

EFFECT OF π -BRIDGES ON ELECTROCHEMICAL AND PHOTOVOLTAIC
PROPERTIES OF BENZOTHIADIAZOLE AND BENZODITHIOPHENE
BASED CONJUGATED POLYMERS

A THESIS SUBMITTED TO
THE GRADUATE SCHOOL OF NATURAL AND APPLIED SCIENCES
OF
MIDDLE EAST TECHNICAL UNIVERSITY

BY

DILAN ECE DİKBİYİK

IN PARTIAL FULFILLMENT OF THE REQUIREMENTS
FOR
THE DEGREE OF MASTER OF SCIENCE
IN
CHEMISTRY

JANUARY 2022

Approval of the thesis:

**EFFECT OF π -BRIDGES ON ELECTROCHEMICAL AND
PHOTOVOLTAIC PROPERTIES OF BENZOTHIADIAZOLE AND
BENZODITHIOPHENE BASED CONJUGATED POLYMERS**

submitted by **DİLAN ECE DİKBIYIK** in partial fulfillment of the requirements for
the degree of **Master of Science in Chemistry, Middle East Technical University**
by,

Prof. Dr. Halil Kalıpçılar
Dean, Graduate School of **Natural and Applied Sciences**

Prof. Dr. Özdemir Doğan
Head of the Department, **Chemistry**

Prof. Dr. Ali Çırpan
Supervisor, **Chemistry, METU**

Dr. Gönül Hızalan Özsoy
Co-Supervisor, **ODTÜ-GÜNAM, METU**

Examining Committee Members:

Prof. Dr. Levent Kamil Toppare
Chemistry, METU

Prof. Dr. Ali Çırpan
Chemistry, METU

Prof. Dr. Atilla Cihaner
Chemical Engineering, Atılım University

Prof. Dr. İrem Erel Göktepe
Chemistry, METU

Assist. Prof. Dr. Erol Yıldırım
Chemistry, METU

Date: 28.01.2022

I hereby declare that all information in this document has been obtained and presented in accordance with academic rules and ethical conduct. I also declare that, as required by these rules and conduct, I have fully cited and referenced all material and results that are not original to this work.

Name Last name: Dilan Ece Dikbıyık

Signature:

ABSTRACT

EFFECT OF π -BRIDGES ON ELECTROCHEMICAL AND PHOTOVOLTAIC PROPERTIES OF BENZOTHIADIAZOLE AND BENZODITHIOPHENE BASED CONJUGATED POLYMERS

Dikbıyık, Dilan Ece
Master of Science, Chemistry
Supervisor: Prof. Dr. Ali Çırpan
Co-Supervisor: Dr. Gönül Hızalan Özsoy

January 2022, 96 pages

In this study, a series of the electron Donor - π bridge- Acceptor type conjugated polymers (PT1, PT2, and PT3) were designed and synthesized via Pd-catalyzed Stille polycondensation reactions. Synthesized polymers were used as donor moieties and blended with acceptor unit PC₇₁BM to form the active layer of the bulk heterojunction organic solar cell (BHJ OSC). Polymers contain electron-deficient benzothiadiazole (BT) as acceptor unit and electron-rich benzodithiophene (BDT) as donor unit. Moreover, thiophene, selenophene, and thieno[3,2-*b*] thiophene were introduced to the polymer backbone as the π -bridge. This study examined the effects of π -bridges on the optical, electrochemical, and photovoltaic properties of the conjugated polymers. The optical band gaps of the PT1, PT2, and PT3 were tuned from 1.70 to 1.58 to 1.61 eV with HOMO levels up-shifted from -5.60 to -5.48 to -5.33 eV, respectively, as the π -bridge was changed from thiophene to selenophene, then to thieno[3,2-*b*]thiophene. OSCs were constructed with the device architecture of ITO/PEDOT:PSS/Polymer: PC₇₁BM/LiF/Al, and power conversion efficiency (PCE) of the devices were measured under standard AM 1.5G illumination (100

mW/cm²). The highest PCE of bulk heterojunction solar cells was found as 3.48 % for PT1 and 2.42 % for PT2.

Keywords: Benzothiadiazole, Benzodithiophene, π -bridge, Donor-Acceptor Type Conjugated polymer, Organic Solar Cell.

ÖZ

π -KÖPRÜLERİNİN BENZOTİYADIAZOL VE BENZODİTİYOFEN BAZLI KONJÜGE POLİMERLERİN ELEKTROKİMYASAL VE FOTOVOLTAİK ÖZELLİKLERİNE ETKİSİ

Dikbıyık, Dilan Ece
Yüksek Lisans, Kimya
Tez Yöneticisi: Prof. Dr. Ali Çırpan
Ortak Tez Yöneticisi: Dr. Gönül Hızalan Özsoy

Ocak 2022, 96 sayfa

Bu çalışmada, bir dizi elektron Verici- π köprüsü- Alıcı tipi konjüge polimerler (PT1,PT2 ve PT3) tasarlanmış ve Pd-katalizli Stille polikondenzasyon tepkimeleri kullanılarak sentezlenmiştir. Sentezlenen polimerler, donör kısım olarak kullanıldı ve toplu hetero bağlantılı organik güneş pilinin aktif tabakasını oluşturmak için alıcı birim olan PC₇₁BM ile harmanlandı. Polimerler verici birim olarak elektronca zengin benzoditiyofen (BDT) ve alıcı birim olarak elektronca eksik benzotiyadiazol (BT) gruplarını içerir. Ayrıca, tiyofen, selenofen ve tieno[3,2-b]tiyofen, kopolimer omurgasında π -köprüsü olarak dahil edildi. Bu çalışmada, farklı π – köprülerinin konjüge polimerlerin optik, elektrokimyasal ve fotovoltaiik özellikleri üzerindeki etkisi incelenmiştir. π -köprüsü tiyofen'den selenofen'e ve tieno[3,2-b]tiyofen'e değıştikçe, PT1, PT2 ve PT3'ün bant aralıkları 1,70'den 1,58'e ve 1,61 eV'a ayarlandı ve HOMO seviyeleri sırasıyla -5,60'dan -5,48'e ve -5,33 eV'a kaydı. OSC'ler ITO/PEDOT:PSS/Polimer:PC₇₁BM/LiF/Al olarak cihaz mimarisi ile oluşturulmuş ve cihazların güç dönüşüm verimliliği (PCE) standart AM 1.5G aydınlatma (100 mW/cm²) altında ölçülmüştür. Toplu heteroeklem güneş pillerinin

en yüksek güç dönüştürme verimliliği, PT1 için %3.48, ve PT2 için %2.42 olarak bulunmuştur.

Anahtar Kelimeler: Benzotiyadiazol, Benzoditiyofen, π – köprüsü, Donör-Alıcı Tip Konjuge Polimer, Organik Güneş Pili.

To my beloved friends & family

ACKNOWLEDGMENTS

Firstly, I would like to express my special gratitude to my supervisor Prof. Dr. Ali Çırpan, for his endless support and guidance throughout my research journey. He is not only a great advisor finding a way to encourage me but also be a family member for me. I am sincerely grateful to him for giving me the chance to work with him.

I owe my thank to Prof. Dr. Levent Toppare for his valuable discussions, suggestions, and comments during our lab meetings.

I would like to that my co-advisor Dr. Gönül Hızalan Özsoy, for everything that I have learned. She was an extraordinary teacher for me during this study. Her discussions and advice will always lead me. I am sincerely grateful to her for giving me the chance to work with her. I also would like to thank her for contributing to organic solar cell studies and her valuable discussions.

I would like to express my gratitude to Sultan Taşkaya Aslan. She always has been kind, patient, and helpful to me since my undergraduate research. She patiently answered all my questions. She is the best boss ever.

I would like to thank Duygu Cevher for optical, electrochemical characterizations, valuable discussions, and comments.

I owe my special thanks to my lab mates Selin Gülmez, Oğuzhan Karakurt, Ümmügülsüm Şahin, and Cem Maraşlıoğlu for sharing great moments and a perfect working environment.

I would also thank the members of Çırpan Research Group, especially Mertcan Erer and Eda Alemdar Yılmaz, for their presence and support.

I would also like to declare my deepest gratitude to my close friends Zafer Çılgın, Tuğçe Deniz, Nazım Çınar Duvaryapar, Bengül Bıyık, Ferhat Kalkan, Umut Aydemir who have shared my happiest and hard moments throughout this journey.

I would like to thank Günbaş Research Group members especially, Sena Tarım, Cevahir Ceren Akgül, Osman Karaman, and Dr. Mustafa Yaşa, for their incredible friendship, support, and happy memories. I hope that everything will be the best for them and our friendship will continue for a long time.

I owe my thanks to my best friend Andaç Öztürk for his friendship, encouragement, and all shared memories. He is always with me despite all distance.

Special thanks go to my amazing friends who always stands by me whenever I need; Deniz Ünlü, İrem Erol, Şule Bayram, and İrem Yazıcı. I am indebted to them for every shared unforgettable moment. Their presence and love gave me the strength that I need to proceed. Words cannot express how much I deeply love them and mean to me. They are the family I choose. I love them to the moon and back.

Last but not least, I would like to thank Filiz Dikbıyık, Atilla Dikbıyık and Ege Dikbıyık for their endless love and understanding. They are always there to encourage me to do better whenever I despair. I owe them everything I have accomplished thus far. My special thanks go to my brother, whom I am fortunate to be in my life and always will be. Their endless support is meaningful than anything in this world.

This study is partially funded by the Scientific and Technological Research Council of Turkey (TUBITAK) under grant number 118Z738. I would also like to thank METU Central Laboratory for TGA, DSC, TEM, and AFM analysis.

Finally, I would like to thank my thesis defense committee members, Prof. Dr. Levent Toppare, Prof. Dr. Atilla Cihaner, Prof. Dr. İrem Erel Göktepe, and Assist. Prof. Dr. Erol Yıldırım for their contributions. Their excellent feedback and evaluations have greatly aided me in improving this thesis.

TABLE OF CONTENTS

ABSTRACT	v
ÖZ.....	vii
ACKNOWLEDGMENTS	x
TABLE OF CONTENTS	xii
LIST OF TABLES	xv
LIST OF FIGURES	xvi
LIST OF ABBREVIATIONS	xix
LIST OF SYMBOLS.....	xxii
CHAPTERS	
1 INTRODUCTION	1
1.1 Energy Demand of the World.....	1
1.2 Renewable Energy.....	2
1.3 Solar Cell Technology	3
1.4 Organic Solar Cells.....	4
1.4.1 Bulk Heterojunction OSCs	5
1.5 Working Principle of OSCs.....	6
1.5.1 Absorption of Light and Formation of Excitons.....	7
1.5.2 Diffusion of Excitons and Dissociation of Charges.....	8
1.5.3 Transportation of Free Charge Carriers	9
1.5.4 Collection of the Charge Carriers	10

1.6	Fabrication of OSCs.....	10
1.7	Parameters- performance characteristics of Solar Cell Device.....	12
1.7.1	Power Conversion Efficiency of OSCs	13
1.7.2	Open Circuit Voltage (V_{oc})	13
1.7.3	Short Circuit Current Density (J_{sc}).....	14
1.7.4	Fill Factor (FF)	15
1.8	Conjugated Polymers for OSCs	16
1.9	Molecular Engineering of Conjugated Polymers.....	17
1.10	Donor – Acceptor Approach.....	19
1.11	Effect of π -bridges	20
1.12	Benzothiadiazole as Acceptor Unit.....	21
1.13	Benzodithiophene as Donor Unit.....	22
1.14	Review of Literature	23
1.15	Aim of the Study	26
2	EXPERIMENTAL.....	29
2.1	Materials and Methods.....	29
2.2	Synthesis	30
2.2.1	Synthesis of Monomers	30
2.2.2	Synthesis of Polymers	41
2.3	Characterizations of Polymers	47
2.3.1	Gel Permeation Chromatography.....	47
2.3.2	Thermal Analysis	47
2.3.3	Cyclic Voltammetry	48
2.3.4	Spectroelectrochemical Studies.....	49

2.3.5	Photovoltaic Studies	50
3	RESULTS AND DISCUSSION.....	51
3.1	Electrochemical Studies	51
3.2	Optical Studies.....	54
3.3	Photovoltaic Studies	56
3.4	Thermal Studies.....	61
3.5	Morphology	62
4	CONCLUSION	65
5	REFERENCES	67
APPENDICES		
A.	NMR DATA.....	83
B.	THERMAL ANALYSIS DATA.....	95

LIST OF TABLES

TABLES

Table 1 Photovoltaic properties of the π bridged polymers in the literature	24
Table 2 Optical & electrochemical properties of π bridged polymers in literature	24
Table 3 Summary of electrochemical properties of PT1, PT2, and PT3.	53
Table 4 Summary of the optical properties of PT1, PT2, and PT3.....	55
Table 5 Summary of the photovoltaic properties of PT1	58
Table 6 Summary of the photovoltaic properties of PT2.....	59

LIST OF FIGURES

FIGURES

Figure 1. Global primary energy consumption by source	1
Figure 2. NREL's efficiency chart.....	4
Figure 3. a) Device architecture of bulk heterojunction OSC. b) Working mechanism of BHJ OSC.....	5
Figure 4. Working principle of bulk heterojunction OSC.....	6
Figure 5. a) Frenkel excitons in organic semiconductors, b) Mott-Wannier excitons in inorganic semiconductors.....	7
Figure 6 BHJ OSC illustration	11
Figure 7 Chemical structure of the PEDOT: PSS	11
Figure 8 Typical J-V curve for OSC	12
Figure 9 Commonly used conjugated polymers.....	16
Figure 10 Illustration of a typical conjugated polymer for PSC	17
Figure 11 Chemical structure of the benzo[c][2,1,3]thiadiazole.....	21
Figure 12 Chemical structure of the benzo[1,2-b:4,5-b']dithiophene.....	22
Figure 13 Molecular structures of the π -bridged polymers in the literature.....	25
Figure 14 Synthesized polymer structures	27
Figure 15 Synthetic pathway of the monomers: TBTBr, SeBTBr, and TTBTBr ...	30
Figure 16 Synthesis of compound (1)	31
Figure 17 Synthesis of compound (2)	32
Figure 18 Synthesis of compound (3)	33
Figure 19 Synthesis of compound (4)	34
Figure 20 Synthesis of TBT	35
Figure 21 Synthesis of SeBT	36
Figure 22 Synthesis of TTBT	37
Figure 23 Synthesis of TBTBr	38
Figure 24 Synthesis of SeBTBr.....	39
Figure 25 Synthesis of TTBTBr.....	40

Figure 26	Synthesis of PT1	41
Figure 27	Synthesis of PT2.....	43
Figure 28	Synthesis of PT3.....	45
Figure 29	(a) Voltammogram for CPs (b) Experimental setup for CV study.....	48
Figure 30	Experimental setup for optical study.....	49
Figure 31	Device construction of BHJ OSCs.	50
Figure 32	Cyclic voltammograms of a) PT1, b) PT2 and c) PT3 in 0.1 M TBAPF ₆ /ACN at 100 mV/s scan rate.....	52
Figure 33	UV-Vis normalized absorption spectra of in CHCl ₃ solution and thin-film for (a) PT1, (b) PT2, and (c) PT3.....	54
Figure 34	Energy level diagram of the PT1, PT2, and PT3.....	56
Figure 35	J-V characterization of a) PT1, and b) PT2.....	60
Figure 36	EQE curves of PT1 and PT2 based best-performed devices.....	61
Figure 37	AFM images of A) PT1: PC ₇₁ BM (1:2, w/w), B) PT1: PC ₇₁ BM (1:2, w/w) with 3% DPE additive, C) PT2: PC ₇₁ BM (1:2, w/w), D) PT2: PC ₇₁ BM (1:2, w/w) with 3% DPE additive. Scale bar is 200 nm.	62
Figure 38	3D-AFM images of A) PT1: PC ₇₁ BM (1:2, w/w), B) PT1: PC ₇₁ BM (1:2, w/w)) with 3% DPE additive, C) PT2: PC ₇₁ BM (1:2, w/w), D) PT2: PC ₇₁ BM (1:2, w/w) with 3% DPE additive	63
Figure 39	TEM images of best performed devices A) PT1: PC ₇₁ BM (1:2, w/w), B) PT1: PC ₇₁ BM (1:2, w/w) with DPE additive, C) PT2: PC ₇₁ BM (1:2, w/w), D) PT2: PC ₇₁ BM (1:2, w/w) with DPE additive.....	64
Figure A. 1	¹ H NMR spectrum of compound 1 in CDCl ₃	83
Figure A. 2	¹³ C NMR spectrum of compound 1 in CDCl ₃	84
Figure A. 3	¹ H NMR spectrum of compound 2 in CDCl ₃	84
Figure A. 4	¹³ C NMR spectrum of compound 2 in CDCl ₃	85
Figure A. 5	¹ H NMR spectrum of compound 3 in CDCl ₃).....	85
Figure A. 6	¹³ C NMR spectrum of compound 3 in CDCl ₃	86

Figure A.7 ^1H NMR of compound 4 in CDCl_3	86
Figure A. 8 ^{13}C NMR of compound 4 in CDCl_3	87
Figure A. 9 ^1H NMR spectrum of TBT in CDCl_3	87
Figure A. 10 ^{13}C NMR spectrum of TBT in CDCl_3	88
Figure A. 11 ^1H NMR spectrum of TBTBr in CDCl_3	88
Figure A. 12 ^{13}C NMR spectrum of TBTBr in CDCl_3	89
Figure A. 13 ^1H NMR spectrum of SeBT in CDCl_3	89
Figure A. 14 ^{13}C NMR spectrum of SeBT in CDCl_3	90
Figure A. 15 ^1H NMR spectrum of SeBTBr in CDCl_3	90
Figure A. 16 ^{13}C NMR spectrum of SeBTBr in CDCl_3	91
Figure A. 17 ^1H NMR spectrum of TTBT in CDCl_3	91
Figure A. 18 ^{13}C NMR spectrum of TTBT in CDCl_3	92
Figure A. 19 ^1H NMR spectrum of TTBTBr in CDCl_3	92
Figure A. 20 ^{13}C NMR spectrum of TTBTBr in CDCl_3	93
Figure A. 21 ^1H NMR spectrum of PT1 in CDCl_3	93
Figure A. 22 ^1H NMR spectrum of PT2 in CDCl_3	94
Figure A. 23 ^1H NMR spectrum of PT3 in CDCl_3	94
Figure B. 1 TGA study of PT1	95
Figure B. 2 TGA study of PT2	95
Figure B. 3 TGA study of PT3	96

LIST OF ABBREVIATIONS

ABBREVIATIONS

SET	Solar Energy Technology
PV	Photovoltaic
OSC	Organic Solar Cell
PCE	Power Conversion Efficiency
ITO	Indium Tin Oxide
Al	Aluminum
BHJ	Bulk Heterojunction
PPV	Poly(p-phenylene vinylene)
CP	Conjugated Polymer
D	Donor
A	Acceptor
OPV	Organic Photovoltaic
HOMO	Highest Occupied Molecular Orbital
LUMO	Lowest Unoccupied Molecular Orbital
WF	Work Function
PEDOT: PSS	Poly(3,4-ethylenedioxythiophene) Polystyrene Sulfonate
PET	Polyethylene Terephthalate
PES	Poly (ether sulfonate)
PC ₇₁ BM	Phenyl-C ₇₁ -butyric acid methyl ester

HTL	Hole Transport Layer
LiF	Lithium Fluoride
J-V	Current density - Voltage
FF	Fill Factor
P_{in}	Power Density of Incident Light
OLED	Organic Light Emitting Diode
OFET	Organic Field-Effect Transistors
PSC	Polymer Solar Cell
BDT	Benzodithiophene
LBG	Low Band Gap
BT	Benzothiadiazole
EA	Electron Affinity
BO	Benzoxadiazole
T	Thiophene
Se	Selenophene
F	Furan
TT	Thieno[3,2- <i>b</i>]thiophene
GPC	Gel Permeation Chromatography
TMS	Tetramethylsilane
CV	Cyclic voltammetry
CE	Counter Electrode
WE	Working Electrode

RE	Reference Electrode
TBAPF ₆ /ACN	Tetrabutylammonium hexafluorophosphate /acetonitrile
P3HT	Poly(3-hexylthiophene-2,5-diyl)
ICT	Intramolecular charge transfer
PDI	Polydispersity index
TGA	Thermogravimetric analysis
DSC	Differential scanning calorimetry
Cb	Chlorobenzene
O-dcb	Orto-dichlorobenzene

LIST OF SYMBOLS

SYMBOLS

δ	Chemical shift
J	Coupling constant
λ_{max}	Maximum wavelength
E_{ox}^{onset}	Oxidation onset potential
E_{red}^{onset}	Reduction onset potential
T_d	Decomposition temperature
M_w	Weight average molecular weight
M_n	Number average molecular weight
E_g	Band Gap
M_{pp}	Maximum Power Point
J_{sc}	Short Circuit Density
J_{mpp}	Current at Maximum Point
V_{mpp}	Voltage at Maximum Point
V_{oc}	Open Circuit Voltage

CHAPTER 1

INTRODUCTION

1.1 Energy Demand of the World

With the rapid development of modern society and the advancement of technology, the energy shortage and environmental pollution caused by the energy demand of the world are becoming problematic. To fulfill the growing energy demand of the developing world, various energy sources have started to be used. From the late 1800s to the present, fossil fuel (coal, oil, gas) has been the dominant source of energy production, as reported in the Statistical Review of World Energy in 2020 [1] shown in Figure 1.

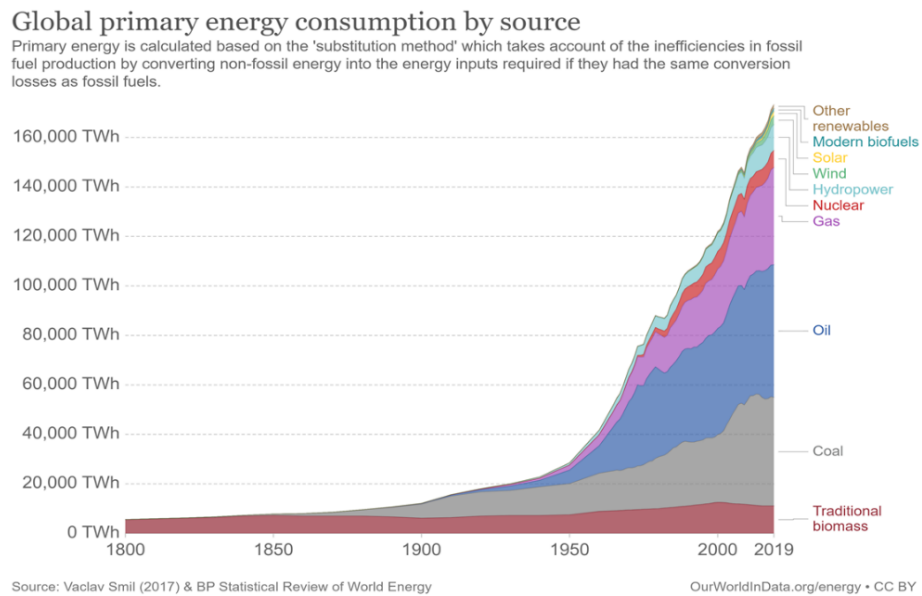


Figure 1. Global primary energy consumption by source [1,2]

The combustion of fossil fuels to generate energy increases greenhouse gas emissions, damages people's health, and accumulates harmful pollutants in the environment. The burning of fossil fuels contributes significantly to the increase in carbon dioxide concentration, thereby exacerbating the threat of global warming.

Aside from environmental and health concerns, the gradual depletion of the world's finite fossil fuel reserves adversely affects energy production and energy conversion. This is driving up demand for clean, sustainable, and renewable energy sources, e.g., wave, wind, hydroelectric, geothermal, biomass, solar energy [3].

1.2 Renewable Energy

To deal with the negative impacts of fossil fuels on the environment and human health and to overcome the increasing energy demand problem of many countries, renewable and environmentally friendly energy source alternatives have been started to researched [4]. Renewable energy is derived from constantly replenished natural processes such as the sun, rain, wind, ocean tides, biomass, and geothermal resources from heat generated deep under the ground in various ways [5]. Solar energy is one of the cleanest, functional, cheap, and environmentally friendly renewable energy sources that do not contribute to global warming. Solar energy is superior to any other type of energy in terms of environmental benefits. Solar energy technology (SET) does not deplete natural resources, emit CO₂ or other gases into the atmosphere, or generate liquid or solid waste that harms the environment [6]. The use of SETs provides additional environmental benefits, including [6–10]:

- Reduction of the emissions of greenhouse gases (CO₂, NO_x) and prevention of toxic gas emissions (SO₂, particulates).
- Reclamation of degraded land.
- Reduction of the required transmission lines of the electricity grids.
- Improvement of the quality of water resources.

1.3 Solar Cell Technology

The use of solar cell technology to generate electricity has become popular since it provides pollution-free, self-contained, stable, silent, long-term, maintenance-free, and year-round continuous and unlimited operation at moderate costs [11]. Various technologies have been employed to solve energy issues and reduce reliance on fossil fuels. One of these technologies is photovoltaic (PV) modules to harness solar energy. A solar cell is an electrical device that uses the photovoltaic effect, a chemical and a physical phenomenon, for converting sunlight into electricity [12]. Photovoltaics can be manufactured in various ways and with a wide range of materials, regardless of their differences; all have the same goal, to collect solar energy and convert it into electricity [13]. Silicon has become the dominant technology for producing electricity from sunlight, accounting for more than 90% of the PV market due to its high efficiencies (as shown in Figure 2) [14]. Although silicon is one of the most abundant elements in nature, it is found as silica or silicon dioxide (SiO_2), not its elemental form. Therefore, several purifications and refining processes are necessary to produce silicon from silica. Aside from its abundance, silicon is non-toxic, non-corrosive material.

Moreover, at the contact between the silicon and the atmosphere, it forms a very thin, stable, and tightly adherent protective layer of SiO_2 [15,16]. This electrically insulating oxide, which forms naturally, functions as a passivating layer, reducing the recombination centers at the surface and boosting the silicon solar cell performance [17]. The oxide layer also minimizes the danger of a silicon wafer inside a solar module degrading. As a result, the technology's long-term stability has helped silicon-based solar cells to gain importance in the PV market. In April 2020, Geisz and France et al. reported a six-junction III-V solar cell with a PCE of 47.1% in an issue of Nature Energy [18] which holds the world record for highest efficiency.

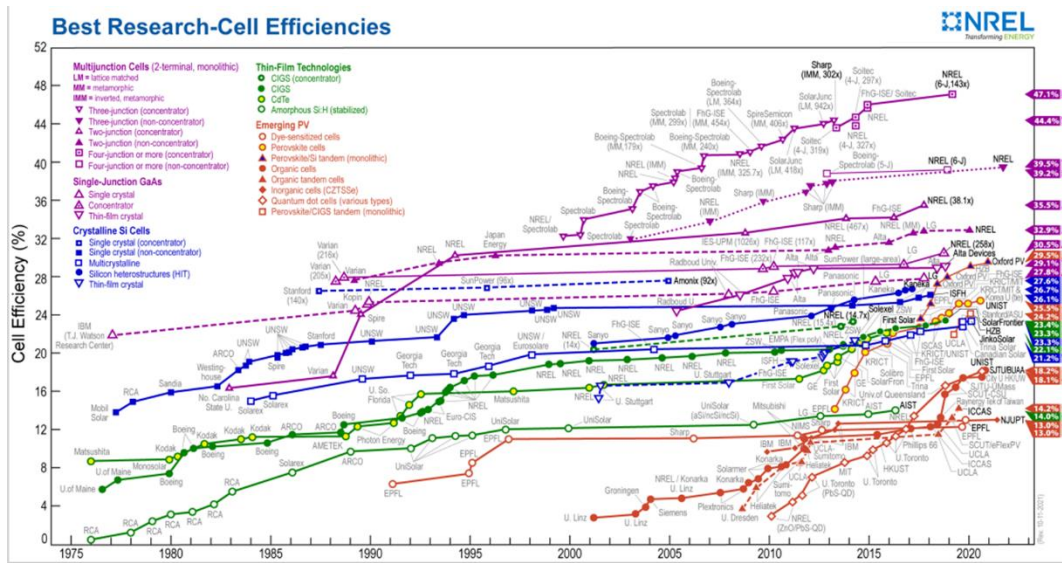


Figure 2. NREL's efficiency chart, 2021 [19].

On the other hand, silicon has a substantially low bandgap and low absorption coefficient; a thicker piece of the material is required to absorb solar radiation over the band gap energy. This necessitates a silicon wafer thicker than 100 μm , providing the inapplicability of silicon solar cells for thin-film technology [16]. Therefore, silicon-based photovoltaics have a higher cost structure than alternative renewable energy technologies. Organic solar cells (OSC) become a possible option for the photovoltaic industry due to their ability for chemical modification, low manufacturing costs, and potential for large-scale production [20].

1.4 Organic Solar Cells

Although silicon-based inorganic photovoltaics dominate the energy industry, their application procedures are costly. On the other hand, organic semiconductors, such as OSCs, have entered the picture with the advantages of low cost, lightweight, flexibility, semitransparency, and ease of manufacture as an alternative to inorganic solar cells [21–26]. Organic photovoltaics are electronic devices that generate electricity from sunlight and carbon-based organic semiconducting materials [27].

Conducting polymers are utilized as active materials since they can absorb sunlight, generate and transfer charge carriers with the delocalized π electron system in the polymer chain [28].

1.4.1 Bulk Heterojunction OSCs

In recent decades, bulk heterojunction (BHJ) organic solar cells (OSCs) have become a preferred alternative for the generation of renewable and clean energy due to their appealing qualities of lightweight, flexibility, large-scale production [11,29,30].

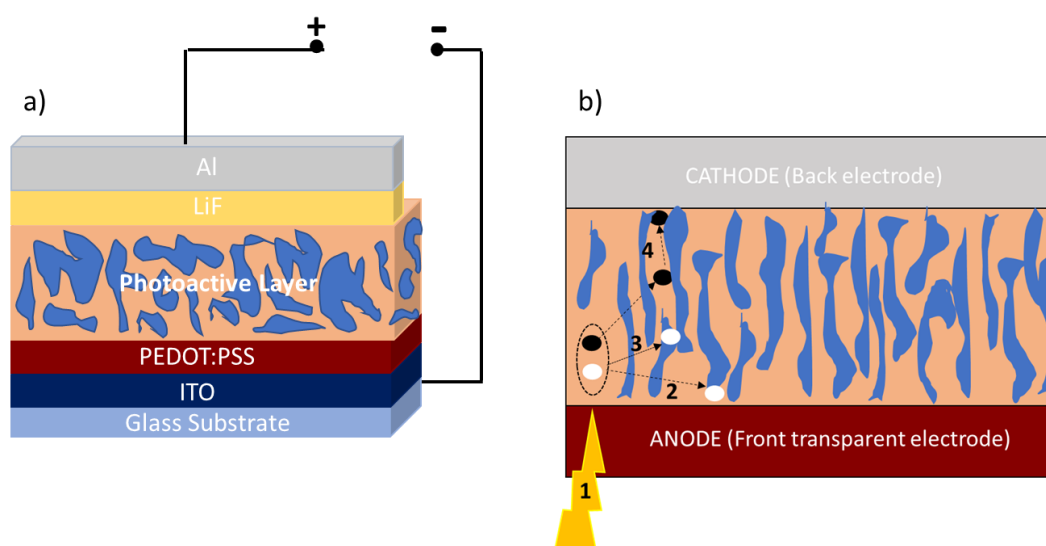


Figure 3. a) Device architecture of bulk heterojunction OSC. b) Working mechanism of BHJ OSC.

As shown in Figure 3, the BHJ OSC is a thin film device made up of donor-acceptor material sandwiched between anode and cathode. Conjugated polymers (CPs), oligomers, and conjugated pigments are commonly utilized as a donor, with fullerene derivatives are used as an acceptor material. In general, CPs materials are classified as organic semiconductors, and they have the ability to transport charges and outstanding optical characteristics [31].

With the invention of the BHJ device architecture, the exciton diffusion problem has been solved, and efficient charge transfer has been achieved. The use of the blended form of donor and acceptor materials increases the interfacial area between the donor and acceptor units. It improves the charge separation efficiency, thus improving the efficiency of the OSCs [32].

1.5 Working Principle of OSCs

The four basic processes in the operation of organic solar cells can be summarized as follows [11] (as shown in Figure 3b and Figure 4):

- Absorption of light and formation of an exciton (Coulombically bounded e^-/h^+ pairs).
- Diffusion of the exciton to the D-A interface.
- Separation of the charges at the D-A interface.
- Collection of the charges in the corresponding electrodes.

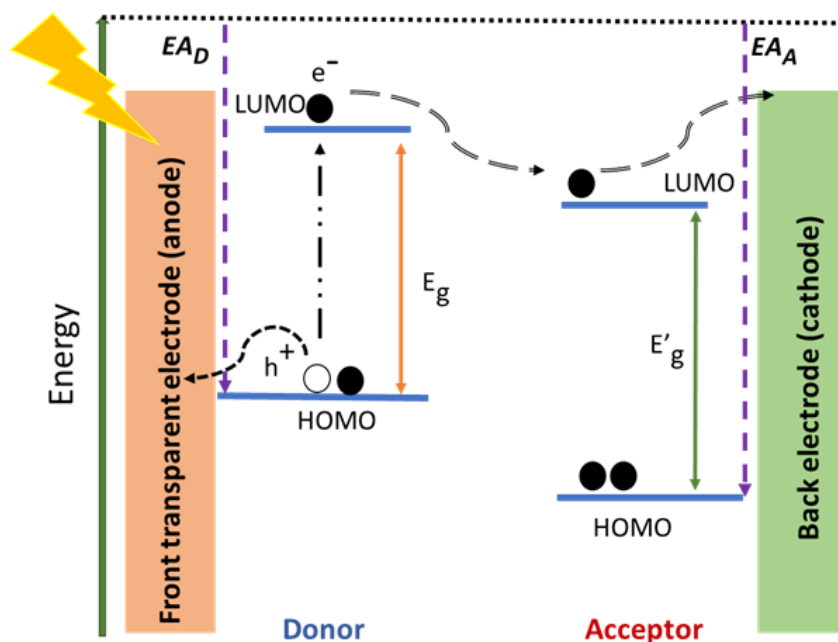


Figure 4. Working principle of bulk heterojunction OSC.

1.5.1 Absorption of Light and Formation of Excitons

In BHJ OSCs, the incoming sunlight is absorbed by the photoactive layer, a conjugated polymer, e.g., donor material of the BHJ photoactive layer [33]. The exciton is the fundamental photogenerated state that originates from the light absorption by organic semiconductor materials. It consists of an electron (e^-) in the lowest unoccupied molecular orbital (LUMO), and a hole (h^+) in the highest occupied molecular orbital (HOMO). Organic semiconductors differ from inorganic semiconductors in that charge carriers are more localized and Coulombic interaction between the opposite charges is stronger. The molecular orbitals in organic solids are more concentrated because the van der Waals connection between molecules is considerably weaker than the bonds within the molecules. As a result, as illustrated in Figure 5, excitons in organic semiconductors (Frenkel excitons) are more localized than inorganic semiconductors (Mott-Wannier excitons).

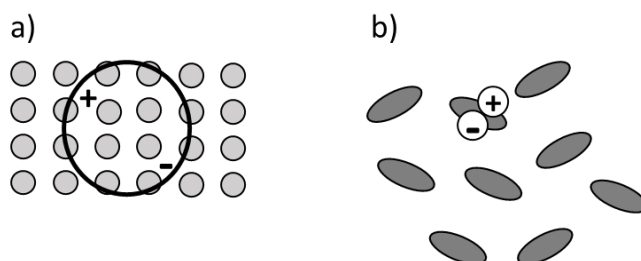


Figure 5. a) Frenkel excitons in organic semiconductors, b) Mott-Wannier excitons in inorganic semiconductors.

The Coulombic attraction between the charges, called the binding energy (E_B), is explained by the following equation:

$$E_B = \frac{e^2}{4\pi\epsilon\epsilon_0 r} \quad \text{where } e: \text{ charge, } \epsilon: \text{ dielectric permittivity, } \epsilon_0: \text{ vacuum permittivity,}$$

and r : separation between the electron and hole.

Inorganic semiconductors have a higher dielectric constant, ϵ , than organic semiconductors, resulting in smaller binding energy (~ 0.025 eV) and more separated electrons and holes at room temperature.

Consequently, due to the smaller dielectric constant and separation, organic semiconductors have greater exciton binding energies ($\sim 0.3\text{-}0.5$ eV). Besides thermal energy, an additional driving force is necessary for generating free charges for organic solar cells (OSCs). Therefore, an interface between the electron donor and acceptor material, known as heterojunction, is necessary to create a free energy difference that contributes to the charge separation [34]. Organic semiconductors can efficiently harvest sunlight with their thin photoactive layer (~ 100 nm) due to high absorption coefficients [35]. Due to low charge carrier mobilities and low diffusion lengths, the polymer-based photoactive layer thickness is also limited. As a result of the narrower absorption of conjugated polymers, decreased photocurrent production is observed. However, narrowing the bandgap of the donor materials improves light absorption, resulting in the maximum number of photon absorption and increasing PCEs [36,37]. Thus, polymers with a narrow bandgap are required to maximize photon harvesting. A bandgap of 1.1 eV, for example, can cover 77% of the AM 1.5 solar photon flux, whereas a bandgap of 1.9 eV can only cover 30% of the AM 1.5 photon flux [37]. As a result, a low bandgap polymer can significantly increase photocurrent generation. An electron is excited from HOMO to LUMO as the light is illuminated from the transparent electrode. An e^-/h^+ pair (exciton) is formed with the E_{binding} of 0.1-1.4 eV. Then, excitons diffuse into the donor-acceptor interface [38].

1.5.2 Diffusion of Excitons and Dissociation of Charges

Photogeneration occurs in OSCs at the heterojunction, where the extra driving force is generated to overcome the Coulombic binding of the e^- and h^+ . In LUMO, the energy difference between the donor and acceptor materials disrupts the Coulomb attraction, causing dissociation of the excitons. Charge separation is promoted in two ways: 1) providing the process is energetically downhill, 2) permitting the electron and hole to be localized on distinct molecules, enhancing the spatial separation and minimizing the chance of recombination. [34].

The diffusion length of the excitons (L_D) is a significant factor for OSCs since the charge separation happens only in the heterojunction. Moreover, L_D limits the volume fraction of the donor and acceptor domains that easily generate charges. If the excitons are formed at a distance greater than L_D , they will be separated or decay before reaching the D-A interface [39]. To obtain free charge carriers, electron-hole pairs with Coulomb bound have to be separated. They recombine or dissociate to form free charge carriers [40]. To obtain efficient charge separation, excitons must dissociate effectively at the interface. The energy difference in the HOMO and LUMO of the donor and acceptor layers creates electrostatic forces at the interface that leads to the generation of an electric field for the effective break-up of excitons into electrons and holes. Free electrons are thus accepted by materials with a greater LUMO level, while holes by materials with a lower HOMO level [33].

1.5.3 Transportation of Free Charge Carriers

As shown in Figure 4, the charges must be transported to the corresponding electrodes after the dissociation of excitons into free charge carriers. In organic semiconductors, charge carriers are typically transported via hopping from one localized state to another [41]. Free charge carriers formed by the Fermi level difference between the electrodes are transported to their respective electrodes by an internal electric field [42]. A high work function (WF) anode and a low WF cathode, in general, produce an internal electric field that identifies the open-circuit voltage (V_{oc}) of the cell [43]. The transfer of free charge carriers is oriented by both carrier diffusion and electric field-induced drift. The fundamental problem to adequate transportation of free charge carriers to the anode and cathode is the recombination of free charge carriers before reaching their respective electrodes. The mobility of the charge carriers in the photoactive layer affects both the transportation of charge carriers and losses, which are related to the recombination of charge carriers [44]. The electrons and holes are bound by Coulomb potential in low mobility materials.

Therefore they cannot overcome their mutual attraction and recombine before reaching the corresponding electrodes[45]. As a result, for high-efficiency devices, the rivalry between the carrier sweep-out by the internal field and the loss of photogenerated carriers by recombination are the critical difficulty to overcome [46].

1.5.4 Collection of the Charge Carriers

When an exciton reaches the donor-acceptor interface, it splits into the electron-hole pairs; they are then transported to the corresponding electrodes to generate photocurrent. The transportation of the charges is achieved if the driving force is strong enough to push the free electrons and holes of the electrodes. At the donor-acceptor junction, the difference between the HOMO of the donor and the LUMO of the acceptor produces a gradient. To maximize the charge extraction, the potential barrier at the photoactive layer and electrode interface must be decreased. As a result, the WF of the anode must match with the HOMO of the donor material, whereas the WF of the cathode must match the LUMO of the acceptor material. The contacts are called Ohmic contacts if the work functions match as indicated [45]. The maximum value of the open-circuit voltage (V_{OC}) and the transportation of the charge carriers are affected by the internal electric field [47,48].

1.6 Fabrication of OSCs

BHJ OSCs are frequently constructed on five main layers; substrate, anode, (Poly (3,4-ethylene dioxythiophene) poly(styrene sulfonate)) (PEDOT: PSS), the active layer, the cathode. Starting with a transparent substrate, glass is widely used in OSCs because of its low cost, stability, and transparency. Additionally, for flexibility, poly (ethylene terephthalate) (PET), poly (ether sulfonate) (PES), and polycarbonate can be used [49].

Glass is coated with a transparent and conductive electrode material. ITO is used in the majority of the reported devices due to its conductivity and outstanding transparency, used as an anode layer. The WF of the ITO can be altered via surface treatment. The use of oxidizing chemicals (e.g., oxygen plasma) on the surface increases WF [50]. The ITO is coated with a hole transport layer (HTL). (Poly(3,4-ethylene dioxythiophene)poly(styrene sulfonate)) (PEDOT: PSS) see Figure 6, thin films of doped conjugated polymer or a thin oxide layer (MoO_3) are commonly used as HTL [39]. PEDOT: PSS provides planarized ITO surface [51].

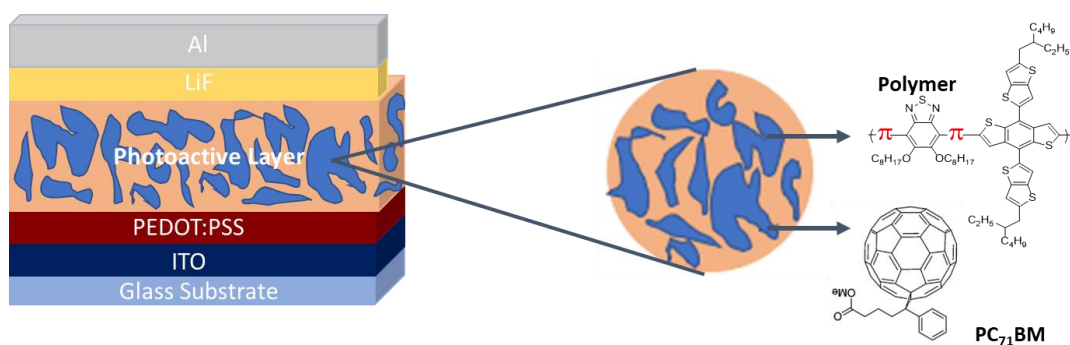


Figure 6 BHI OSC illustration

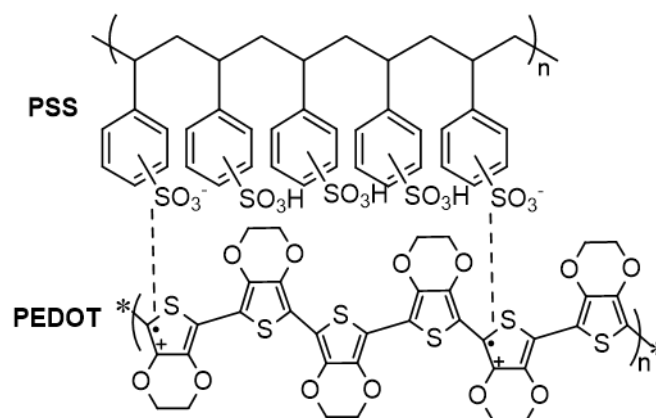


Figure 7 Chemical structure of the PEDOT: PSS

As an active layer, a blend of the donor (e.g., conjugated polymer) and acceptor ([6,6]-Phenyl- C_{61} -butyric acid methyl ester, PCBM) is placed on the top of the HTL.

In general, the cathode is the top electrode in the typical layout, and calcium (Ca), barium (Ba), or aluminum (Al) are used to capture the electrons created in the photoactive layer. A top metal is coated by using the vacuum deposition technique. The cathode materials are selected as low WF metals to match the acceptor's LUMO and collect the electrons effectively [32]. On the other hand, selecting low WF metals leads to stability issues since stability is related to the WF. Thus, a thin layer consists of lithium fluoride (LiF) deposited between the metal and active layer, improving OSC performance [52].

1.7 Parameters- performance characteristics of Solar Cell Device

Figure 8 represents the solar cell's current density-voltage (J-V) curve in the dark and under the light. When the contacts start to inject at forwarding bias for voltages larger than the V_{OC} , there is essentially no current flow in the dark. The device generates power under the light in the fourth quadrant. The current and voltage are the greatest at the maximum power point (P_{max}).

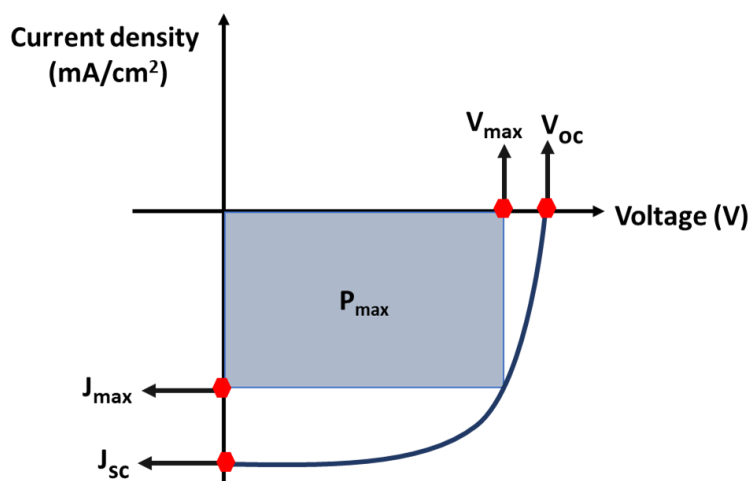


Figure 8 Typical J-V curve for OSC

P_{in} is the power density of incident light. The intensity of the light is standardized at 1000 W.m^{-2} , and the distribution of spectral intensity matches that of the sun on the earth's surface at a 48.2° incidence angle [32].

J_{\max} represents the current, while V_{\max} is the voltage at the maximum point. The V_{OC} of metal-insulator-metal type devices is generally determined by the difference between the WF's of two metal contacts. However, for p-n junction, V_{OC} is selected via the contrast of the quasi-Fermi levels of two charge carriers, the energy level of n-doped semiconductor and p-doped semiconductor. In OSCs, V_{OC} is linearly related with the HOMO level of the donor (p-type semiconductor) and LUMO level of the acceptor (n-type semiconductor). When there is no current flowing across a circuit, the voltage is called open-circuit voltage (V_{OC}). On the other hand, when the voltage is zero, the amount of the current flows across the circuit is called the short current density (J_{SC}). The fill factor (FF) is the maximum power of OSCs ratio to the multiplication of V_{OC} and J_{SC} .

1.7.1 Power Conversion Efficiency of OSCs

The ratio of the maximum power generated by the solar cell to the total power applied to the device by solar spectrum is known as power conversion efficiency (PCE). This parameter can also be explained as the maximum efficiency of the solar cell. Other parameters affect the performance of the solar cell. The PCE of a solar cell is determined after the current-voltage (J-V) characterization of a solar cell under AM 1.5G illumination.

$$PCE\% = \frac{P_{OUT}}{P_{IN}} \times 100 = \frac{FF \times J_{SC} \times V_{OC}}{100 \text{ mW/cm}^2} \times 100 = FF \times J_{SC} \times V_{OC}$$

1.7.2 Open Circuit Voltage (V_{OC})

As shown in Figure 8, basically V_{OC} is determined as the recorded voltage when no current flows through the system. The following equation gives the information about the determination of V_{OC} values, approximately [53].

$$V_{OC} \cong \frac{1}{e} (E_{LUMO}^{Acceptor} - E_{HOMO}^{Donor} - \Delta) - \frac{kT}{e} \ln\left(\frac{n_e n_h}{N_c^2}\right)$$

From the equation, the difference between the HOMO of donor and the LUMO of acceptor determines the V_{OC} [54]. Further detail can be determined by the difference between the quasi-Fermi levels of holes and electrons under illumination, assuming barrierless connections to the electrodes are formed. Moreover, the recombination rate in the device limits the V_{OC} [55]. In most cases, the difference in the work functions (WF) of electrodes determines the V_{oc} . On the other hand, in the recently evolved OSC architectures, V_{OC} values are enhanced towards the interfacial layers employed in device architecture, primarily by the active layer. High HOMO energy levels should not be used to achieve a narrow band gap for conjugated polymers in OSCs to prevent V_{OC} losses.

Additionally, using non-fullerene acceptors can be another way to enhance V_{OC} values due to their exchangeable LUMO levels [56,57]. Aside from the energy levels, V_{OC} values are also relative to the efficiency with which charges are collected at corresponding electrodes. As a result, factors affecting the overall performance of OSC, such as optimum morphology, contact quality, charge transfer through the device via suitable energy levels, and high shunt resistance, are related to enhancing V_{OC} values [58,59].

1.7.3 Short Circuit Current Density (J_{SC})

As shown in Figure 8, short circuit current density (J_{SC}) is measured as the current density when no external voltage is applied through the system. J_{SC} is called current density instead of short circuit current since it is the current value measured for the area of the OSC. The absorption of the active layer mainly determines the J_{SC} value.

Therefore, both the donor-acceptor (D-A) blend concentration and the donor molecule loading enhance the absorption; these factors improve the J_{SC} value. On the other hand, J_{SC} is also strongly dependent on both efficient charge collection on the electrons and the quantity of generated excitons. Higher shunt resistance values and lower series are required.

Additionally, to obtain high J_{SC} values, the properties for an ideal conjugated polymer (CP) with a low band gap and defect-free OSC architecture are necessary [60]. Since as the band gap of the CP becomes narrower, more light could be absorbed, which enhances the J_{SC} . Additionally, a few more appealing characteristics such as high molecular weight, high charge mobility, and optimal active layer morphology can be included to reduce these losses, all of which enhance the J_{SC} value [61].

1.7.4 Fill Factor (FF)

Fill factor (FF) is a characteristic that determines how much of a solar cell's maximal performance it can display. The following relationship explains the FF parameter:

$$FF = \frac{J_{max} \times V_{max}}{J_{sc} \times V_{oc}}$$

FF equals 1 only if the ideal case is represented as the white region in Figure 8. However, the blue box labeled as P_{max} on the J-V curve holds in the real case. Both J_{max} and V_{max} define the maximum power output by the OSC. All characteristics that affect the J_{SC} value, excluding the absorption of the active layer, also affect the FF value. On the other hand, all factors that affect the V_{OC} value, excluding the energy difference between the HOMO of acceptor and the LUMO of the donor, and the WF of electrodes, also affect the FF value [58,62]. To obtain higher FF values, collection of charges through the corresponding electrodes, smaller series resistance (R_s), and larger shunt resistance (R_{sc}) are required factors influenced by the morphology of the D-A blend. Therefore, the morphology of the active layer should be optimized to enhance charge separation and transport of photogenerated charges for increasing the FF and J_{SC} values [61]. The transportation of charges benefits from a homogeneous active layer, smaller domains, higher domain purity, and crystallization. Additionally, the morphology of the active layer can be affected by solvent choice, additives, adjusting the donor-acceptor blend ratio, and thermal annealing [63].

1.8 Conjugated Polymers for OSCs

Conjugated polymers are organic macromolecules with alternating double and single bonds in their backbone. Conjugated polymers containing overlapping p-orbitals create a delocalized π -electrons system with optical and electronic properties. Delocalization of electrons is achieved across the polymer backbone with the sp^2 hybridized carbon-based polymer structure. As a result, polymers have the ability of high electron polarizability and semiconducting characteristics. Therefore, conjugated polymers are also known as conductive polymers [58]. As an example, commonly used conjugated polymers are shown in Figure 9.

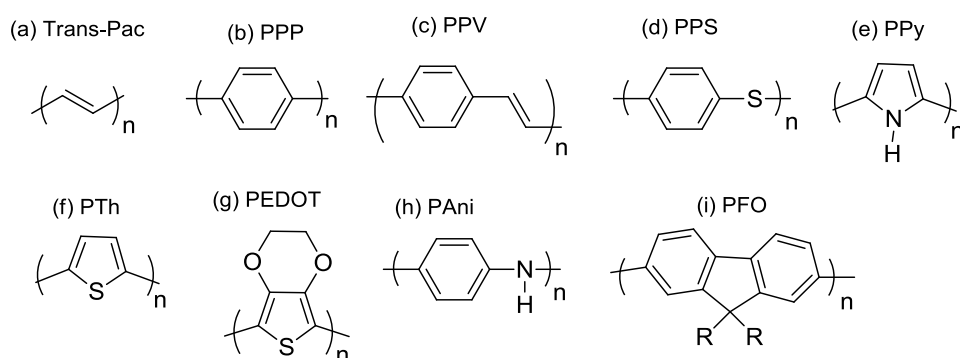


Figure 9 Commonly used conjugated polymers

(a)Trans-polyacetylene-trans-Pac,(b)Poly(p-phenylene)-PPP, (c)Poly(phenylenevinylene)-PPV,(d) Poly(p-phenylene-sulphide)-PPS,(e) Polypyrrole-PPy,(f) Polythiophene-PTh,(g) Poly(3,4-ethylenedioxythiophene)PEDOT,(h) Polyaniline-PAni and (i) Polyfluorene-PFO.

Conjugated polymers gained prominence after the discovery of highly conductive polyacetylene. MacDiarmid, Heeger, and Shirakawa were awarded Nobel Prize in Chemistry in 2000 [64]. Although conjugated polymers have lower charge carrier mobility and conductivity than inorganic semiconductors and metals, they offer functional and structural diversity, solution processability, lightweight, flexibility, suitable bandgap, and low cost.

Organic photovoltaics (OPVs), organic light-emitting diodes (OLED), organic field-effect transistors (OFET), supercapacitors, batteries, and different types of sensors have all benefited from this family of materials since semiconducting characteristics and advantages of the conjugated polymers over mainstream silicon-based solar cells [65].

1.9 Molecular Engineering of Conjugated Polymers

Conjugated polymers can be categorized into three main constituting parts: (1) conjugated backbone, (2) side chains, (3) substituents, as shown in Figure 10.

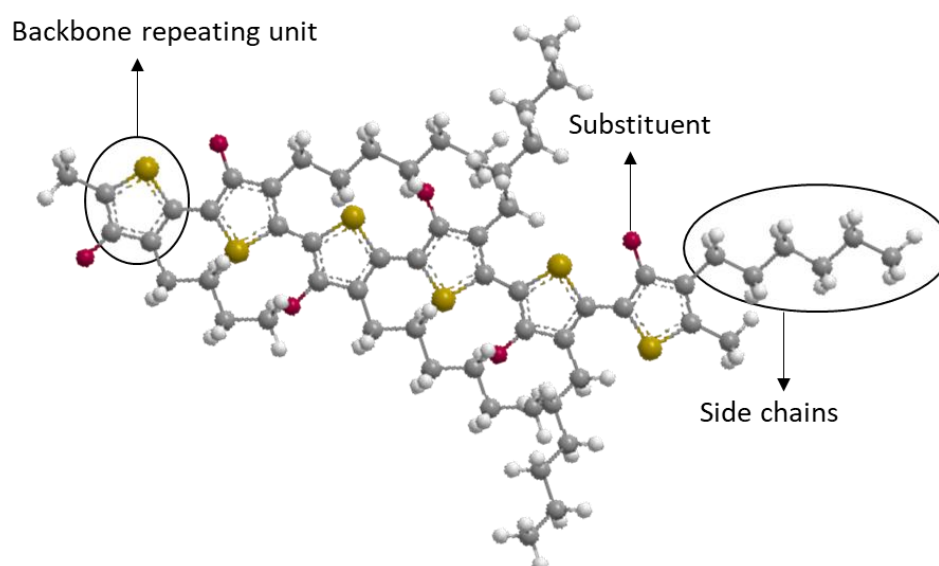


Figure 10 Illustration of a typical conjugated polymer for PSC

The most significant constituent is the conjugated backbone. It determines most of the PSC-related physical characteristics of the CPs, such as band-gap, energy levels, intermolecular, and intramolecular interactions. Several distinct backbone designs have been documented thus far [66–68]. Therefore, the rational design of the conjugated backbone (i.e., repeating units) is critical for improving the PSCs.

The other important part is sidechains, which provide solubility of conjugated polymers in organic solvents, thus providing solution processability. Sidechains can also affect intermolecular interactions and provide optimal mixing with the PCBM to obtain the required morphology. Although side chains in the conjugated polymer design have numerous advantages, they disrupt the π stacking of polymer backbones and chromophore density, thereby impeding the absorption of light and transportation of charges. Furthermore, inappropriate attachment of side chains can cause steric hindrance and twisting of the backbone, resulting in the wider band gap, reducing charge carrier mobility resulting in poor photovoltaic characteristics [61]. Literature studies show that the length and shape of the side chains significantly affect the photovoltaic characteristics of the CP [69,70].

The last constituting part is substituents (e.g., F, Cl, CN, etc.) are frequently utilized to fine-tune the physical properties of CPs, especially their electrical properties (e.g., band-gap, energy levels, mobility, etc.). Because photovoltaic capabilities of the conjugated polymers are highly dependent on their electronic properties, substituents can occasionally significantly impact the PCE of related CPs. Li et al. inserted alkylthio substituents into the benzodithiophene (BDT) unit. They proved that the insertion of alkylthio substituents broadened the absorption and shifted the HOMO energy level of the band gap CPs [71]. Furthermore, Hou et al. designed a thiothienyl substituted BDT as a donor unit and proved that substituted BDT containing polymer shows 0.15 V higher V_{OC} than its nonsubstituted equivalent that improves the PCE [72].

1.10 Donor – Acceptor Approach

Donor-Acceptor type polymers are π -conjugated semiconducting polymers with alternating donor (π electron-rich) and acceptor (π electron-deficient) building blocks, distributed along the backbones of the polymer are known as third-generation semiconducting polymers. According to the literature, there are two milestones in postulating donor-acceptor type polymers.

The first postulation belongs to Wudl et al., who synthesize the first narrow band-gap polymer in the 1980s. The study supported that the bandgap can be modulated if the polymer backbone is made up of an alternating sequence of quinoid and aromatic units [73]. The second postulation was proposed by Yamamoto et al. [74] and demonstrated by Havinga et al. [75] to arrange the bandgap of the polymer, electron releasing (push), and electron-withdrawing (pull) units can be combined. Many recent research studies have confirmed that the above two postulates are linked and applicable to the design of D-A type polymers. In researching highly efficient BHJ polymer photovoltaic devices, molecular engineering of CPs for adjusting the energy band is an important step. PCE of a solar cell is bound with the multiplication of three significant factors: J_{SC} , V_{OC} , and FF. V_{OC} is in direct proportion to the energy difference between the HOMO of the polymer and the LUMO of the fullerene in a device with a BHJ structured active layer. As a result, raising the LUMO of fullerene or lowering the HOMO of the polymer can both enhance the value of V_{OC} . To harvest a larger portion of the solar spectrum, polymers having low band gaps (LBG) are designed. Still, they tend to have low-lying LUMO energy levels and high-lying HOMO energy levels [76]. This situation causes a smaller difference between the HOMO energy level of the polymer and the LUMO energy level of the fullerene, leading to low V_{OC} values. It is required to optimize the band-gap and energy levels of the polymer to obtain BHJ PSCs with high V_{OC} and J_{SC} values at the same time. [77,78]. By adjusting the molecular weight, torsion angles, aromatic resonance energy, bond length alteration, intermolecular interactions, and substituents addition, the HOMO-LUMO band gap (E_g) can be controlled and modified.

Due to the ease of adjusting HOMO and LUMO energy levels and solubility, the synthesis of the CPs containing alternating electron donor (D) and electron acceptor (A) moieties has become an effective method for producing organic semiconductors to apply in BHJ OSCs. To illustrate, placing alternating D-A moieties into the polymer backbone that leading internal charge transfer throughout the conjugated chain enhances the effective resonance length of the π electrons, resulting in lower bandgaps due to the facilitated π electron delocalization through planarization [76].

Because the HOMO and LUMO energy levels are mostly confined to the D and A units, these energy levels can be modified by carefully designing and selecting the D and A units; thus, E_g of CP can also be controlled [79]. For example, to concurrently reduce the HOMO energy level and E_g of a D-A polymer and thus raise V_{OC} and J_{SC} of the device, weakly electron-donating moiety (donor unit) with a strongly electron-withdrawing moiety (acceptor unit) is required. Compared to amorphous polymers, CP with rigid and planar D-A units can construct crystalline structures that enhance charge carriers' mobility and procures greater resistance against the water and oxygen permeability. Recent research on polymer solar cells having crystalline polymers showed that the crystallinity of the CP has a substantial effect on the PCE; crystalline polymers enable transportation of charge carriers, increasing the FF [80–82].

1.11 Effect of π -bridges

Inserting different π -bridges has several advantages. Firstly, aromatic π -bridges are applied to extend the absorption across a sufficiently broad wavelength range. Secondly, the use of conjugated π -bridges can result in a lower E_g value and broad absorption across the entire visible and near-infrared region of the solar spectrum. Thirdly, the introduction of π bridges into the polymer backbone increases the conjugation length that influences both the optical and electronical characteristics of the D-A type LBG polymer. Fourthly, inserting π -bridges increases the crystallinity and J_{SC} while decreasing the steric hindrance [83].

Finally, the ability to select alternative aromatic derivatives of π -bridges is the most effective way to reduce reorganization energy levels [84]. Wang. et al., focusing on the different π - bridges and proved that different π - bridges significantly impact the polymer backbone's electronic structure and the interaction of D and A units. π -bridges affect the stereo structure and, as a result, the D-A conjugated polymer's optical, electrochemical, charge transport, and photovoltaic characteristics [85,86]. It is critical to comprehend the effects of the bridges on the physicochemical and photovoltaic properties of the conjugated polymers to construct effective PSCs. Furthermore, in addition to the film crystallinities and carrier mobilities, Kim et al. evaluated the effects of the bridges on the optical, electrochemical, and photovoltaic properties of the polymers. They prove that using 6-alkylthieno[3,2-b]thiophene π -bridge leads to an enhancement in the FF, J_{sc} , and PCE of the device because of the higher absorption, improved crystallinity, and high hole mobility of the 6-alkylthieno[3,2-b]thiophene incorporated polymer. [87].

1.12 Benzothiadiazole as Acceptor Unit

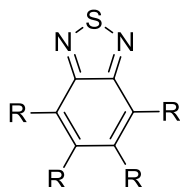


Figure 11 Chemical structure of the benzo[c][2,1,3]thiadiazole

Pilgram et al. were the first to synthesize brominated benzo[c][2,1,3]thiadiazole (BT) in 1970 [88]. However, Meihere et al. designed the first alternating D-A copolymer with BT unit in 1996 [89]. 2,1,3-Benzothiadiazole (BT) is a crucial part of the chemistry of photoluminescent compounds that can be exploited in light technology. Attention has been focused on BT π -extended derivatives with possible usage in this exciting area due to their potential as constituents of OLEDs, OSCs, liquid crystals, dyes, photovoltaic cells, etc. [90,91].

Benzothiadiazole (BT) is an effective electron acceptor; (1) the inclusion of the imine functionalities with low π^* orbitals provide BT with a comparatively high electron affinity (EA). The BT structure can be identified as a quasi-quinoidal structure (shorter π bonds placed in the benzo ring, localized) instead of a ten π electron heteroaromatic system. This situation can boost the electronic coupling between substituents in the 4th and 7th positions compared to that seen across 1,4-substituted aromatic units [92]. (2) Because the heterocyclic system of the BT unit has a high electron-withdrawing capability, molecules with this ring could be used as an electron carrier. (3) BT has enhanced solubility. (4) Due to their highly polarized characteristics, BT compounds are expected to produce well-ordered crystal structures, leading to intermolecular interactions such as heteroatom contacts and $\pi - \pi^*$ interactions [90].

1.13 Benzodithiophene as Donor Unit

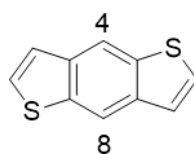


Figure 12 Chemical structure of the benzo[1,2-b:4,5-b']dithiophene

In the early 1980s, the conductivity of the benzo[1,2-b:4,5-b']dithiophene (BDT) moiety was proved and applied to several designs of the molecules [93,94]. Moreover, in 2008 Hou & Yang et al. utilized the BDT unit in the synthesis of PV polymers and proved that BDT moiety is one of the accomplished compounds in the development of highly efficient materials due to its tunable optical and electrochemical properties and intermolecular charge transfer (ICT) between the donor and acceptor [95]. BDT becomes an attractive electron-rich donor unit owing to its several advantages. (1) BDT has high hole mobility due to its π -conjugated structure. Its rigid and planar structure creates highly adjustable molecular energy levels, optical band gaps.

(2) Two thiophene moiety fused with benzene unit in the BDT structure makes it planar. (3) Depending on the side chains, the solubility of the BDT unit can be adjusted. (4) Planar and conjugated molecule structure of the BDT leads to easier π -stacking and has relatively high hole mobility, making BDT-based polymers capable of achieving outstanding photovoltaic characteristics for PSC applications [96]. BDT-based OPV devices attained record PCEs verified by the National Renewable Energy Laboratory (NREL) [97–99].

1.14 Review of Literature

The synthesis of D-A type polymers has piqued attention in photovoltaics [100]. Electron-rich units (donor) and electron-deficient units (acceptor) are bounded with a covalent bond, and these units are repeated through the conjugated polymer chain. The optoelectronic characteristics of D-A type polymers have begun to be tuned using the donor-acceptor (D-A) strategy. This strategy uses intramolecular charge transfer (ICT) between the donor and acceptor units integrated under the same roof to achieve a narrower bandgap, lower oxidation potential, and improved coloration efficiency than traditional strategies. On the other hand, insertion of π bridges into the polymer backbone provides various advantages, including extending the absorption profile, lowering the band gap (E_g), increasing the conjugation length and crystallinity. Therefore, combining two effective strategies has become popular, and D- π bridge-A type conjugated polymers have become widely used in PV applications. Following the pioneering study of Havinga et al., a series of D-A type conjugated polymers containing furan, thiophene, selenophene, and derivatives used as a donor, and benzoxadiazole (BO), benzothiadiazole (BT), benzotriazoles used as acceptor were designed, synthesized, and characterized for different PV application purposes [101]. As electron donors, conjugated polymers having D- π bridge-A architecture are frequently utilized. The characteristics of the conjugated polymer, such as energy levels of the HOMO and LUMO, absorption range, morphology, and charge carrier mobility, can be adjusted by changing the donor and acceptor moieties.

Furthermore, the π bridge, as a part of the polymer backbone, has a significant impact on the molecular structure, optoelectronic and physical characteristics of the polymer. Consequently, selecting the appropriate π bridge may be an essential technique for improving OPV performance. In the light of this knowledge, polymers with three different π -bridges (PT1-PT2-PT3) were synthesized by combining several articles from the literature, and the effect of bridges on the photovoltaic, optical, and electrochemical properties of polymers was investigated in this thesis study

Table 1 Photovoltaic properties of the π bridged polymers in the literature

Polymer	Polymer/PC ₇₁ BM (w:w)	V _{OC} (V)	J _{SC} (mA/cm ²)	FF	PCE (%)	Reference
P(BDT-F-BT)	1:2	0.94	6.50	0.46	2.81	
P(BDT-T-BT)	1:1.5	0.82	9.45	0.48	3.72	[85]
P(BDT-TT-BT)	1:1.5	0.69	11.34	0.63	4.93	
PBDT-TBT	1:1	0.96	9.10	0.51	4.9	
PBDT-TTBT	1:1	0.80	11.83	0.66	6.3	[102]
PBDTS	1:2	0.73	7.37	0.60	3.24	[103]
PBDTSe	1:2	0.65	8.62	0.54	3.05	

Table 2 Optical & electrochemical properties of π bridged polymers in literature

Polymer	E_g^{opt} (eV)	HOMO (eV)	LUMO (eV)	E_g^{CV} (eV)	Reference
P(BDT-F-BT)	1.96	-5.44	-3.48	1.96	
P(BDT-T-BT)	1.82	-5.35	-3.44	1.91	[85]
P(BDT-TT-BT)	1.78	-5.21	-3.54	1.66	
PBDT-TBT	1.79	-5.27	-3.48	1.79	
PBDT-TTBT	1.73	-5.09	-3.36	1.73	[102]
PBDTS	1.81	-5.32	-3.26	2.06	[103]
PBDTSe	1.71	-5.29	-3.33	1.96	

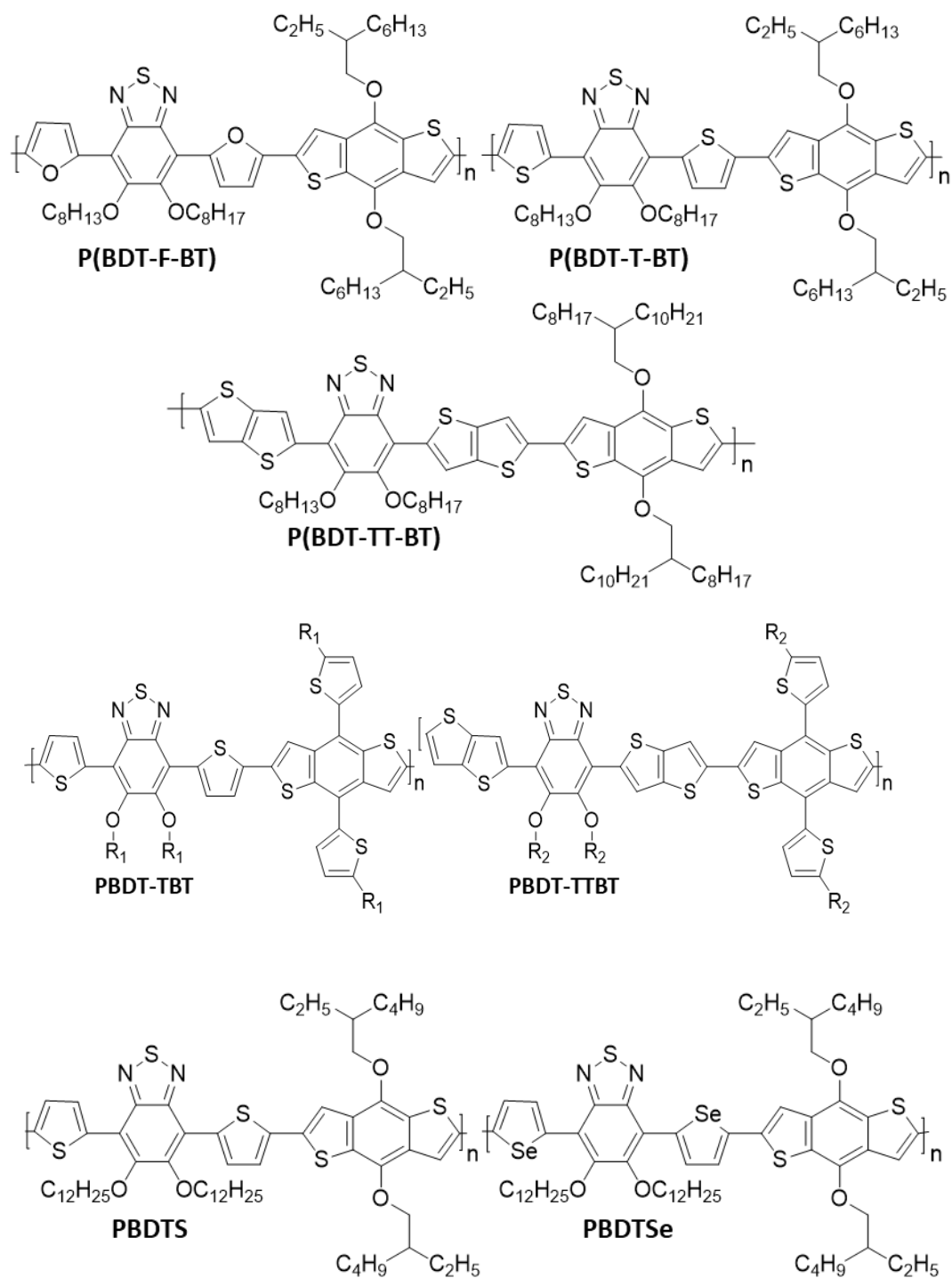


Figure 13 Molecular structures of the π -bridged polymers in the literature.

As represented in Figure 13, there has been a lot of study in the literature using Benzothiadiazole (BT) as the acceptor unit, Benzodithiophene (BDT) with various substituents as the donor unit, and thiophene, selenophene, furan, and the thiophene as the π bridges [85,102,103]. As clarified in chapters 1.12 and 1.13, BDT and BT were selected as donor-acceptor couples since they ensure polymers with broad absorbance and appropriate molecular energy levels for harvesting sunlight, separation, and transportation of charges in the polymer.

1.15 Aim of the Study

Strong electron-withdrawing units (acceptor moiety) reduce LUMO energy levels, giving rise to the formation of LBG polymers. Benzothiadiazole (BT) is one of the most common and stronger acceptor parts stated in the literature. BT has a quasi-quinoidal structure that can adopt a quinoid system, and it also has a high electron-withdrawing property, making it a desirable part of polymer synthesis. Additionally, insertion of different π -bridges into the polymer backbone extends the absorption range, increases the conjugation length and crystallinity, reduces the steric hindrance. Therefore, 2,1,3-Benzothiadiazole (BT) bearing, D- π bridges-A type conjugated polymers were designed and synthesized via Stille crosscoupling reactions for usage in OSCs. In this thesis study, three-D- π bridges-A type conjugated polymers PT1, PT2, and PT3 with 2,1,3-thiadiazole (BT) as the acceptor unit and benzo[1,2-b:4,5-b']dithiophene (BDT) as the donor unit were synthesized. To demonstrate the electron-donating properties of thiophene, selenophene, and thienothiophene, the effect of different π -bridges on conjugated polymers was examined. The polymer characterizations were carried out using a conventional OSC device architecture. The PT1 with thiophene, PT2 with selenophene, and PT3 with thienothiophene bearing polymers were characterized electrochemically, optically, thermally, and photovoltaically. The gel permeation chromatography (GPC) technology was used to estimate the molecular weight of the polymers. The polymer structures are shown in Figure 14.

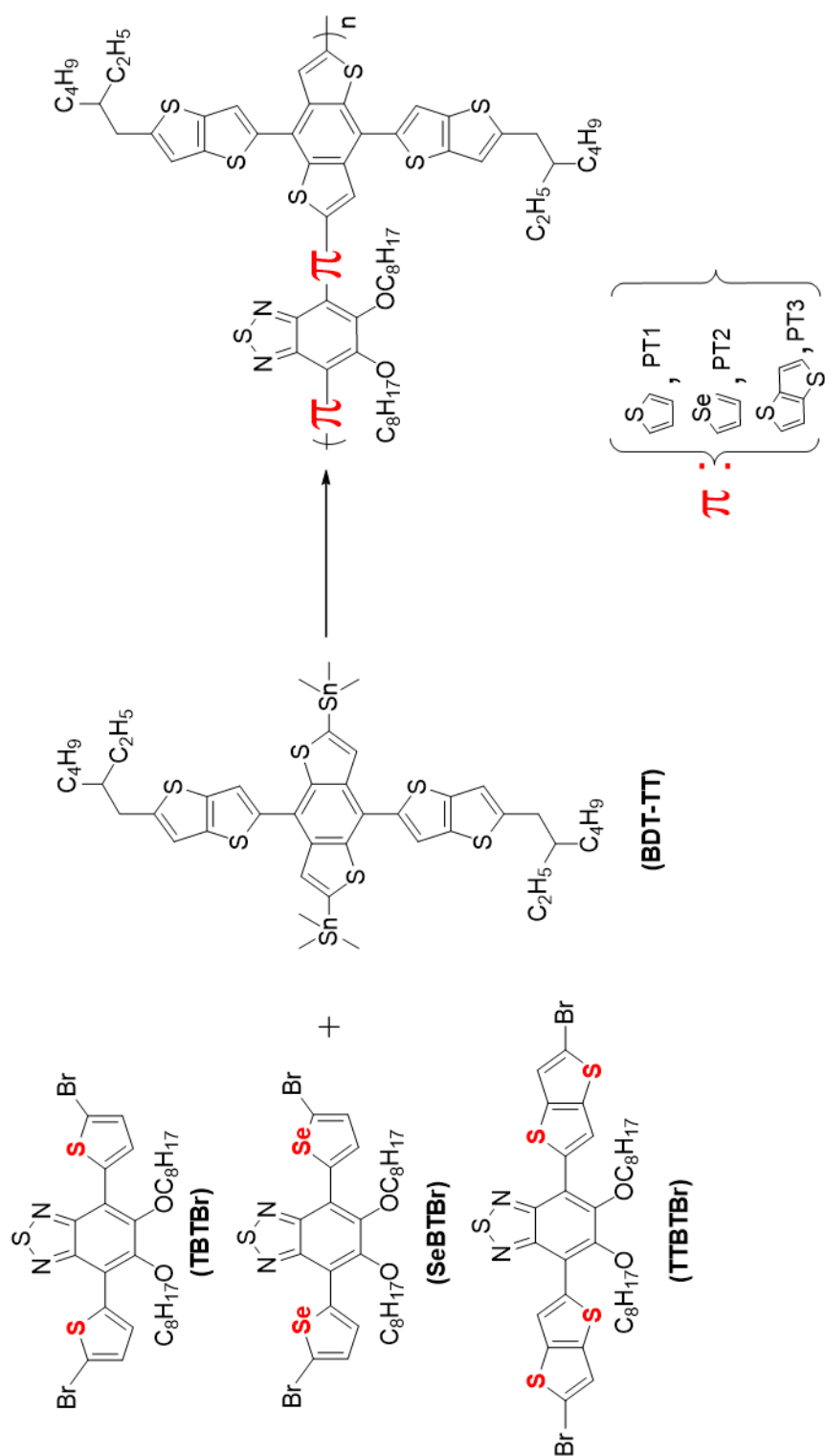


Figure 14 Synthesized polymer structures

CHAPTER 2

EXPERIMENTAL

2.1 Materials and Methods

All chemicals and solvents were purchased from Sigma-Aldrich except glacial acetic acid from Carlo Erba, and fuming nitric acid from Merck. All reactions were performed under nitrogen atmosphere unless otherwise specified. THF, toluene, triethylamine and DMF were distilled freshly and dried over Na/benzophenone ketyl before use. All monomer units which are named as 4,7-bis(5-bromothiophen-2-yl)-5,6-bis(octyloxy)benzo[*c*][1,2,5]thiadiazole (TBTBr), 4,7-bis(5-bromoselenophen-2-yl)-5,6-bis(octyloxy)benzo[*c*][1,2,5]thiadiazole (Se-(BTBr)) and 4,7-bis(5-bromothiopheno[3,2-*b*]thiophen-2-yl)-5,6-bis(octyloxy)-benzo-[*c*][1,2,5]thiadiazole (TTBTBr) were synthesized according to the previously mentioned methods [85,104–106]. A Bruker Spectrospin Avance DPX-400 Spectrometer was used to perform ^1H and ^{13}C NMR analysis. The chemical shift data for each signal were specified in units of δ (ppm) relative to tetramethylsilane (TMS) where δ (TMS) = 0. Splittings were designated as s (singlet), d (doublet), t (triplet), dd (doublet of doublet), and m (multiplet). Column chromatography was conducted with Merck Silica Gel 60 (Particle size: 0.040–0.063 mm, 230–400 mesh ASTM). For Gel permeation chromatography (GPC) measurements, Shimadzu LC-20AT instrument was used to determine number average (M_n), and weight average (M_w) molecular weights in chloroform solvent and polystyrene was used as a universal standard. A JASCO V-770 UV-Vis spectrophotometer was used to conduct optical studies in both solutions in chloroform and the thin film of polymers. All electrochemical characterization studies were performed using a GAMRY Reference 600 potentiostat.

2.2 Synthesis

2.2.1 Synthesis of Monomers

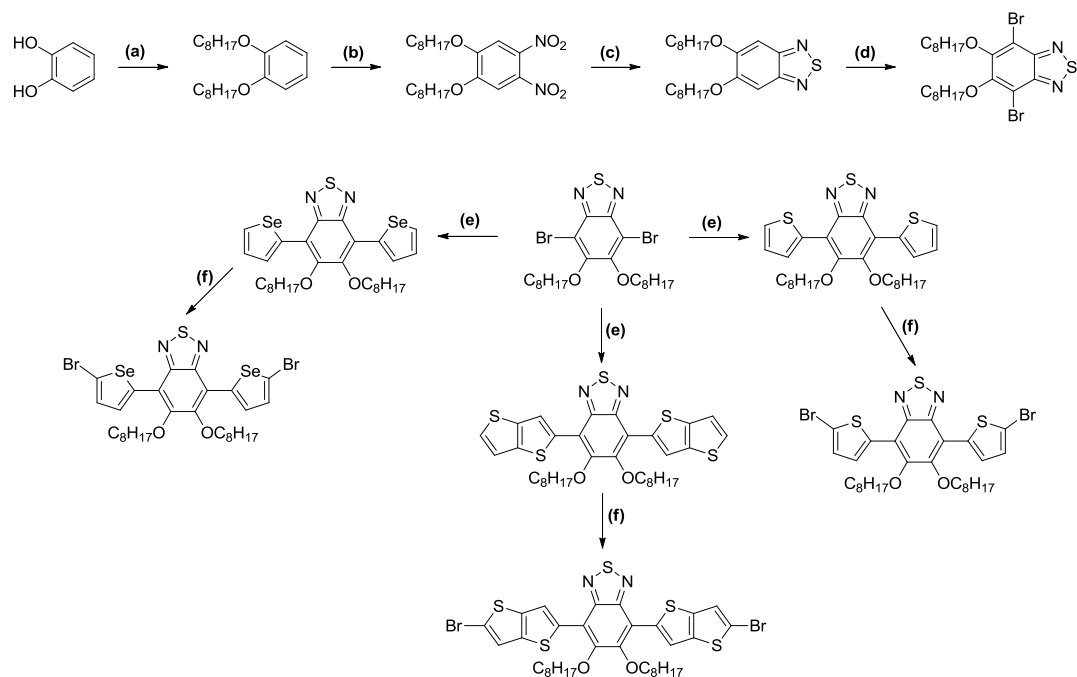


Figure 15 Synthetic pathway of the monomers: TBTBr, SeBTBr, and TTBTBr

(a) K₂CO₃, 1-Bromooctane, DMF, 115 °C, 72 h. (b) 65% HNO₃, 97% HNO₃, HOAc, DCM, RT, 48 h. (c)-(i) Pd/C, Hydrazine monohydrate, ethanol, 70 °C, overnight (c)-(ii) N-thionyl aniline, Triethylamine, toluene, 120 °C, 3 h. (d) Br₂, HOAc, CHCl₃, RT, 72h. (e) PdCl₂(PPh₃)₂, dry THF, 66 °C, 48 h. (f) NBS, CHCl₃, HOAc, RT, 24 h.

2.2.1.1 Synthesis of 1,2-bis(octyloxy)benzene (1)

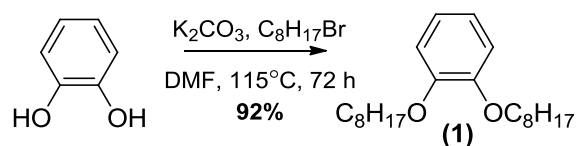


Figure 16 Synthesis of compound (1)

Pyrocatechol (5.0 g, 45.41 mmol) and K_2CO_3 (18.8 g, 136.03 mmol) were dissolved in DMF solvent, stirred at room temperature for 1 hour. Then, 1-bromooctane (21.9 g, 113.4 mmol) was added to the reaction medium and stirred for 72 hours at $115^\circ C$ under an inert atmosphere. DMF was removed using a rotary evaporator, and the crude product was extracted with dichloromethane and brine more than once. The organic phases were collected and dried over with $MgSO_4$. The organic solvent was evaporated under reduced pressure. The milky brown product was recrystallized from cold methanol and filtered to obtain a white solid. (14.0 g, 92.2%). 1H NMR (400 MHz, $CDCl_3$): δ (ppm) 6.90 (s, 4H), 4.01 (t, $J = 6.7$ Hz, 4H), 1.87 – 1.78 (m, 4H), 1.53 – 1.25 (m, 20H), 0.91 (t, $J = 8.8, 4.9$ Hz, 6H). ^{13}C NMR (100 MHz, $CDCl_3$): δ (ppm) 149.2, 121.0, 114.0, 69.3, 31.9, 29.4, 29.4, 29.3, 26.1, 22.7, 14.1.

2.2.1.2 Synthesis of 1,2-dinitro-4,5-bis(octyloxy)benzene (2)

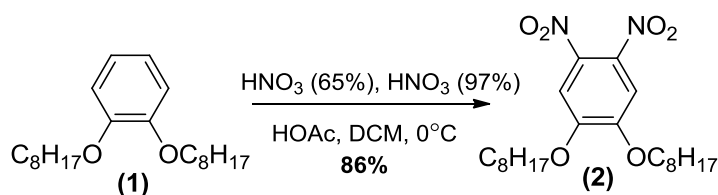


Figure 17 Synthesis of compound (2)

1,2-Bis(octyloxy)benzene (10.5 g, 31.4 mmol) was dissolved in a mixture of glacial acetic acid (150 mL) and dichloromethane (150 mL) then the reaction medium was cooled to 0 °C in an ice-bath. HNO₃ (65%, 25 mL) was added dropwise to the reaction, then stirred at room temperature for 1.5 hours. The reaction medium was cooled to 0 °C again, and fuming nitric acid (97%, 70 mL) was added dropwise to the reaction medium and stirred for 48 hours. The reaction medium was poured into an ice-water mixture and extracted with dichloromethane. The organic layer was extracted with aqueous NaHCO₃ solution, water, and brine. Organic phases were dried with MgSO₄, and the organic solvent was evaporated under reduced pressure. Yellow crystalline solid was obtained after recrystallization with hot ethanol. (11.5 g, 86.3%). ¹H NMR (400 MHz, CDCl₃): δ (ppm) 7.29 (s, 2H), 4.09 (t, *J* = 6.5 Hz, 4H), 1.90 – 1.84 (m, 4H), 1.52 – 1.26 (m, 20H), 0.88 (t, *J* = 6.8 Hz, 6H). ¹³C NMR (100 MHz, CDCl₃): δ (ppm) 151.8, 136.5, 107.9, 70.2, 31.8, 29.2, 29.0, 28.7, 25.8, 22.6, 14.1.

2.2.1.3 Synthesis of 5,6-bis(octyloxy)benzo[c][1,2,5]thiadiazole (3)

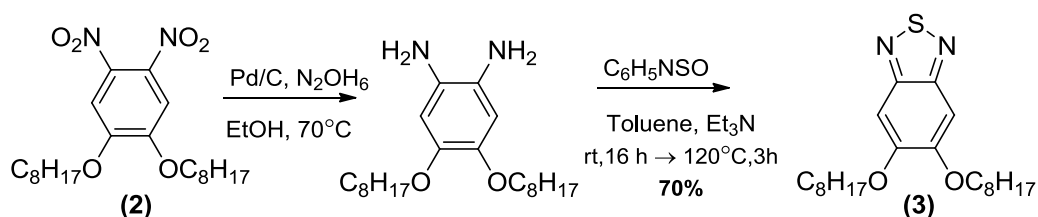


Figure 18 Synthesis of compound (3)

1,2-Dinitro-4,5-bis(octyloxy)benzene (1.5 g, 3.53 mmol), palladium on carbon (0.113 g, 1.06 mmol) were dissolved in ethanol (30 mL) and stirred for 1 hour under inert atmosphere at room temperature. Hydrazine monohydrate (0.113 g, 3.53 mmol) was added drop by drop to the reaction medium, and the medium was heated up to 70 °C. The dark red reaction medium was refluxed overnight. Celite was used to filter the reaction medium for removing Pd/C, and the medium was washed with hot ethanol using the Buchner funnel. The resulting ethanol was evaporated under reduced pressure to yield an off-white solid. The solid was kept under vacuum-argon cycles. Since diamine is quite unstable, easily decomposes with air, and is highly air-sensitive, an off-white solid was immediately used for the next reaction. Schlenk tube was loaded with 1,2-diamino-4,5-bis(octyloxy)benzene and dissolved in dry toluene (12 mL) and freshly distilled triethylamine (12 mL). The reaction mixture was degassed under a nitrogen atmosphere. N-thionyl aniline (1.05 g, 7.54 mmol) was added dropwise to the reaction medium and stirred for 16 hours at room temperature. Then, the medium was heated up to 120 °C for 3 hours. The reaction solvent was evaporated, and the crude product was poured into distilled water. The crude product was filtered then recrystallized from ethanol to obtain an off-white solid. (0.9 g, 70.0%). ¹H NMR (400 MHz, CDCl₃): δ (ppm) 7.13 (s, 2H), 4.09 (t, J = 6.6 Hz, 4H), 1.94 – 1.88 (m, 4H), 1.54 – 1.29 (m, 20H), 0.89 (t, J = 6.8 Hz, 6H). ¹³C NMR (100 MHz, CDCl₃): δ (ppm) 154.1, 151.4, 98.4, 69.1, 31.8, 29.3, 29.3, 28.7, 26.0, 22.7, 14.1.

2.2.1.4 Synthesis of 4,7-dibromo-5,6-bis(octyloxy)benzo[*c*][1,2,5]thiadiazole (4)

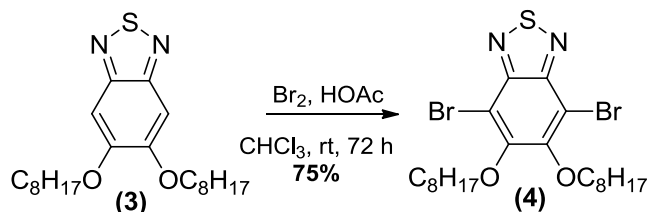


Figure 19 Synthesis of compound (4)

5,6-Bis(octyloxy)benzo[*c*][1,2,5]thiadiazole (1.5 g, 3.82 mmol) was dissolved in a mixture of acetic acid (10 mL) and chloroform (80 mL). Molecular bromine (1.37 mL, 27 mmol) was added dropwise to the reaction medium and stirred for 72 hours in the dark. The reaction medium was poured into an aqueous NaOH solution then extracted with dichloromethane and brine several times. The organic layer was dried over by using MgSO₄, and the organic solvent was evaporated under reduced pressure. The crude product was chromatographically purified on a silica gel column eluting with dichloromethane: hexane (1:3) to afford a white crystalline solid. (1.57 g, 74.7%). ¹H NMR (400 MHz, CDCl₃): δ (ppm) 4.16 (t, J = 6.7 Hz, 4H), 1.92 – 1.83 (m, 4H), 1.58 – 1.29 (m, 20H), 0.90 (t, J = 6.8 Hz, 6H). ¹³C NMR (100 MHz, CDCl₃): δ (ppm) 154.5, 150.4, 106.3, 75.2, 31.8, 30.3, 29.4, 29.3, 26.0, 22.7, 14.1.

2.2.1.5 Synthesis of 5,6-bis(octyloxy)-4,7-di(thiophen-2-yl)benzo[*c*][1,2,5]thiadiazole (TBT)

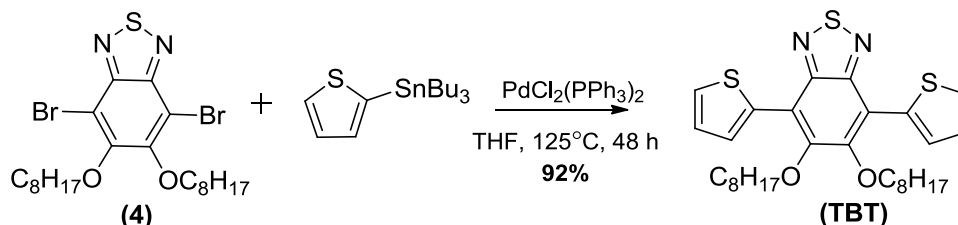


Figure 20 Synthesis of TBT

4,7-Dibromo-5,6-bis(octyloxy)benzo[*c*][1,2,5]thiadiazole (0.8 g, 1.45 mmol) and tributyl(thiophen-2-yl)stannane (1.2 g, 3.22 mmol) were loaded into the Schlenk tube, degassed three times under a nitrogen atmosphere then dissolved in dry THF solvent (30 mL) under inert atmosphere. $\text{PdCl}_2(\text{PPh}_3)_2$ (0.2 g, 0.285 mmol) was added to the reaction medium and the reaction medium was heated to 125°C to reflux for 48 hours. The reaction solvent was evaporated under reduced pressure. The crude product was chromatographically purified on a silica gel column to afford orange crystalline solid. (0.742 g, 92.0%). ^1H NMR (400 MHz, CDCl_3): δ (ppm) 8.47 (dd, $J = 3.8, 0.9$ Hz, 2H), 7.51 (dd, $J = 5.2, 1.0$ Hz, 2H), 7.23 (dd, $J = 5.1, 3.8$ Hz, 2H), 4.11 (t, $J = 7.1$ Hz, 4H), 1.96 – 1.89 (m, 4H), 1.44 – 1.29 (m, 20H), 0.91 (t, $J = 6.9, 4.5$ Hz, 6H). ^{13}C NMR (100 MHz, CDCl_3): δ (ppm) 151.9, 150.9, 134.0, 130.4, 127.2, 126.6, 117.5, 74.3, 31.7, 30.2, 29.4, 29.2, 25.8, 22.6, 13.9.

2.2.1.6 Synthesis of 5,6-bis(octyloxy)-4,7-di(selenophen-2-yl)benzo[*c*][1,2,5]thiadiazole (SeBT)

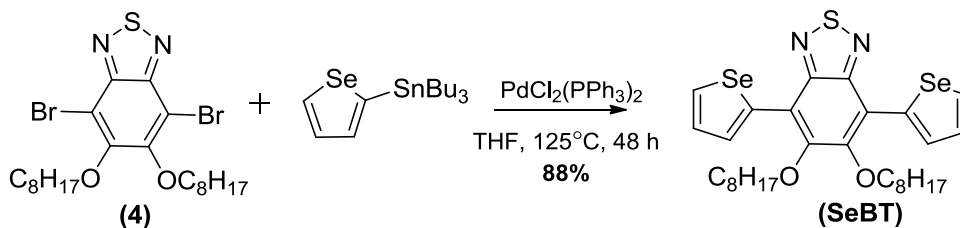


Figure 21 Synthesis of SeBT

4,7-Dibromo-5,6-bis(octyloxy)benzo[*c*][1,2,5]thiadiazole (0.5 g, 0.908 mmol) and tributyl(selenophen-2-yl)stannane (0.86 g, 2.05 mmol) were loaded into the Schlenk tube, degassed three times under a nitrogen atmosphere then dissolved in dry THF solvent (30 mL) under inert atmosphere. PdCl₂(PPh₃)₂ (0.13 g, 0.118 mmol) was added to the reaction medium and the reaction medium was heated to 125 °C to reflux for 48 hours. The reaction solvent was evaporated under reduced pressure. The crude product was chromatographically purified on a silica gel column to afford orange crystalline solid. (0.521 g, 88.1%). ¹H NMR (400 MHz, CDCl₃): δ (ppm) 8.86 (d, *J* = 4.3 Hz, 2H), 8.22 (d, *J* = 4.3 Hz, 2H), 7.49 (dd, *J* = 5.7, 4.1 Hz, 2H), 4.14 (t, *J* = 7.3 Hz, 4H), 2.00 – 1.92 (m, 4H), 1.47 – 1.25 (m, 20H), 0.89 (t, *J* = 6.3 Hz, 6H). ¹³C NMR (10 MHz, CDCl₃) δ (ppm) 150.9, 150.1, 140.2, 133.1, 132.8, 120.1, 118.6, 74.8, 31.8, 30.5, 29.5, 29.3, 25.9, 22.7, 14.1.

2.2.1.7 Synthesis of 5,6-bis(octyloxy)-4,7-di(thieno[3,2-*b*]thiophen-2-yl)benzo[*c*][1,2,5]thiadiazole (TTBT)

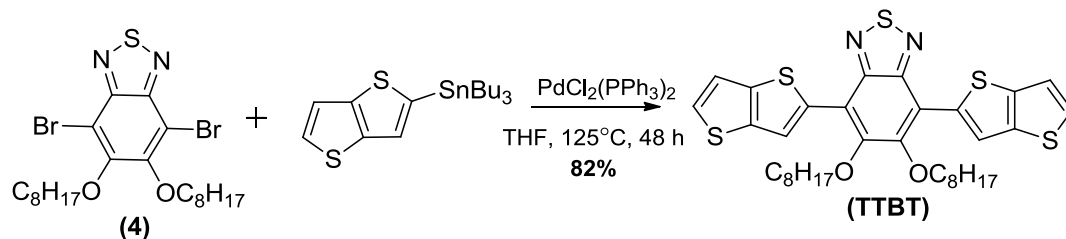


Figure 22 Synthesis of TTBT

4,7-Dibromo-5,6-bis(octyloxy)benzo[*c*][1,2,5]thiadiazole (0.4 g, 0.726 mmol) and tributyl(thieno[3,2-*b*]thiophen-2-yl)stannane (1.14 g, 2.66 mmol) were loaded into the Schlenk tube, degassed three times under a nitrogen atmosphere then dissolved in dry THF solvent (30 mL) under inert atmosphere. PdCl₂(PPh₃)₂ (0.1 g, 0.142 mmol) was added to the reaction medium and the reaction medium was heated to 125 °C to reflux for 48 hours. The reaction solvent was evaporated under reduced pressure. The crude product was chromatographically purified on a silica gel column to afford orange crystalline solid. (0.4 g, 82.3%). ¹H NMR (400 MHz, CDCl₃): δ (ppm) 8.81 (d, *J* = 0.6 Hz, 2H), 7.46 (d, *J* = 5.1, 1.5 Hz, 2H), 7.33 (dd, *J* = 5.2, 0.7 Hz, 2H), 4.16 (t, *J* = 7.1 Hz, 4H), 2.00 – 1.95 (m, 4H), 1.48 – 1.29 (m, 20H), 0.90 (t, *J* = 6.9 Hz, 6H). ¹³C NMR (100 MHz, CDCl₃): δ (ppm) 151.9, 150.8, 141.3, 139.2, 136.2, 128.2, 122.9, 119.3, 117.9, 74.6, 31.7, 30.3, 29.4, 29.2, 25.9, 22.6, 14.0.

2.2.1.8 Synthesis of 4,7-bis(5-bromothiophen-2-yl)-5,6-bis(octyloxy)benzo[c][1,2,5]thiadiazole (TBTBr)

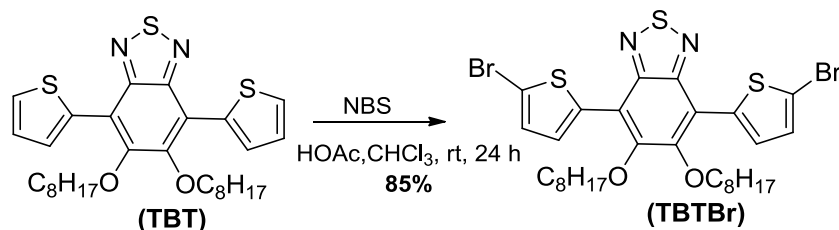


Figure 23 Synthesis of TBTBr

5,6-Bis(octyloxy)-4,7-di(thiophen-2-yl)benzo[c][1,2,5]thiadiazole (0.82 g, 1.47 mmol) was dissolved in chloroform (40 mL) and acetic acid (15 mL) under inert atmosphere. Then, N-bromosuccinimide (NBS) (0.58 g, 3.28 mmol) was dissolved in dry chloroform (10 mL), added to the reaction medium dropwise, and stirred for 24 hours in the dark. The reaction medium was extracted with chloroform and brine. Organic phases were collected and dried over by using MgSO₄. The organic phases were removed under reduced pressure. The crude product was chromatographically purified on a silica gel column eluting with chloroform: hexane to afford a red crystalline solid. (0.895 g, 85.3%). ¹H NMR (400 MHz, CDCl₃): δ (ppm) 8.36 (d, J = 4.1 Hz, 2H), 7.17 (d, J = 4.1 Hz, 2H), 4.12 (t, J = 7.2 Hz, 4H), 1.98 – 1.90 (m, 4H), 1.46 – 1.30 (m, 20H), 0.91 (t, J = 6.8 Hz, 6H). ¹³C NMR (100 MHz, CDCl₃): δ (ppm) 151.5, 150.4, 135.7, 131.0, 129.7, 117.0, 115.5, 74.6, 31.8, 30.3, 29.5, 29.3, 25.9, 22.7, 14.1.

2.2.1.9 Synthesis of 4,7-bis(5-bromoselenophen-2-yl)-5,6-bis(octyloxy)benzo[c][1,2,5]thiadiazole (SeBTBr)

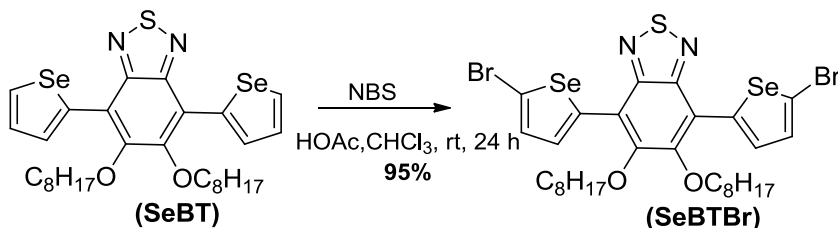


Figure 24 Synthesis of SeBTBr

5,6-Bis(octyloxy)-4,7-di(selenophen-2-yl)benzo[c][1,2,5]thiadiazole (0.42 g, 0.645 mmol) was dissolved in chloroform (20 mL) and acetic acid (5 mL) under inert atmosphere. Then, N-bromosuccinimide (NBS) (0.23 g, 1.3 mmol) was dissolved in chloroform (5 mL), added to the reaction medium dropwise, and stirred for 24 hours in the dark. The reaction medium was extracted with chloroform and brine. Organic phases were collected and dried over by using MgSO₄. The organic phases were removed under reduced pressure. The crude product was chromatographically purified on a silica gel column eluting with chloroform: hexane to afford a red crystalline solid. (0.496 g, 95.0%). ¹H NMR (400 MHz, CDCl₃): δ (ppm) 8.66 (d, *J* = 4.4 Hz, 2H), 7.39 (d, *J* = 4.4 Hz, 2H), 4.14 (t, *J* = 7.4 Hz, 4H), 1.99 – 1.93 (m, *J* = 15.0, 7.5 Hz, 4H), 1.46 – 1.30 (m, 20H), 0.89 (t, *J* = 7.0 Hz, 6H). ¹³C NMR (100 MHz, CDCl₃): δ (ppm) 151.0, 150.1, 140.0, 133.1, 132.8, 120.1, 118.7, 74.8, 31.8, 30.5, 29.5, 29.3, 25.9, 22.7, 14.1

2.2.1.10 Synthesis of 4,7-bis(5-bromothieno[3,2-*b*]thiophen-2-yl)-5,6-bis(octyloxy)-benzo-*c*[[1,2,5] thiadiazole (TTBTBr)

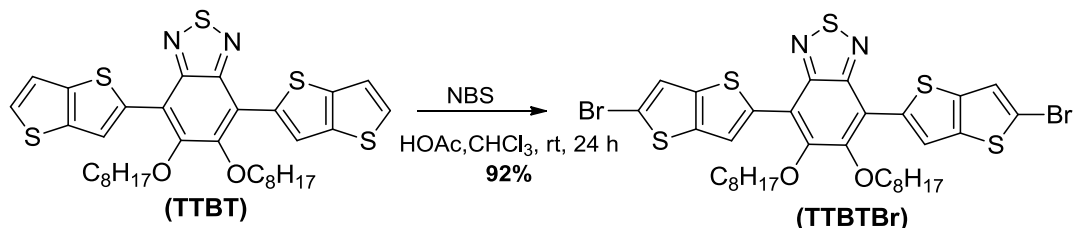


Figure 25 Synthesis of TTBTBr

5,6-Bis(octyloxy)-4,7-di(thieno[3,2-*b*]thiophen-2-yl)benzo-*c*[[1,2,5]thiadiazole (0.36 g, 0.538 mmol) was dissolved in chloroform (30 mL) and acetic acid (10 mL) under inert atmosphere. Then, N-bromosuccinimide (NBS) (0.2 g, 1.13 mmol) was dissolved in dry chloroform (5 mL), added to the reaction medium dropwise, and stirred for 24 hours in the dark. The reaction medium was extracted with chloroform and brine. Organic phases were collected and dried over by using MgSO₄. The organic phases were removed under reduced pressure. The crude product was chromatographically purified on a silica gel column eluting with chloroform: hexane to afford a red crystalline solid. (0.41 g, 92.0%). ¹H NMR (400 MHz, CDCl₃): δ (ppm) 8.74 (s, 2H), 7.32 (s, 2H), 4.13 (t, *J* = 7.0 Hz, 4H), 1.98 – 1.94 (m, 4H), 1.45 – 1.29 (m, 20H), 0.90 (t, *J* = 5.2 Hz, 6H). ¹³C NMR (101 MHz, CDCl₃) δ (ppm) 151.6, 150.4, 140.0, 139.4, 135.3, 122.4, 122.1, 117.4, 114.6, 74.7, 31.7, 30.2, 29.4, 29.2, 25.9, 22.6, 14.0.

2.2.2 Synthesis of Polymers

2.2.2.1 Synthesis of PT1

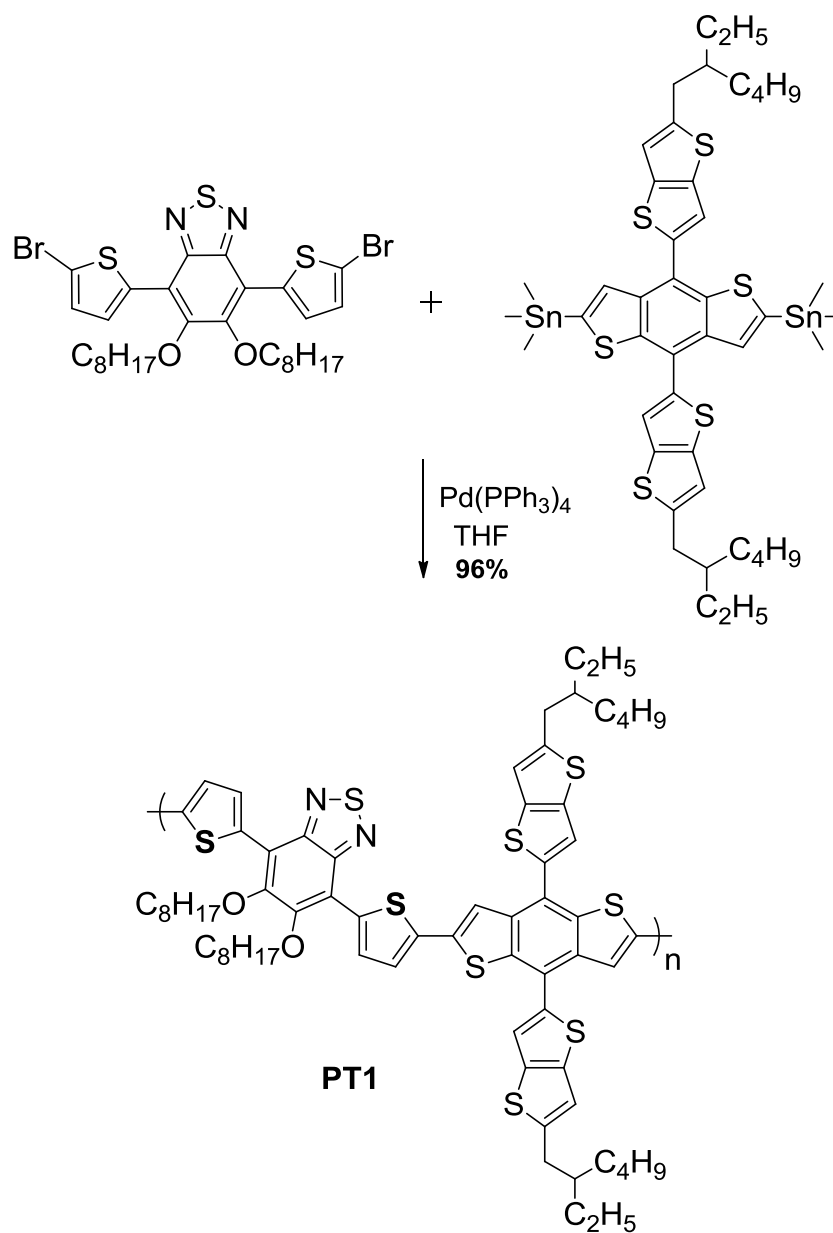


Figure 26 Synthesis of PT1

In a 25 mL Schlenk tube, 4,7-bis(5-bromothiophen-2-yl)-5,6-bis(octyloxy)benzo[*c*]-[1,2,5] thiadiazole (TBTBr) (0.15 g, 0.209 mmol) and 2,6-bis(trimethyltin)-4,8-bis(2-ethylhexyl) thieno[3,2-*b*]thiophene)-benzo[1,2-*b*:4,5-*b'*]dithiophene (0.213 g, 0.209 mmol) were added and degassed with nitrogen for 1 hour. After adding anhydrous THF (7 mL), the mixture was stirred under an inert atmosphere for another 1 hour. Then, tetrakis(triphenylphosphine)palladium (0) (0.012 g, 0.01 mmol) was added into the reaction medium, and the mixture was heated at 65 °C for 11 hours. The reaction was ended by TLC checking and cooled to room temperature. The reaction medium was poured into cold methanol, then sodium diethyldithiocarbamate trihydrate (0.02 g) was added as a palladium scavenger, stirred vigorously for 1 hour. The crude form of the polymer was collected by filtration and washed with methanol, acetone, hexane by using a Soxhlet funnel for removing oligomeric fractions. The polymer was recovered from chloroform and evaporated under reduced pressure. The solid product was dissolved in a minimal amount of chloroform and added to a beaker of cold methanol (300 mL) drop by drop to reprecipitate polymer. The precipitate was filtered and dried under a vacuum to obtain a purple solid. Yield: 96.2%. M_w : 85.8 kDa, M_n : 66.6 kDa, PDI: 1.29. ^1H NMR (400 MHz, CDCl_3 , δ : ppm) 7.40-7.10 (thiophene, BDT), 3.85-3.70 (-OCH₂), 2.15-0.8 (alkyl).

2.2.2.2 Synthesis of PT2

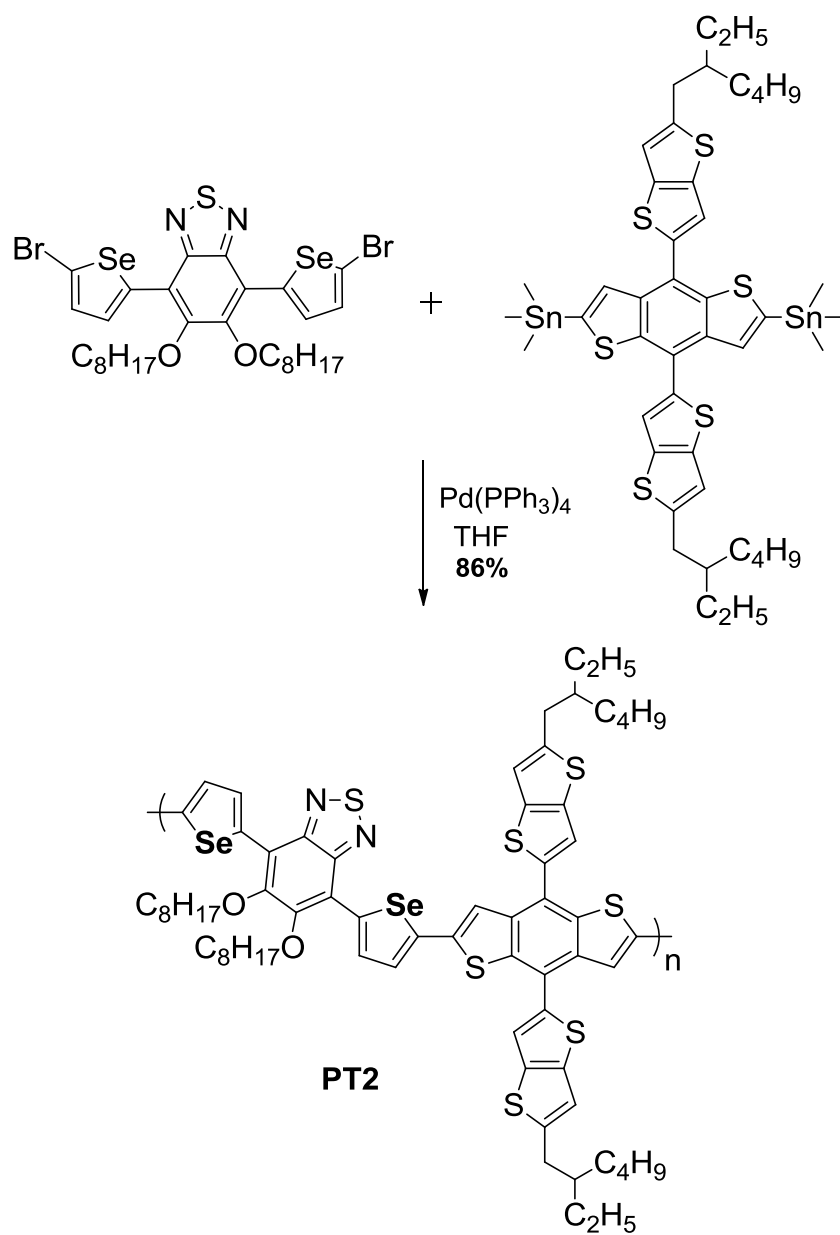


Figure 27 Synthesis of PT2

In a 25 mL Schlenk tube, 4,7-bis(5-bromoselenophen-2-yl)-5,6-bis(octyloxy)benzo[*c*] [1,2,5]thiadiazole (SeBTBr) (0.15 g, 0.185 mmol), and 2,6-bis(trimethyltin)-4,8-bis(2-ethylhexyl)thieno[3,2-*b*]thiophene)-benzo[1,2-*b*:4,5-*b'*]dithiophene were added, and degassed with nitrogen for 1 hour. After adding anhydrous THF (7 mL), the mixture was stirred under an inert atmosphere for another 1 hour. Then, tetrakis(triphenylphosphine)palladium(0) (0.0107 g, 0.009 mmol) was added into the reaction medium and the mixture was heated at 65 °C for 11 hours. The reaction was ended by TLC checking and cooled to room temperature. The reaction medium was poured into cold methanol, then sodium diethyldithiocarbamate trihydrate (0.02 g) was added as a palladium scavenger, stirred vigorously for 1 hour. The crude form of the polymer was collected by filtration and washed with methanol, acetone, hexane by using a Soxhlet funnel for removing oligomeric fractions. The polymer was recovered from chloroform and evaporated under reduced pressure. The solid product was dissolved in a minimal amount of chloroform and added to a beaker of cold methanol (300 mL) drop by drop to reprecipitate polymer. The precipitate was filtered and dried under a vacuum to obtain a blue solid. Yield: 86.5%. M_w : 82.2 kDa, M_n : 65.6 kDa, PDI: 1.25. ^1H NMR (400 MHz, CDCl_3 , δ : ppm): 7.32-7.26 (selenophene, BDT), 3.78 (- OCH_2), 2.20-0.85 (alkyl).

2.2.2.3 Synthesis of PT3

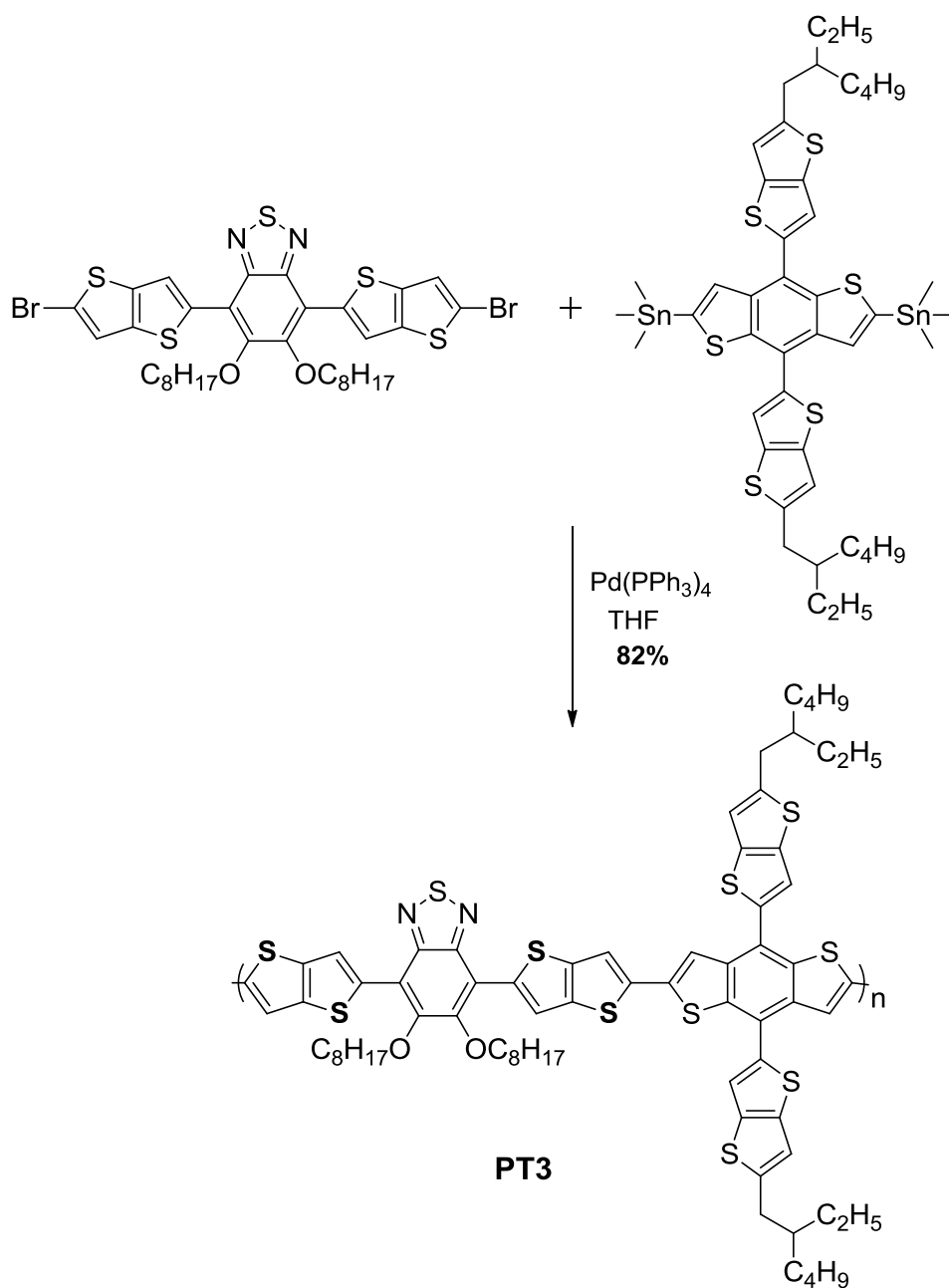


Figure 28 Synthesis of PT3

In a 25 mL Schlenk tube, 4,7-bis(5-bromothieno[3,2-*b*]thiophen-2-yl)-5,6-bis(octyloxy)benzo-[*c*][1,2,5]thiadiazole (TTBTBr) (0.15 g, 0.181 mmol), and 2,6-bis(trimethyltin)-4,8-bis(2-ethylhexyl)thieno[3,2-*b*]thiophene)-benzo[1,2-*b*:4,5-*b'*]dithiophene (0.184 g, 0.181 mmol) were added and degassed with nitrogen for 1 hour. After adding anhydrous THF (7 mL), the mixture was stirred under an inert atmosphere for another 1 hour. Then tetrakis(triphenylphosphine)palladium (0) (0.0105 mg, 0.009 mmol) was added into the reaction medium and the mixture was heated at 65 °C for 11 hours. The reaction was ended by TLC checking and cooled to room temperature. The reaction medium was poured into cold methanol, then sodium diethyldithiocarbamate trihydrate (0.02 g) was added as a palladium scavenger, stirred vigorously for 1 hour. The crude form of the polymer was collected by filtration and washed with methanol, acetone, hexane, chloroform by using a Soxhlet funnel for removing oligomeric fractions. Distinctively from PT1 and PT2, PT3 was recovered from chlorobenzene and evaporated under reduced pressure. The solid product was dissolved in a minimal amount of chlorobenzene and added to a beaker of cold methanol (300 mL) drop by drop to precipitate the polymer. The precipitate was filtered and dried under a vacuum to obtain a purple solid. Yield: 82.0 %. M_w : 266.7 kDa, M_n : 147.4 kDa, PDI: 1.81. $^1\text{H NMR}$ (400 MHz, CDCl_3 , δ : ppm): 7.33-7.27 (thieno[3,2-*b*]thiophene, BDT), 3.82-3.73 (-OCH₂), 1.9-0.8 (alkyl).

2.3 Characterizations of Polymers

2.3.1 Gel Permeation Chromatography

Gel permeation chromatography (GPC) is performed to measure the molecular weight of the polymer samples and the distribution of the molecular weights. Polymer samples were dissolved in chloroform (2.0 mg/mL), weight average molecular weight (M_w), and number average molecular weight (M_n) information were obtained from the chromatogram. Moreover, polydispersity index (PDI) that is the measurement of the heterogeneity of the polymer size, is also calculated from the ratio of M_w to M_n [107].

2.3.2 Thermal Analysis

Thermal analysis (TA) is a term used to describe methodologies for determining the properties of materials as a function of temperature. The thermogravimetric analyzer (TGA) continually measures the mass changes (gain or loss) of the polymer as a function of temperature. Decomposition temperature (T_d) that 5% weight loss is observed by the TGA instrument. Differential scanning calorimetry (DSC) is a thermoanalytical technique that measures the difference in heat capacity of the polymer sample as a function of temperature by heating or cooling. Both melting point temperature (T_m) and the glass temperature (T_g) of the polymers are determined by DSC analysis [108].

2.3.3 Cyclic Voltammetry

Cyclic voltammetry (CV) is widely used electrochemical technique for studying the reduction and oxidation processes of conjugated polymers. Additionally, CV provides qualitative information regarding CPs, such as p- or n-type doping and de-doping potentials, as well as process reversibility. Voltammograms or cyclic voltammograms are represented in Figure 29 (a). The x-axis shows a system parameter, the applied potential (E), while the y-axis represents the response, the consequent current (i) passed. Figure 29 (b) shows a schematic illustration of an electrochemical cell. A three-electrode (working electrode (WE), counter electrode (CE), and reference electrode (RE)) cell is commonly used in CV measurements to segregate the roles of referencing the applied potential and balancing the current produced. The potentiostat is used to apply the desired potential to WE in relation to RE. This process generates a current that flows between the WE and CE. The cell is filled with a solvent called a supporting electrolyte mixture, and three electrodes are inserted. The solvent should dissolve the supporting electrolyte while not reacting with the electrodes. By reason for adding a supporting electrolyte is to achieve ionic conductivity. A background run is performed to determine the potential range before the experiment in the presence of bare WE, CE, RE, supporting electrolyte, and solvent.

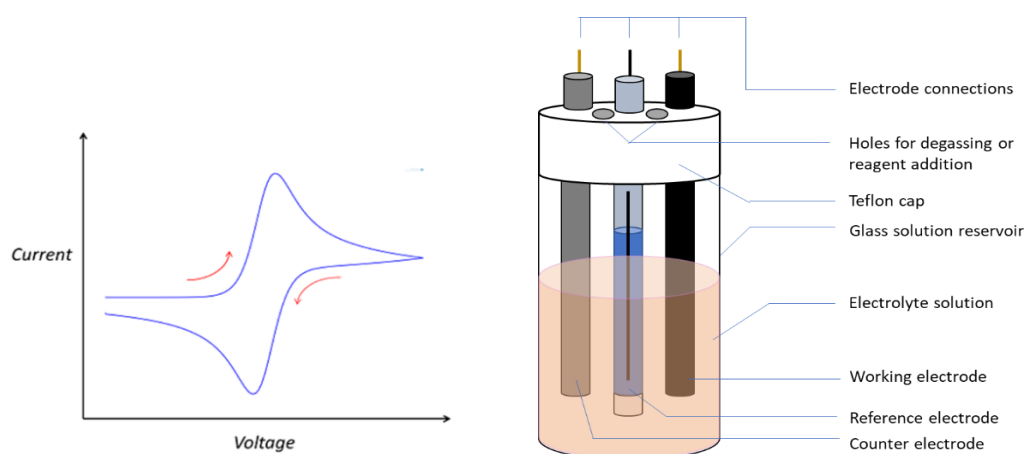


Figure 29 (a) Voltammogram for CPs (b) Experimental setup for CV study

2.3.4 Spectroelectrochemical Studies

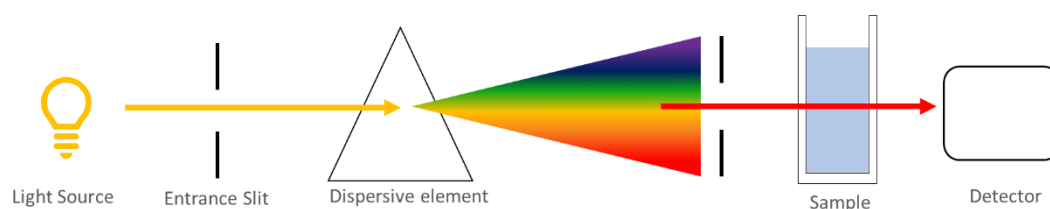


Figure 30 Experimental setup for optical study

The energy levels in organic molecules correspond to the electronic state energy levels under the UV-Vis radiation. The energy is absorbed in conjugated polymers and transported by electromagnetic radiation at resonance, where the migration of an electron from Under UV-Visible radiation, the energy is corresponded by the electronic state energy levels in organic molecules. Absorption of energy in the molecule occurs, and this energy is carried by electromagnetic radiation at resonance where an electron moves to higher molecular orbital from lower energy molecular orbital [109]. At this point, absorption profiles of the polymers in visible and NIR regions was determined by using Ultraviolet-Visible (UV-Vis) spectrophotometer. In clarifying the structure of examined molecules in solid, liquid, and or gaseous form, spectroscopic techniques constantly complement one another. For the measurement of thin film spectra, polymer solution was spray coated onto the ITO surface. For the solution spectra, polymers were dissolved in chloroform. From the obtained spectra, λ_{\max} and optical band gap (E_g^{op}) of the corresponding polymers can be calculated.

2.3.5 Photovoltaic Studies

An organic cell is constructed by following several steps, as illustrated in Figure 31. First, ITO coated glass substrate is cleaned by distilled water, detergent (Hellmanex), acetone, isopropyl alcohol to remove impurities. The cleaned glass substrate is dried using N_2 , then exposed to the oxygen plasma for 5 minutes using Harrick Plasma Cleaner. PEDOT: PSS is spin-coated on the ITO surface at 3500 rpm for 45 seconds. Substrates are annealed on the heater at $145^\circ C$ for 15 minutes. Then, Polymer: PC₇₁BM mixture is spin-coated on the device at 750 rpm in the glove box.

Later, devices are placed in the shadow mask and, LiF and Al layers are evaporated under the 5.0×10^{-7} mbar pressure. After the metal evaporation process, the active area of the devices is measured. Finally, current density vs. voltage characterization of the devices are performed by using Keithley 2400 source meter under illumination of AM 1.5G solar simulator (100 mV/cm^2).

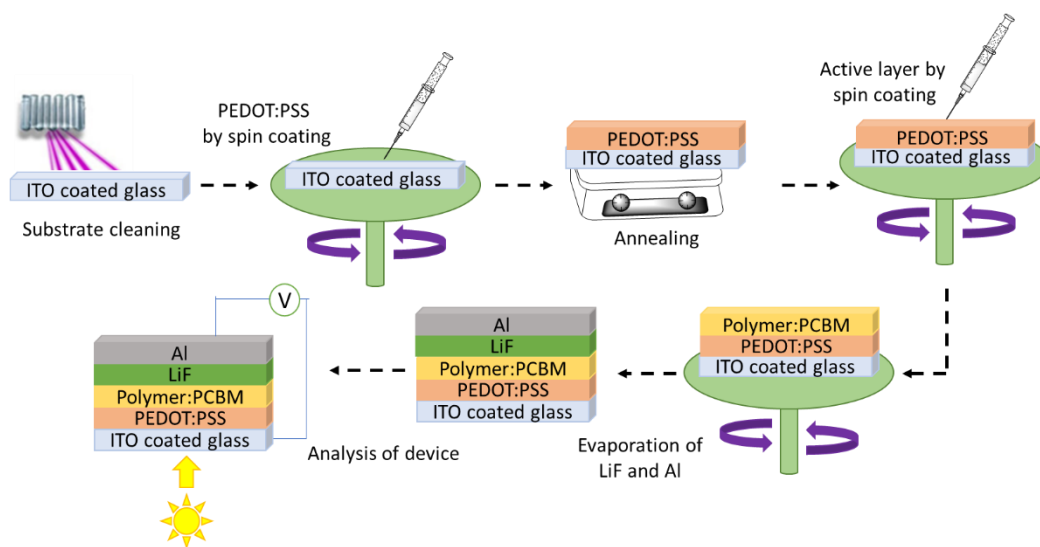


Figure 31 Device construction of BHJ OSCs.

CHAPTER 3

RESULTS AND DISCUSSION

3.1 Electrochemical Studies

Electrochemical studies of the polymers were performed via cyclic voltammetry (CV). Experiments were carried out by a three-electrode system as explained in section 5.3.3 to determine both redox behaviors HOMO-LUMO energy levels of the polymers. Synthesized polymers were dissolved in chloroform (5 mg/mL) and then sprayed coated onto the ITO electrodes with a spray gun. Polymer-coated ITO as working electrode, Pt wire as a counter electrode, and Ag wire as reference electrode were inserted in a cell, containing a mixture of 0.1 M tetrabutylammonium hexafluorophosphate/aceto-nitrile (TBAPF₆/ACN) electrolyte /solvent couple. Cyclic voltammograms were monitored between the potential range -1.6 V-1.2 V for PT1, -1.6 V-1.6 V for PT2, and -1.6 V-1.1 V for PT3 at a scan rate of 100 mV/s as shown in Figure 32. All three polymers show ambipolar character. Polymers with ambipolar properties exhibit both p- and n-type doping tendencies, making them suitable for various PV applications [110]. As stated in Table 3, thieno[3,2-*b*]thiophene π -bridged PT3 showed a lower oxidation onset value (0.58 V) compared to PT2 (0.73 V) and PT1 (0.88 V). Inserting electron rich thieno[3,2-*b*]thiophene, and selenophene π -bridges on the polymer backbone improve the intramolecular charge transfer (ICT) and leads to perform doping/dedoping processes easily [111]. Since thieno[3,2-*b*]thiophene has a more rigid and fused molecular structure, it provides more π -electron delocalization and higher charge mobilities [112]. Selenophene π -bridged PT2 also has lower E_{ox}^{onset} value than PT1. This can be resulting from the electron-rich character and strong electron-donating ability of the selenophene unit [91].

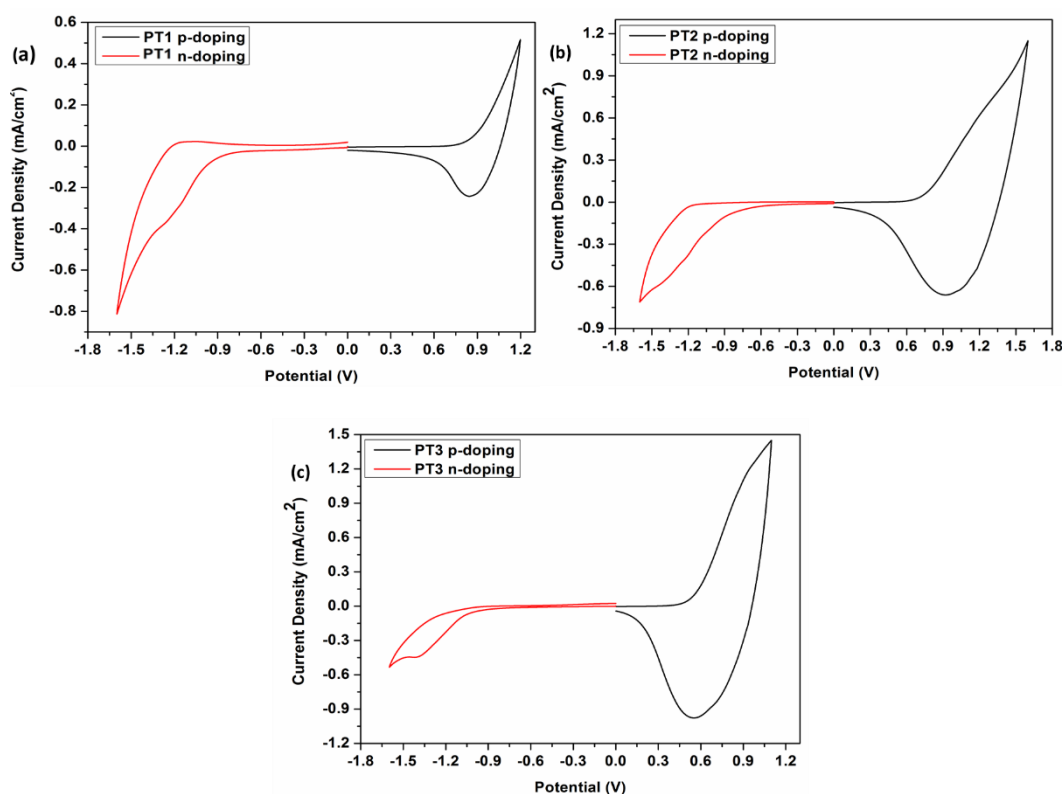


Figure 32 Cyclic voltammograms of a) PT1, b) PT2 and c) PT3 in 0.1 M TBAPF₆/ACN at 100 mV/s scan rate.

Determining the HOMO and LUMO energy levels is also crucial for OPV application. HOMO and LUMO energy levels of the polymers were calculated from the onset oxidation/reduction potentials according to the following equations (SHE vs. vacuum level accepted as 4.75 eV):

$$HOMO = -(4.75 + E_{ox}^{onset})$$

$$LUMO = -(4.75 + E_{red}^{onset})$$

HOMO and LUMO energy levels were calculated as -5.63/ -3.82 eV for PT1, -5.48/ -3.60 eV for PT2, and -5.33/ -3.75 eV for PT3 respectively (see in Table 3). According to the literature, the HOMO energy level of the polymer must be lower than the air oxidation threshold, which is -5.27 eV lower to synthesize a stable oxidative polymer. PT1, PT2, and PT3 are accepted to have stable oxidative polymers [113].

Table 3 Summary of electrochemical properties of PT1, PT2, and PT3.

	E_{ox}^{onset}	E_{red}^{onset}	HOMO	LUMO	E_g^{el}
Polymers	(V)	(V)	(eV)	(eV)	(eV)
PT1	0.88	-0.93	-5.63	-3.82	1.81
PT2	0.73	-0.85	-5.48	-3.90	1.58
PT3	0.58	-1.00	-5.33	-3.75	1.58

Optoelectronic characteristics vary dramatically depending on the changing donor units on the polymer backbone. Therefore, changes in the HOMO energy level may be related to changes in the electron densities of the polymer chains and electrical characters [114]. Thieno[3,2-*b*]thiophene and selenophene have more significant electron density because of their extended conjugation; thus, thieno[3,2-*b*]thiophene and selenophene containing PT2 and PT3 have the higher HOMO energy levels (-5.48 eV and -5.33 eV) than thiophene containing polymer. The stronger electron-donating ability of thieno[3,2-*b*]thiophene and selenophene are highlighted and demonstrated by the oxidation potential of the PT2 and PT3. To sum, polymers with selenophene, and thieno[3,2-*b*]thiophene π -bridges are easily oxidized than that thiophene analogs, while a greater decrease in reduction potential [115].

LUMO energy levels of the π -bridged polymers are close to each other. Therefore, this information suggests that the LUMO levels of the D- π bridge-A type polymers are unaffected by the insertion of π -bridges. The LUMO levels of the polymers are all within a reasonable range (-3.90 to -3.75 eV) and are much higher than that of PC₇₁BM (-3.91 eV) [116], implying that efficient charge transfer may occur in their respective devices [85].

3.2 Optical Studies

Optical experiments were carried out to investigate the effects of different π -bridge architectures on the optical properties of the benzothiadiazole (BT) and benzodithiophene (BDT) based polymers. The normalized UV-Visible spectra of the polymers in chloroform and thin film form are shown in Figure 33, and Table 4 summarizes absorption wavelengths (λ_{max}), absorption edge wavelengths ($\lambda_{\text{max}}^{\text{onset}}$), and the optical band gap (E_{g}^{op}) of the synthesized polymers. The absorption spectra of dilute chloroform solutions show two absorption bands for all three polymers: the first peak is around at 300-450 nm, which can be identified as localized π - π^* transitions related to donor unit, and the second one is around at 450-750 nm, which corresponds to intramolecular charge transfer (ICT) between the D and A parts. The various structures of the π -bridges in the polymer backbones are primarily responsible for the differences in absorption position and intensity.

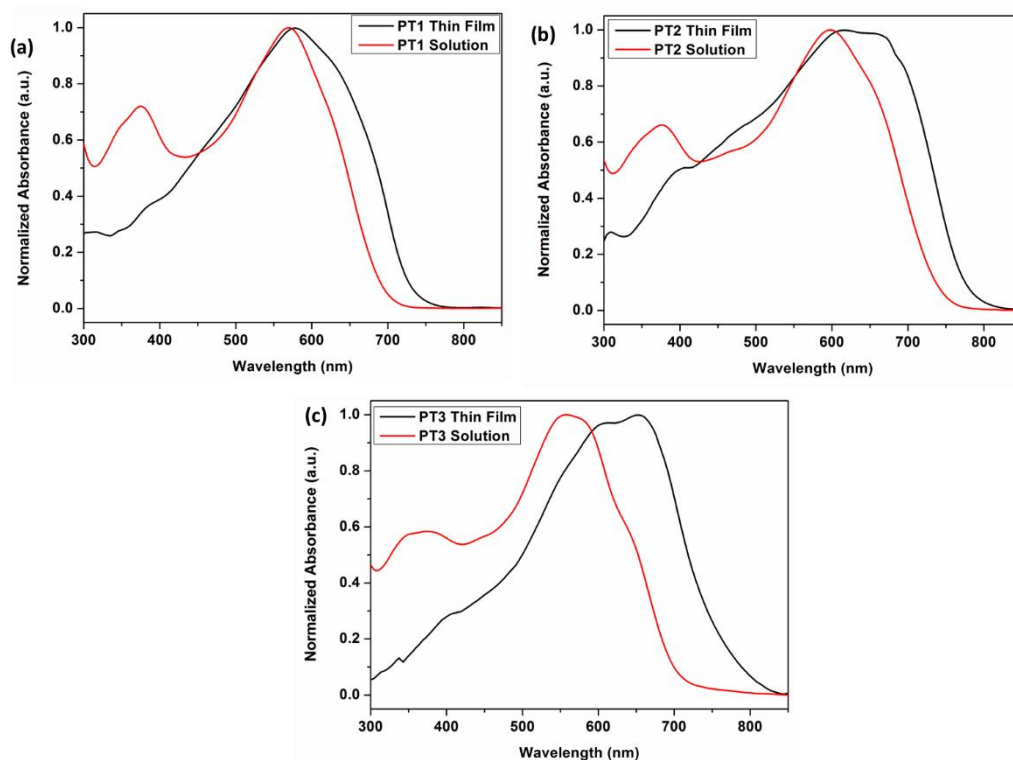


Figure 33 UV-Vis normalized absorption spectra of in CHCl_3 solution and thin-film for (a) PT1, (b) PT2, and (c) PT3.

The solid-state absorption spectra of the polymers are comparable to their solution spectra, with redshifts (ca. 10-96 nm) of their absorption maxima, confirming the presence of intermolecular polymer chain interaction and ordered structural organization of the polymers in the solid state. Furthermore, PT3 shows a vibronic shoulder at 606 nm, indicating that strong π - π stacking between the polymer backbones has resulted in an ordered structure in its solid films. Also, PT3 shows a significant redshift (96 nm) compared to PT1 and PT2.

Table 4 Summary of the optical properties of PT1, PT2, and PT3.

Polymer	λ_{\max} (nm) CHCl ₃	λ_{\max} (nm) thin film	$\lambda_{\max}^{\text{onset}}$ (nm)	E_g^{op} (eV)
PT1	570	580	730	1.70
PT2	597	616	785	1.58
PT3	557	653	770	1.61

From the absorption edge wavelengths ($\lambda_{\max}^{\text{onset}}$) data 730 nm, 785 nm, and 770 nm, respectively, optical band-gaps of the polymers are determined according to the following equation:

$$E = h \cdot \nu = \frac{h \cdot c}{\lambda} \quad \text{where Planck's constant} = 6.626 \times 10^{-34} \text{ J}\cdot\text{s}$$

$$\text{Speed of light} = 2.998 \times 10^8 \text{ m/s}$$

When all constants are converted to the electron volt (eV) unit, the equation transformed to the following equation:

$$E_g^{\text{op}} = \frac{1241}{\lambda}$$

Optical band gaps of the polymers were calculated as 1.70 eV for PT1, 1.58 eV for PT2, and 1.61 eV for PT3. Except for PT3, electronic bandgaps of the polymers are higher than optical bandgaps. While carrying out the CV experiments, the charge on the polymers can explain the difference between the optical and electrical bandgaps [114].

Thieno[3,2-*b*]thiophene bridged PT3 has absorption peaks at 373 and 557 nm in solution and 655 nm in the thin film, respectively, exhibiting a large redshift (98 nm) compared to the other polymers. Thiophene bridged PT1 has higher E_g^{op} (1.70 eV) than PT2 (1.58 eV) and PT3 (1.61 eV). This result can be achieved due to the inserting strong π -bridges into polymer backbones. Selenophene and thieno[3,2-*b*]thiophene have higher electron density compared to the thiophene analogs due to the extended conjugation length of the selenophene, thieno[3,2-*b*]thiophene units.

3.3 Photovoltaic Studies

This section compares the effect of thiophene, and selenophene bridged low band-gap D- π bridge-A copolymers used in BHJ OPVs. To investigate the impact of π -bridges on the photovoltaic characteristic of the polymers, bulk heterojunction OSC devices were constructed according to the conventional device structure of ITO/PEDOT/Polymer:PC₇₁BM/LiF/Al. The photovoltaic performance of the devices was evaluated under illumination of solar simulator (AM 1.5 G at 100 mW/cm²).

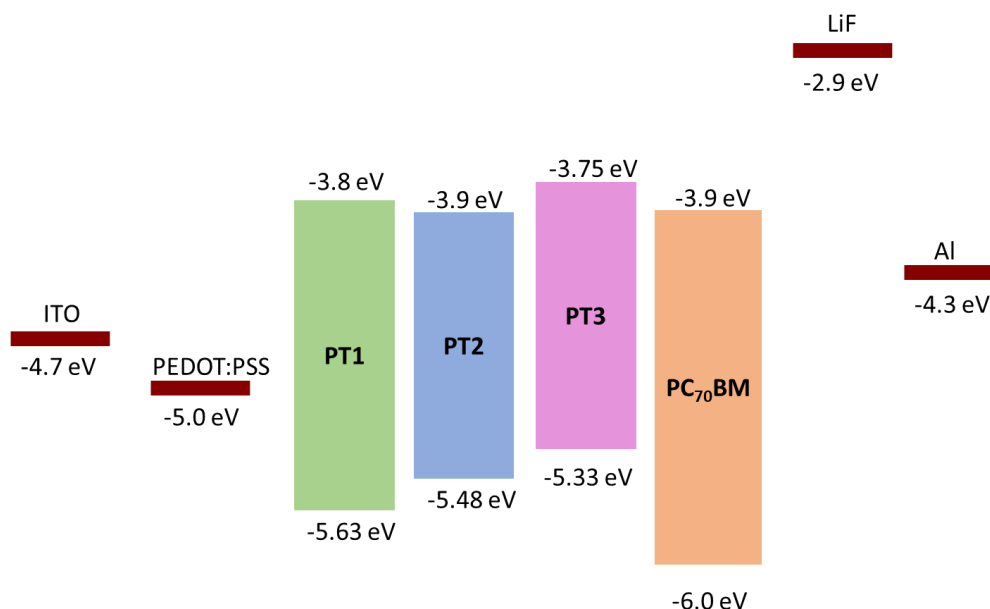


Figure 34 Energy level diagram of the PT1, PT2, and PT3

In figure 34, the energy level diagram for the PT1, PT2, and PT3 based OSCs with the conventional device architecture is illustrated. The energy levels of the corresponding polymers were determined via HOMO, LUMO and E_g^{el} measurements conducted in electrochemical studies, given in Section 3.1.

The detailed device fabrication and characterization methods were explained in Section 5.4.5. The active layer of BHJ OSC is made up of a blend of fullerene-based acceptor and polymer-based donor units. While PT1 and PT2 were used as donor units, PC₇₁BM was used as an acceptor unit in BHJ structure. In this study PC₇₁BM was used as n type material due to broader and stronger absorption than PC₆₁BM [117]. It was proven that both the blend ratio, organic solvent selection, and solvent additive processing directly impacted the surface morphology of the active layer, which is an important factor for the performance characteristics (J_{SC} , V_{OC} , FF) of the OSC devices [118,119]. Therefore, the blending ratio of the D-A bulk heterojunction layer was adjusted from 1:1, 1:2, and 1:3, and the mixture of Polymer: PC₇₁BM solutions were prepared using chlorobenzene (cb) and *o*-dcb (*o*-dichlorobenzene) organic solvents. In addition to these solvent additive optimizations were performed however solvent additive optimizations did not improve the photovoltaic performance of the devices. Summary of the photovoltaic properties and J-V curves of the PT1 and PT2 are illustrated in Table 5-6 and shown in Figure 35, respectively.

The thiophene π -bridged PT1 with the blend ratio PT1:PC₇₁BM (1:2, w:w) had the best device performance among the three polymers, with a PCE of 3.48%, a J_{SC} of 9.19 mA/cm², a V_{OC} of 0.75 V, and a FF of 50.30%. PT2:PC₇₁BM (1:2, w:w) based devices showed 3.48% PCE, with a J_{SC} of 8.58 mA/cm², a V_{OC} of 0.67 V, and a FF of 50.63%. Due to the limited solubility of the PT3, photovoltaic studies of the PT3:PC₇₁BM based devices can not be performed.

Table 5 Summary of the photovoltaic properties of PT1

PT1:PC₇₁BM (w:w)	V _{OC} (V)	J _{sc} (mA/cm ²)	FF (%)	PCE (%)	Solvent
1:2	0.73	6.48	49.44	2.34	<i>o</i> -dcb
1:2	0.75	9.19	50.30	3.48	cb
1:1	0.76	6.22	51.72	2.44	cb
1:3	0.76	8.09	50.75	3.12	cb
1:2	0.74	8.92	39.87	2.64	cb+1%DIO
1:2	0.74	9.40	39.40	2.74	cb+3%DPE

The photovoltaic properties of the PT1 are summarized in Table 5. Optimization studies were started with the selection of proper solvents. Chlorobenzene (Cb) was selected as the optimum solvent for PT1 based devices, same as its literature analogous [120,121]. After solvent selection, polymer PCBM ratio optimizations were carried out. As shown in Table 5, the blend ratio was changed from 1:1 to 1:3, and the 1:2 polymer: PC₇₁BM blend ratio demonstrated the highest power conversion efficiency (3.48%) with a maximum J_{SC} of 9.19 mA/cm². As depicted in Table 5, PT1:PC₇₁BM (1:2, w:w) blend ratio showed better photovoltaic performance than PT1:PC₇₁BM (1:3, w:w) blend ratio since an increase in the polymer concentration inside the active layer improves the light absorption capability of the active layer, resulting in enhanced photovoltaic performance. In addition to the blend ratio and solvent optimizations, solvent additive treatment was performed to improve the device performance. With the addition of a solvent additive, there was no improvement in device performance, and a sharp decrease was observed in FF values. This situation can be explained by morphological changes in the active layer, which will be discussed in Section 6.4. Consequently, the ideal polymer: PC₇₁BM blend ratio for the active layer was determined as 1:2 with J_{SC} of 9.19 mA/cm², V_{OC} of 0.75 V, FF of 50.30%, and PCE of 3.48%. For PT1, the current density-voltage graph (J-V) was shown in Figure 35-a.

Table 6 Summary of the photovoltaic properties of PT2

PT2:PC₇₁BM (w:w)	V _{oc} (V)	J _{sc} (mA/cm ²)	FF (%)	PCE (%)	Solvent
1:1	0.67	6.70	46.81	2.12	<i>o</i> -dcb
1:2	0.67	8.58	50.63	2.42	<i>o</i>-dcb
1:3	0.66	7.05	50.34	2.35	<i>o</i> -dcb
1:2	0.63	6.50	39.76	1.64	<i>o</i> -dcb +1%DIO
1:2	0.64	5.96	38.79	1.48	<i>o</i> -dcb +3%DPE

For PT2, polymer: PCBM ratio optimizations were carried out and 1:2 polymer: PCBM ratio found as optimum. As shown in Table 6, when the PT2:PC₇₁BM blend ratio altered from 1:2 to 1:3, the short circuit current (J_{sc}) value for PT2 based OSC decreased from 8.58 mA/cm² to 7.05 mA/cm². The reason behind this result might be the increased PC₇₁BM loading decreased polymer content of the blend. When the polymer content of the blend decreases, the ability of the active layer to absorb light decreases, resulting in reduced current values. Furthermore, the maximum fill factor (FF) of 50.63% was obtained for the 1:2 blend ratio (PT2:PC₇₁BM). The rise in PCE and FF can be attributed to the enhanced morphology of the active layer since the active layer morphology predominantly influences FF values.

Moreover, to improve the photovoltaic performance of the OSCs, different additive treatments were applied. However, additive treatment resulted in a drastic fall in the PCE due to decreased FF values. This indicates that additive treatment causes the active layer morphology to deform, which will be explored more in the morphological analysis of the active layers in section 6.4.

To sum, as a result of ratio and additive optimizations, the ideal polymer: PC₇₁BM blend ratio for PT2 containing the active layer was determined as 1:2 with J_{sc} of 8.85 mA/cm², V_{oc} of 0.67 V, FF of 50.63%, and PCE of 2.42%. For PT2, the photovoltaic parameters were illustrated in Table 6, and the current density-voltage graph (J-V) was shown in Figure 35-b.

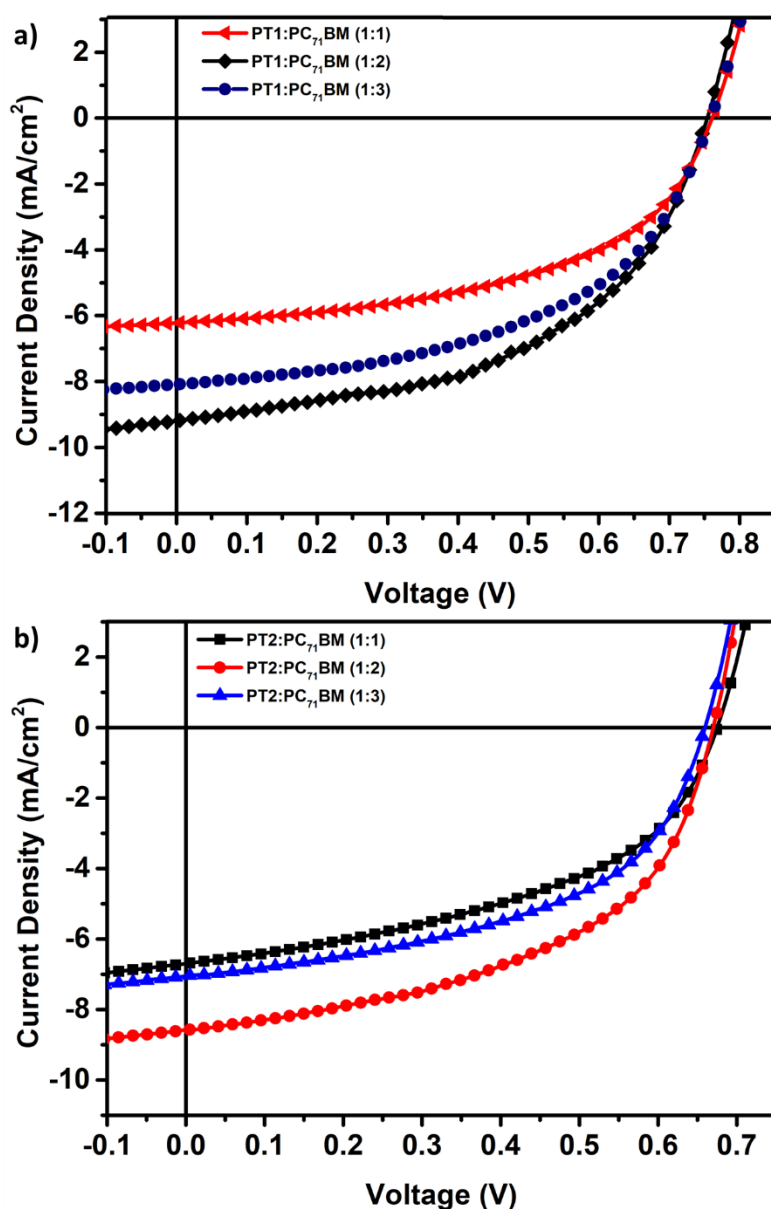


Figure 35 J-V characterization of a) PT1, and b) PT2

The external quantum efficiencies (EQE) of the devices were examined. For EQE analysis, photovoltaic devices were prepared following the same procedures with photovoltaic studies. EQE of the photovoltaic devices was recorded and represented in Figure 36. All devices have a light response between the 350-720 nm wavelength range, consistent with the red-shifted spectra of the polymers obtained from the optical analysis.

The J_{SC} values obtained from the J-V curves of the OSCs were confirmed by integrating the area under the EQE curve. Maximum EQE values for PT1 and PT2 based OSCs were found as 64% and 54%, respectively. As stated in Table 5 and Table 6, the J_{SC} values obtained from the J-V curves are consistent with the J_{SC} values obtained from the EQE curves.

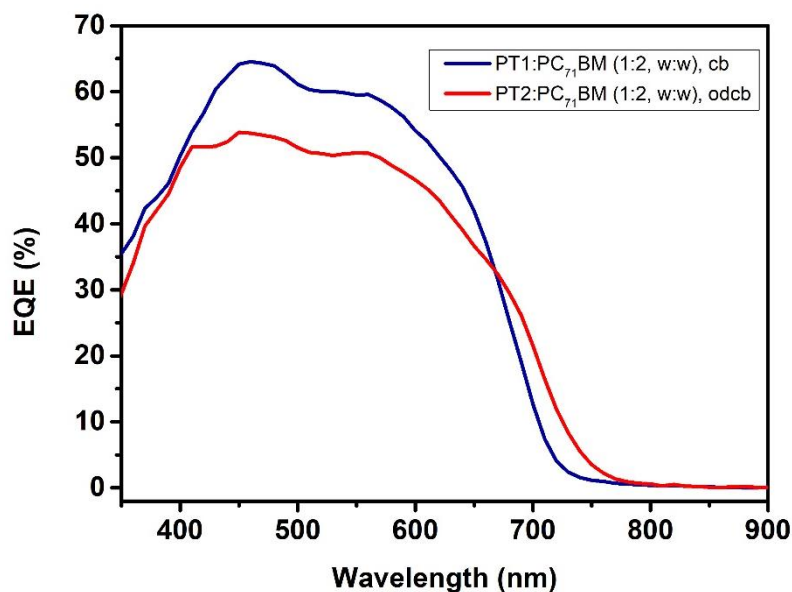


Figure 36 EQE curves of PT1 and PT2 based best-performed devices

3.4 Thermal Studies

Thermogravimetric analyses of the polymers were reported in Appendices Part B. TGA analysis was carried out using Perkin Elmer Pyris 1 instrument at a heating rate of 10 °C/minute in the range of 25 °C - 655°C in the inert atmosphere. TGA is an analytical technique that monitors the weight change that happens while the sample is heated at a constant rate to observe the thermal stability of the material and the fraction of the volatile components. Thermograms show the 5% weight loss of the polymers temperatures as 341 °C, 303 °C, 320 °C, respectively. If the polymers are heated up to 650 °C, 43.4 %, 46.4 %, and 39.5 % mass loss are observed. These results indicate that polymers have high-temperature stability.

3.5 Morphology

To achieve high fill factors and enhanced overall device performance, morphology control of the active layer is crucial for OSCs. The nanoscale phase separation mostly used for the determination of exciton dissociation, charge transport, and ultimately the photovoltaic performance [122,123]. A bi-continuous charge transport network is necessary to improve device performance because the size of the domains is required for excitons to reach the donor-acceptor interface, where the charge is generated [124]. Therefore, the topographies and morphologies of active layers were examined using atomic force microscopy (AFM) and transmission electron microscopy (TEM), respectively. (Figures 37-39)

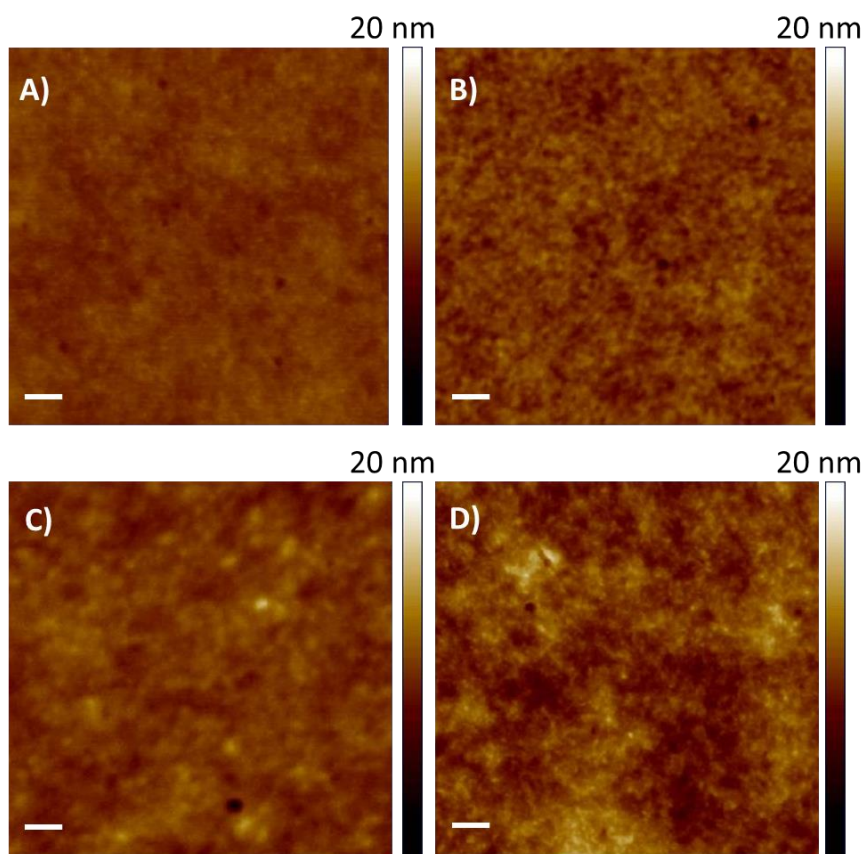


Figure 37 AFM images of A) PT1: PC₇₁BM (1:2, w/w), B) PT1: PC₇₁BM (1:2, w/w) with 3% DPE additive, C) PT2: PC₇₁BM (1:2, w/w), D) PT2: PC₇₁BM (1:2, w/w) with 3% DPE additive. Scale bar is 200 nm.

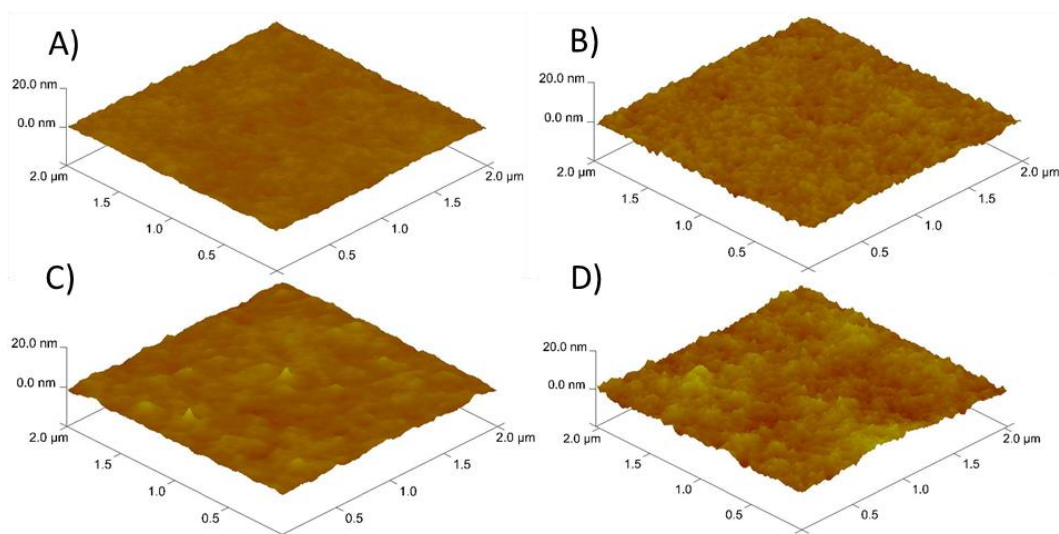


Figure 38 3D-AFM images of A) PT1: PC₇₁BM (1:2, w/w), B) PT1: PC₇₁BM (1:2, w/w)) with 3% DPE additive, C) PT2: PC₇₁BM (1:2, w/w), D) PT2: PC₇₁BM (1:2, w/w) with 3% DPE additive

Topographic images of the photoactive layer containing PT1:PC₇₁BM (1:2, w/w) and PT2:PC₇₁BM (1:2, w/w), and those of 3% DPE additive containing active layers were shown in Figure 37. The surface roughness (R_{ms}) of the active layers were determined as 0.53 nm, 0.86 nm for the blends of PT1:PC₇₁BM, and PT2:PC₇₁BM, on the other hand, 0.85 nm, and 1.14 nm for PT1:PC₇₁BM with 3% DPE, PT2:PC₇₁BM with 3% DPE, respectively. Active layer processed without any additive treatment had smoother surfaces. However, active layer processed with additive had higher roughness values, which may lead to defects in the active layer and dramatically decrease the fill factor values.

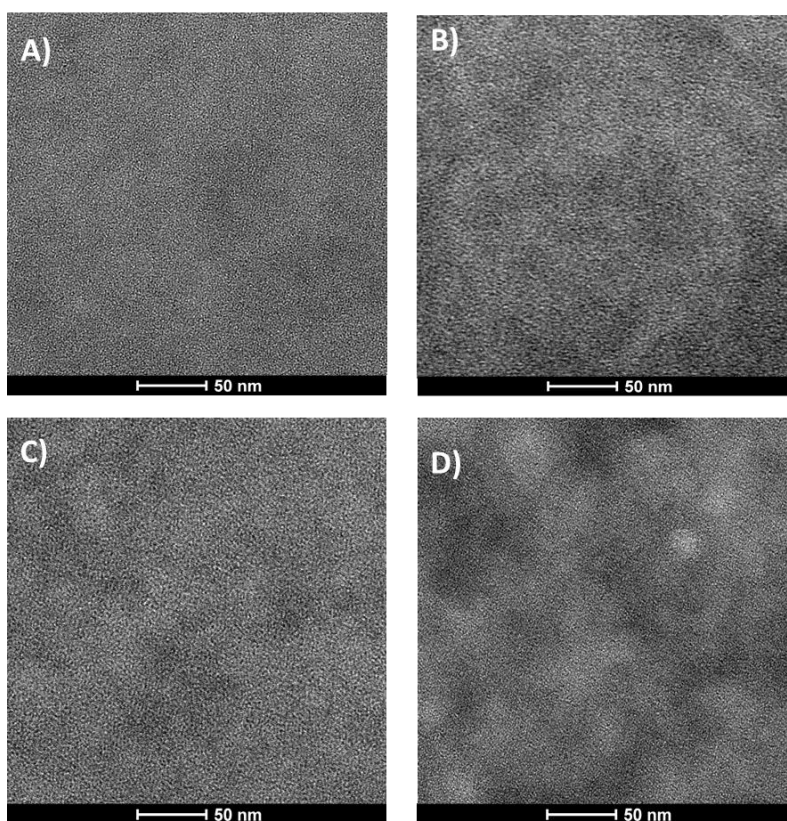


Figure 39 TEM images of best performed devices A) PT1: PC₇₁BM (1:2, w/w), B) PT1: PC₇₁BM (1:2, w/w) with DPE additive, C) PT2: PC₇₁BM (1:2, w/w), D) PT2: PC₇₁BM (1:2, w/w) with DPE additive.

TEM images also prove the morphological information about the polymer containing active layers, shown in Figure 38. While the photoactive layer containing PT1:PC₇₁BM (1:2, w/w) and PT2:PC₇₁BM (1:2, w/w) illustrate well mixed and homogeneous morphology, aggregations were observed for the 3% DPE containing active layers. These aggregations may negatively affect the charge transportation, therefore decrease in the FF values and the PCE of the devices.

CHAPTER 4

CONCLUSION

A series of Donor- π bridge-Acceptor copolymers were synthesized from 5,6-bis(octyloxy)benzo[c][1,2,5]thiadiazole and (4,8-bis(5-(2-ethylhexyl)thieno[3,2-*b*]thiophen-2-yl)benzo[1,2-*b*:4,5-*b'*]dithiophene-2,6-diyl)bis(trimethylstannane) via Pd catalyzed Stille cross-coupling reactions. Thiophene, selenophene, and thieno[3,2-*b*]thiophene π bridge incorporated polymers were named as PT1, PT2, and PT3, respectively. The effect of π bridges on the optical, electrochemical and photovoltaic properties were studied. Polymers showed red-shifted absorption maxima, especially PT3. E_g^{op} values were determined as 1.70 eV for PT1, 1.58 eV for PT2, and 1.61 eV for PT3. According to the electrochemical studies, all polymers showed ambipolar character. The HOMO/LUMO energy levels were calculated as -5.63/-3.82 eV, -5.48/-3.90 eV, and -5.33/-3.75 eV, for PT1, PT2, and PT3 respectively. E_g^{op} of the polymers are in good agreement with their electronic bandgaps. All polymers were thermally stable up to 300°C, which indicated that they were applicable in PV studies. Both PT1 and PT2 had good solubility in commonly used organic solvents. However, PT3 was soluble only in chlorobenzene. Due to high molecular weight of PT3, solubility problems were observed, and photovoltaic studies were not completed. The highest PCE of the PT1 and PT2 based OSCs were recorded as 3.48% and 2.42%, respectively. The formation of agglomerations and rough surfaces in the morphology resulting from additive treatment results in a decrease in PCE through a fall in FF, limiting the enhancement of the photovoltaic performance for both PT1 and PT2 based OSCs.

REFERENCES

- [1] BP, Statistical Review of World Energy, (2020) 66. <https://www.bp.com/content/dam/bp/business-sites/en/global/corporate/pdfs/energy-economics/statistical-review/bp-stats-review-2020-full-report.pdf>.
- [2] V. Smil, Energy Transitions: Global and National Perspectives, Second edi, Praeger, 2016. <http://vaclavsmil.com/2016/12/14/energy-transitions-global-and-national-perspectives-second-expanded-and-updated-edition>.
- [3] X. Li, Chapter One Thermodynamic Performance of Fuel Cells and Comparison with Heat Engines, Elsevier Ltd, 2007. [https://doi.org/10.1016/S1752-301X\(07\)80006-8](https://doi.org/10.1016/S1752-301X(07)80006-8).
- [4] A. Bahadori, C. Nwaoha, A review on solar energy utilisation in Australia, Renew. Sustain. Energy Rev. 18 (2013) 1–5. <https://doi.org/10.1016/j.rser.2012.10.003>.
- [5] J. Mohtasham, Review Article-Renewable Energies, Energy Procedia. 74 (2015) 1289–1297. <https://doi.org/10.1016/j.egypro.2015.07.774>.
- [6] T. Tsoutsos, N. Frantzeskaki, V. Gekas, Environmental impacts from the solar energy technologies, Energy Policy. 33 (2005) 289–296. [https://doi.org/10.1016/S0301-4215\(03\)00241-6](https://doi.org/10.1016/S0301-4215(03)00241-6).
- [7] R. Saidur, M.R. Islam, N.A. Rahim, K.H. Solangi, A review on global wind energy policy, Renew. Sustain. Energy Rev. 14 (2010) 1744–1762. <https://doi.org/10.1016/j.rser.2010.03.007>.
- [8] A. Shahsavari, M. Akbari, Potential of solar energy in developing countries for reducing energy-related emissions, Renew. Sustain. Energy Rev. 90 (2018) 275–291. <https://doi.org/10.1016/j.rser.2018.03.065>.

- [9] Q. Wang, H.N. Qiu, Situation and outlook of solar energy utilization in Tibet, China, *Renew. Sustain. Energy Rev.* 13 (2009) 2181–2186. <https://doi.org/10.1016/j.rser.2009.03.011>.
- [10] K. Bilen, O. Ozyurt, K. Bakirci, S. Karsli, S. Erdogan, M. Yilmaz, O. Comakli, Energy production, consumption, and environmental pollution for sustainable development: A case study in Turkey, *Renew. Sustain. Energy Rev.* 12 (2008) 1529–1561. <https://doi.org/10.1016/j.rser.2007.03.003>.
- [11] A.J. Heeger, 25th anniversary article: Bulk heterojunction solar cells: Understanding the mechanism of operation, *Adv. Mater.* 26 (2014) 10–28. <https://doi.org/10.1002/adma.201304373>.
- [12] F. Bayrak, N. Abu-Hamdeh, K.A. Alnefaie, H.F. Öztop, A review on exergy analysis of solar electricity production, *Renew. Sustain. Energy Rev.* 74 (2017) 755–770. <https://doi.org/10.1016/j.rser.2017.03.012>.
- [13] T. Saga, Advances in crystalline silicon solar cell technology for industrial mass production, *NPG Asia Mater.* 2 (2010) 96–102. <https://doi.org/10.1038/asiamat.2010.82>.
- [14] I. Fraunhofer Institute for Solar Energy Systems, Photovoltaics Report, (2021). www.ise.fraunhofer.de.
- [15] R.M. Izatt, S.R. Izatt, R.L. Bruening, N.E. Izatt, B.A. Moyer, Challenges to achievement of metal sustainability in our high-tech society, *Chem. Soc. Rev.* 43 (2014) 2451–2475. <https://doi.org/10.1039/c3cs60440c>.
- [16] P.P. Altermatt, Silicon solar cells, The Royal Society of Chemistry, 2005. https://doi.org/10.1007/0-387-27256-9_11.
- [17] M.A. Green, High Efficiency Silicon Solar Cells, Goetzberger A., Palz W., Willeke G. Seventh E.C. Photovolt. Sol. Energy Conf. Springer, Dordr. (1987) 681–687. https://doi.org/10.1007/978-94-009-3817-5_121.

- [18] J.F. Geisz, R.M. France, K.L. Schulte, M.A. Steiner, A.G. Norman, H.L. Guthrey, M.R. Young, T. Song, T. Moriarty, Six-junction III–V solar cells with 47.1% conversion efficiency under 143 Suns concentration, *Nat. Energy*. 5 (2020) 326–335. <https://doi.org/10.1038/s41560-020-0598-5>.
- [19] NREL, Best Research-Cell Efficiency Chart, 2021. <https://www.nrel.gov/pv/cell-efficiency.html>.
- [20] A. Mohammad Bagher, Comparison of Organic Solar Cells and Inorganic Solar Cells, *Int. J. Renew. Sustain. Energy*. 3 (2014) 53. <https://doi.org/10.11648/j.ijrse.20140303.12>.
- [21] L. Duan, N.K. Elumalai, Y. Zhang, A. Uddin, Progress in non-fullerene acceptor based organic solar cells, *Sol. Energy Mater. Sol. Cells*. 193 (2019) 22–65. <https://doi.org/10.1016/j.solmat.2018.12.033>.
- [22] L. Duan, H. Yi, Z. Wang, Y. Zhang, F. Haque, B. Sang, R. Deng, A. Uddin, Semitransparent organic solar cells based on PffBT4T-2OD with a thick active layer and near neutral colour perception for window applications, *Sustain. Energy Fuels*. 3 (2019) 2456–2463. <https://doi.org/10.1039/c9se00413k>.
- [23] C. Yan, S. Barlow, Z. Wang, H. Yan, A.K.Y. Jen, S.R. Marder, X. Zhan, Non-fullerene acceptors for organic solar cells, *Nat. Rev. Mater.* 3 (2018) 1–19. <https://doi.org/10.1038/natrevmats.2018.3>.
- [24] A. Wadsworth, M. Moser, A. Marks, M.S. Little, N. Gasparini, C.J. Brabec, D. Baran, I. McCulloch, Critical review of the molecular design progress in non-fullerene electron acceptors towards commercially viable organic solar cells, *Chem.Soc.Rev.* 48(2019)1596–1625. doi.org/10.1039/c7cs00892a.
- [25] K.K. Sadasivuni, K. Deshmukh, T.N. Ahipa, A. Muzaffar, M.B. Ahamed, S.K.K. Pasha, M.A.A. Al-Maadeed, Flexible, biodegradable and recyclable solar cells: a review, *J. Mater. Sci. Mater. Electron*. 30 (2019) 951–974. <https://doi.org/10.1007/s10854-018-0397-y>.

- [26] J. Bergqvist, T. Österberg, A. Melianas, L. Ever Aguirre, Z. Tang, W. Cai, Z. Ma, M. Kemerink, D. Gedefaw, M.R. Andersson, O. Inganäs, Asymmetric photocurrent extraction in semitransparent laminated flexible organic solar cells, *Npj Flex. Electron.* 2 (2018). <https://doi.org/10.1038/s41528-01700176>.
- [27] M. Kaltenbrunner, M.S. White, E.D. Głowacki, T. Sekitani, T. Someya, N.S. Sariciftci, S. Bauer, Ultrathin and lightweight organic solar cells with high flexibility, *Nat. Commun.* 3 (2012). <https://doi.org/10.1038/ncomms1772>.
- [28] C. Winder, N.S. Sariciftci, Low bandgap polymers for photon harvesting in bulk heterojunction solar cells, *J. Mater. Chem.* 14 (2004) 1077–1086. <https://doi.org/10.1039/b306630d>.
- [29] O. Inganäs, Organic Photovoltaics over Three Decades, *Adv. Mater.* 30 (2018) 1–26. <https://doi.org/10.1002/adma.201800388>.
- [30] J. Hou, O. Inganäs, R.H. Friend, F. Gao, Organic solar cells based on non-fullerene acceptors, *Nat. Mater.* 17 (2018) 119–128. doi:10.1038/NMAT5063.
- [31] W. Hresko, Feature Article, *Remedial Spec. Educ.* 10 (1989) 8. <https://doi.org/10.1177/074193258901000304>.
- [32] S. Günes, H. Neugebauer, N.S. Sariciftci, Conjugated polymer-based organic solar cells, *Chem. Rev.* 107 (2007) 1324–1338. DOI: 10.1021/cr050149z.
- [33] S. Rafique, S.M. Abdullah, K. Sulaiman, M. Iwamoto, Fundamentals of bulk heterojunction organic solar cells: An overview of stability/degradation issues and strategies for improvement, *Renew. Sustain. Energy Rev.* 84 (2018) 43–53. <https://doi.org/10.1016/j.rser.2017.12.008>.
- [34] C. Dyer-Smith, J. Nelson, *Organic Solar Cells*, Elsevier Ltd, 2012. <https://doi.org/10.1016/B978-0-12-385934-1.00016-7>.
- [35] P.W.M. Blom, V.D. Mihailetschi, L.J.A. Koster, D.E. Markov, Device physics of polymer:Fullerene bulk heterojunction solar cells, *Adv. Mater.* 19 (2007) 1551–1566. <https://doi.org/10.1002/adma.200601093>.

- [36] C.J. Brabec, C. Winder, N.S. Sariciftci, J.C. Hummelen, A. Dhanabalan, P.A. Van Hal, R.A.J. Janssen, A low-bandgap semiconducting polymer for photovoltaic devices and infrared emitting diodes, *Adv. Funct. Mater.* 12 (2002) 709–712. [https://doi.org/10.1002/1616-3028\(20021016\)12:10<709::AID-ADFM709>3.0.CO;2-N](https://doi.org/10.1002/1616-3028(20021016)12:10<709::AID-ADFM709>3.0.CO;2-N).
- [37] N. Yeh, P. Yeh, Organic solar cells: Their developments and potentials, *Renew. Sustain. Energy Rev.* 21 (2013) 421–431. <https://doi.org/10.1016/j.rser.2012.12.046>.
- [38] A.C. Mayer, S.R. Scully, B.E. Hardin, M.W. Rowell, M.D. McGehee, Polymer-based solar cells, *Mater. Today.* 10 (2007) 28–33. [https://doi.org/10.1016/S1369-7021\(07\)70276-6](https://doi.org/10.1016/S1369-7021(07)70276-6).
- [39] M.C. Scharber, N.S. Sariciftci, Efficiency of bulk-heterojunction organic solar cells, *Prog. Polym. Sci.* 38 (2013) 1929–1940. <https://doi.org/10.1016/j.progpolymsci.2013.05.001>.
- [40] C. Deibe, T. Strobe, V. Dyakonov, Role of the charge transfer state in organic donor-acceptor solar cells, *Adv. Mater.* 22 (2010) 4097–4111. <https://doi.org/10.1002/adma.201000376>.
- [41] S.D. Baranovskii, H. Cordes, F. Hensel, G. Leising, Charge-carrier transport in disordered organic solids, *Phys. Rev. B - Condens. Matter Mater. Phys.* 62 (2000) 7934–7938. <https://doi.org/10.1103/PhysRevB.62.7934>.
- [42] Y. Zhou, M. Eck, M. Krüger, Bulk-heterojunction hybrid solar cells based on colloidal nanocrystals and conjugated polymers, *Energy Environ. Sci.* 3 (2010) 1851–1864. <https://doi.org/10.1039/c0ee00143k>.
- [43] H. Machrafi, *Green Energy and Technology*, 2012. <https://doi.org/10.2174/97816080528511120101>.

- [44] M.M. Mandoc, L.J.A. Koster, P.W.M. Blom, Optimum charge carrier mobility in organic solar cells, *Appl. Phys. Lett.* 90 (2007) 8–11. <https://doi.org/10.1063/1.2711534>.
- [45] M. Lenes, L.J.A. Koster, V.D. Mihailetschi, P.W.M. Blom, Thickness dependence of the efficiency of polymer:fullerene bulk heterojunction solar cells, *Appl. Phys. Lett.* 88 (2006) 86–89. <https://doi.org/10.1063/1.2211189>.
- [46] S.R. Cowan, N. Banerji, W.L. Leong, A.J. Heeger, Charge formation, recombination, and sweep-out dynamics in organic solar cells, *Adv. Funct. Mater.* 22 (2012) 1116–1128. <https://doi.org/10.1002/adfm.201101632>.
- [47] N. Marinova, S. Valero, J.L. Delgado, Organic and perovskite solar cells: Working principles, materials and interfaces, *J. Colloid Interface Sci.* 488 (2017) 373–389. <https://doi.org/10.1016/j.jcis.2016.11.021>.
- [48] S. Rafique, S.M. Abdullah, K. Sulaiman, M. Iwamoto, Fundamentals of bulk heterojunction organic solar cells: An overview of stability/degradation issues and strategies for improvement, *Renew. Sustain. Energy Rev.* 84 (2018) 43–53. <https://doi.org/10.1016/j.rser.2017.12.008>.
- [49] F.C. Krebs, Fabrication and processing of polymer solar cells: A review of printing and coating techniques, *Sol. Energy Mater. Sol. Cells.* 93 (2009) 394–412. <https://doi.org/10.1016/j.solmat.2008.10.004>.
- [50] M. Brumbach, P.A. Veneman, F.S. Matrikar, T. Schulmeyer, A. Simmonds, W. Xia, P. Lee, N.R. Armstrong, Surface composition and electrical and electrochemical properties of freshly deposited and acid-etched indium tin oxide electrodes, *Langmuir.* 23 (2007) 11089–11099. <https://doi.org/10.1021/la701754u>.
- [51] A. Singh, M. Katiyar, A. Garg, Understanding the formation of PEDOT:PSS films by ink-jet printing for organic solar cell applications, *RSC Adv.* 5 (2015) 78677–78685. <https://doi.org/10.1039/c5ra11032g>.

- [52] E.D. Głowacki, K.L. Marshall, C.W. Tang, N.S. Sariciftci, Doping of organic semiconductors induced by lithium fluoride/aluminum electrodes studied by electron spin resonance and infrared reflection-absorption spectroscopy, *Appl. Phys. Lett.* 99 (2011) 1–4. <https://doi.org/10.1063/1.3615799>.
- [53] S.R. Cowan, A. Roy, A.J. Heeger, Recombination in polymer-fullerene bulk heterojunction solar cells, *Phys. Rev. B - Condens. Matter Mater. Phys.* 82 (2010) 1–10. <https://doi.org/10.1103/PhysRevB.82.245207>.
- [54] M.C. Scharber, D. Mühlbacher, M. Koppe, P. Denk, C. Waldauf, A.J. Heeger, C.J. Brabec, Design rules for donors in bulk-heterojunction solar cells - Towards 10 % energy-conversion efficiency, *Adv. Mater.* 18 (2006) 789–794. <https://doi.org/10.1002/adma.200501717>.
- [55] B. Kippelen, J.L. Brédas, Organic photovoltaics, *Energy Environ. Sci.* 2 (2009) 251–261. <https://doi.org/10.1039/b812502n>.
- [56] C.B. Nielsen, S. Holliday, H.Y. Chen, S.J. Cryer, I. McCulloch, Non-Fullerene Electron Acceptors for Use in Organic Solar Cells, *Acc. Chem. Res.* 48 (2015) 2803–2812. <https://doi.org/10.1021/acs.accounts.5b00199>.
- [57] C. Sae-Kung, B.F. Wright, T.M. Clarke, G.G. Wallace, A.J. Mozer, Effects of Interfacial Layers on the Open Circuit Voltage of Polymer/Fullerene Bulk Heterojunction Devices Studied by Charge Extraction Techniques, *ACS Appl. Mater. Interfaces.* 11 (2019) 21030–21041. <https://doi.org/10.1021/acsami.9b02850>.
- [58] H. Hoppe, N.S. Sariciftci, Organic solar cells: An overview, *J. Mater. Res.* 19 (2004) 1924–1945. <https://doi.org/10.1557/JMR.2004.0252>.
- [59] N.K. Elumalai, A. Uddin, Open circuit voltage of organic solar cells: An in-depth review, *Energy Environ. Sci.* 9 (2016) 391–410. <https://doi.org/10.1039/c5ee02871j>.

- [60] A.M. and J.-M. Nunzi, How to model the behaviour of organic photovoltaic cells, *Polym Int.* 55 (2006) 585–600. <https://doi.org/10.1002/pi.2038>.
- [61] H. Zhou, L. Yang, W. You, Rational design of high performance conjugated polymers for organic solar cells, *Macromolecules.* 45 (2012) 607–632. <https://doi.org/10.1021/ma201648t>.
- [62] X. Liu, C. Zhang, C. Duan, M. Li, Z. Hu, J. Wang, F. Liu, N. Li, C.J. Brabec, R.A.J. Janssen, G.C. Bazan, F. Huang, Y. Cao, Morphology Optimization via Side Chain Engineering Enables All-Polymer Solar Cells with Excellent Fill Factor and Stability, *J. Am. Chem. Soc.* 140 (2018) 8934–8943. <https://doi.org/10.1021/jacs.8b05038>.
- [63] W.A. Hammed, R. Yahya, A.L. Bola, H.N.M.E. Mahmud, Recent approaches to controlling the nanoscale morphology of polymer-based bulk-heterojunction solar cells, *Energies.* 6 (2013) 5847–5868. <https://doi.org/10.3390/en6115847>.
- [64] H. Shirakawa, E.J. Louis, A.G. MacDiarmid, C.K. Chiang, A.J. Heeger, Synthesis of electrically conducting organic polymers: Halogen derivatives of polyacetylene, (CH)_x, *J. Chem. Soc. Chem. Commun.* (1977) 578–580. <https://doi.org/10.1039/C39770000578>.
- [65] Y.J. Wang, G. Yu, Conjugated polymers: From synthesis, transport properties, to device applications, *J. Polym. Sci. Part B Polym. Phys.* 57 (2019) 1557–1558. <https://doi.org/10.1002/polb.24911>.
- [66] Y.J. Cheng, S.H. Yang, C.S. Hsu, Synthesis of conjugated polymers for organic solar cell applications, *Chem. Rev.* 109 (2009) 5868–5923. <https://doi.org/10.1021/cr900182s>.
- [67] A. Facchetti, π -Conjugated polymers for organic electronics and photovoltaic cell applications, *Chem. Mater.* 23 (2011) 733–758. <https://doi.org/10.1021/cm102419z>.

- [68] C.A. Junwu, C. Yong, Development of novel conjugated donor polymers for high-efficiency bulk-heterojunction photovoltaic devices, *Acc. Chem. Res.* 42 (2009) 1709–1718. <https://doi.org/10.1021/ar900061z>.
- [69] D. Xia, Y. Wu, Q. Wang, A. Zhang, C. Li, Y. Lin, F.J.M. Colberts, J.J. Van Franeker, R.A.J. Janssen, X. Zhan, W. Hu, Z. Tang, W. Ma, W. Li, Effect of Alkyl Side Chains of Conjugated Polymer Donors on the Device Performance of Non-Fullerene Solar Cells, *Macromolecules.* 49 (2016) 6445–6454. <https://doi.org/10.1021/acs.macromol.6b01326>.
- [70] I.O. Raji, S. Wen, Y. Li, D. Huang, X. Shi, A. Sapparbaev, C. Gu, C. Yang, X. Bao, Benzo bis (Thiazole)-Based Conjugated Polymer with Varying Alkylthio Side-Chain Positions for Efficient Fullerene-Free Organic Solar Cells, *ACS Appl. Mater. Interfaces.* (2021). <https://doi.org/10.1021/acsami.1c07822>.
- [71] C. Cui, W.Y. Wong, Y. Li, Improvement of open-circuit voltage and photovoltaic properties of 2D-conjugated polymers by alkylthio substitution, *Energy Environ. Sci.* 7 (2014) 2276–2284. <https://doi.org/10.1039/c4ee00446a>.
- [72] H. Yao, H. Zhang, L. Ye, W. Zhao, S. Zhang, J. Hou, Dialkylthio Substitution: An Effective Method to Modulate the Molecular Energy Levels of 2D-BDT Photovoltaic Polymers, *ACS Appl. Mater. Interfaces.* 8 (2016) 3575–3583. <https://doi.org/10.1021/acsami.5b07311>.
- [73] F. Wudl, N. Kobayashi, A.J. Heeger, Poly(isothianaphthene), *J. Org. Chem.* 49 (1984) 3382–3384.
- [74] Z.H. Zhou, T. Maruyama, T. Kanbara, T. Ikeda, K. Ichimura, T. Yamamoto, K. Tokuda, Unique optical and electrochemical properties of π -conjugated electrically conducting copolymers consisting of electron-withdrawing pyridine units and electron-donating thiophene units, *J. Chem. Soc. Chem. Commun.* 1460 (1991) 1210–1212. <https://doi.org/10.1039/C39910001210>.

- [75] E.E. Havinga, W. ten Hoeve, H. Wynberg, Alternate donor-acceptor small-band-gap semiconducting polymers; Polysquaraines and polycroconaines, *Synth. Met.* 55 (1993) 299–306. [https://doi.org/10.1016/0379-6779\(93\)90949-W](https://doi.org/10.1016/0379-6779(93)90949-W).
- [76] J.M. Jiang, M.C. Yuan, K. Dinakaran, A. Hariharan, K.H. Wei, Crystalline donor-acceptor conjugated polymers for bulk heterojunction photovoltaics, *J. Mater. Chem. A* 1 (2013) 4415–4422. <https://doi.org/10.1039/c2ta00965j>.
- [77] R.A. Segalman, B. McCulloch, S. Kirmayer, J.J. Urban, Block copolymers for organic optoelectronics, *Macromolecules* 42 (2009) 9205–9216. <https://doi.org/10.1021/ma901350w>.
- [78] S.B. Darling, Block copolymers for photovoltaics, *Energy Environ. Sci.* 2 (2009) 1266–1273. <https://doi.org/10.1039/b912086f>.
- [79] S.C. Lan, P.A. Yang, M.J. Zhu, C.M. Yu, J.M. Jiang, K.H. Wei, Thiophene spacers impart crystallinity and enhance the efficiency of benzotrithiophene-based conjugated polymers for bulk heterojunction photovoltaics, *Polym. Chem.* 4 (2013) 1132–1140. <https://doi.org/10.1039/c2py20819a>.
- [80] J. Peet, J.Y. Kim, N.E. Coates, W.L. Ma, D. Moses, A.J. Heeger, G.C. Bazan, Efficiency enhancement in low-bandgap polymer solar cells by processing with alkane dithiols, *Nat. Mater.* 6 (2007) 497–500. <https://doi.org/10.1038/nmat1928>.
- [81] H.Y. Chen, J. Hou, A.E. Hayden, H. Yang, K.N. Houk, Y. Yang, Silicon atom substitution enhances interchain packing in a thiophene-based polymer system, *Adv. Mater.* 22(2010)371–375. DOI: 10.1002/adma.200902469.
- [82] W. Chen, T. Xu, F. He, W. Wang, C. Wang, J. Strzalka, Y. Liu, J. Wen, D.J. Miller, J. Chen, K. Hong, L. Yu, S.B. Darling, Hierarchical nanomorphologies promote exciton dissociation in polymer/fullerene bulk heterojunction solar cells, *Nano Lett.* 11 (2011) 3707–3713. <https://doi.org/10.1021/nl201715q>.

- [83] T.H. Lee, M.H. Choi, S.J. Jeon, D.K. Moon, Correlation of intermolecular packing distance and crystallinity of D-A polymers according to π -spacer for polymer solar cells, *Polymer*. 99 (2016) 756–766. <https://doi.org/10.1016/j.polymer.2016.07.082>.
- [84] Shafiq UrRehman, A. Alam, S. Bibi, S. Sadaf, S.R. Khan, M. Shoaib, A.Q. Khan, M. Khan, W. UrRehman, The effect of different aromatic conjugated bridges on optoelectronic properties of diketopyrrolopyrrole-based donor materials for organic photovoltaics, *J. Mol. Model.* 26 (2020). <https://doi.org/10.1007/s00894-020-4341-8>.
- [85] X. Wang, Y. Sun, S. Chen, X. Guo, M. Zhang, X. Li, Y. Li, H. Wang, Effects of π -conjugated bridges on photovoltaic properties of donor- π -acceptor conjugated copolymers, *Macromolecules*. 45 (2012) 1208–1216. <https://doi.org/10.1021/ma202656b>.
- [86] S.C. Cevher, N.A. Unlu, A.C. Ozelcaglayan, D.H. Apaydin, Y.A. Udum, L. Toppare, A. Cirpan, Fused structures in the polymer backbone to investigate the photovoltaic and electrochromic properties of donor-acceptor-type conjugated polymers, *J. Polym. Sci. Part A Polym. Chem.* 51 (2013) 1933–1941. <https://doi.org/10.1002/pola.26553>.
- [87] J.H. Kim, H.S. Kim, J.B. Park, I.N. Kang, D.H. Hwang, Thieno[3,2-b]thiophene-substituted benzodithiophene in donor-acceptor type semiconducting copolymers: A feasible approach to improve performances of organic photovoltaic cells, *J. Polym. Sci. Part A Polym. Chem.* 52 (2014) 3608–3616. <https://doi.org/10.1002/pola.27431>.
- [88] K. Yilgram, M. Zupan, R. Skiles, Bromination of 2,1,3-Benzothiadiazoles, *J. Heterocycl. Chem.* 7 (1970) 629–633.
- [89] H.A.M. Van Mullekom, J.A.J.M. Vekemans, E.W. Meijer, Alternating copolymer of pyrrole and 2,1,3-benzothiadiazole, *Chem. Commun.* (1996) 2163–2164. <https://doi.org/10.1039/cc9960002163>.

- [90] B.A.D. Neto, A.A.M. Lapis, E.N. Da Silva Júnior, J. Dupont, 2,1,3-benzothiadiazole and derivatives: Synthesis, properties, reactions, and applications in light technology of small molecules, *European J. Org. Chem.* (2013) 228–255. <https://doi.org/10.1002/ejoc.201201161>.
- [91] D. Keles, M.C. Erer, E. Bolayir, S.C. Cevher, G. Hizalan, L. Toppare, A. Cirpan, Conjugated polymers with benzothiadiazole and benzotriazole moieties for polymer solar cells, *Renew. Energy.* 139 (2019) 1184–1193. <https://doi.org/10.1016/j.renene.2019.03.018>.
- [92] T.C. Parker, D.G. Patel, K. Moudgil, S. Barlow, C. Risko, J.L. Brédas, J.R. Reynolds, S.R. Marder, Heteroannulated acceptors based on benzothiadiazole, *Mater. Horizons.* 2 (2015) 22–36. <https://doi.org/10.1039/c4mh00102h>.
- [93] G. Kossmehl, K.-H. Hatscher, G. Manecke, Uber Polyarylenalkenylene und Polyheteroarylenalkenylene, *Die Makromol. Chemie.* 176 (1975) 539–559.
- [94] G. Kossmehl, G.; Beimling, P.; Manecke, Synthesis of Benzo[1,2-b:4,5-b']dithiophene and its 4,s-Dimethoxy and 4,s-Dimethyl Derivatives, *Chem. Ber.* 3203 (1986) 3198–3203.
- [95] J. Hou, M.H. Park, S. Zhang, Y. Yao, L.M. Chen, J.H. Li, Yang, Bandgap and molecular energy level control of conjugated polymer photovoltaic materials based on benzo[1,2-b:4,5-b']dithiophene, *Macromolecules.* 41 (2008) 6012–6018. <https://doi.org/10.1021/ma800820r>.
- [96] B. Zheng, L. Huo, Y. Li, Benzodithiophenedione-based polymers: recent advances in organic photovoltaics, *NPG Asia Mater.* 12 (2020). <https://doi.org/10.1038/s41427-019-0163-5>.
- [97] X. Xu, G. Zhang, Y. Li, Q. Peng, The recent progress of wide bandgap donor polymers towards non-fullerene organic solar cells, *Chinese Chem. Lett.* 30 (2019) 809–825. <https://doi.org/10.1016/j.ccllet.2019.02.030>.

- [98] S.M. Lee, T. Kumari, B. Lee, Y. Cho, J. Lee, J. Oh, M. Jeong, S. Jung, C. Yang, Horizontal-, Vertical-, and Cross-Conjugated Small Molecules: Conjugated Pathway-Performance Correlations along Operation Mechanisms in Ternary Non-Fullerene Organic Solar Cells, *Small*. 16 (2020) 1–12. <https://doi.org/10.1002/sml.201905309>.
- [99] S.M. Bang, S. Kang, Y.S. Lee, B. Lim, H. Heo, J. Lee, Y. Lee, S.I. Na, A novel random terpolymer for high-efficiency bulk-heterojunction polymer solar cells, *RSC Adv.* 7 (2017) 1975–1980. <https://doi.org/10.1039/c6ra27518d>.
- [100] M. Hurhangee, Heteroatom and bridged-ring π -conjugated polymers and their use in organic electronics, *Imp. Coll. London*. (2016). <http://hdl.handle.net/10044/1/73366>.
- [101] L.C. Karabay, B. Karabay, M.S. Karakoy, A. Cihaner, Effect of furan, thiophene and selenophene donor groups on benzoselenadiazole based donor-acceptor-donor systems, *J. Electroanal. Chem.* 780 (2016) 84–89. <https://doi.org/10.1016/j.jelechem.2016.08.039>.
- [102] G. Zuo, Z. Li, M. Zhang, X. Guo, Y. Wu, S. Zhang, B. Peng, W. Wei, J. Hou, Influence of the backbone conformation of conjugated polymers on morphology and photovoltaic properties, *Polym. Chem.* 5 (2014) 1976–1981. <https://doi.org/10.1039/c3py01231j>.
- [103] H.Y. Chen, S.C. Yeh, C.T. Chen, C.T. Chen, Comparison of thiophene- and selenophene-bridged donor-acceptor low band-gap copolymers used in bulk-heterojunction organic photovoltaics, *J. Mater. Chem.* 22 (2012) 21549–21559. <https://doi.org/10.1039/c2jm33735e>.
- [104] S. Zhi, H. Lim, B.W.T. Neo, A.C.M. Cho, X. Wang, A.A. Yan, X. Tan, A.H. Sze, O. Chan, Electrochromic p -Conjugated Copolymers Derived from Azulene, Fluorene, and Dialkyloxybenzothiadiazole, *Aust. J. Chem.* 66 (2013) 1048–1056. <https://doi.org/10.1071/CH13147>.

- [105] J.M. Jiang, P.A. Yang, T.H. Hsieh, K.H. Wei, Crystalline low-band gap polymers comprising thiophene and 2,1,3-benzooxadiazole units for bulk heterojunction solar cells, *Macromolecules*. 44 (2011) 9155–9163. <https://doi.org/10.1021/ma201848z>.
- [106] F. Liu, H. Li, Y. Wu, C. Gu, H. Fu, Naphthalene diimide and benzothiadiazole copolymer acceptor for all-polymer solar cells with improved open-circuit voltage and morphology, *RSC Adv.* 5 (2015) 92151–92158. <https://doi.org/10.1039/c5ra14887a>.
- [107] A.S. Mukasyan, *DTA/TGA-Based Methods*, Elsevier Inc., 2017. <https://doi.org/10.1016/b978-0-12-804173-4.00040-5>.
- [108] V. Bush, *Instrumental Analysis*, Massachusetts Inst. Technol. (1936) 649–669.
- [109] G. Manivannan, UV-vis spectroscopy as an analytical tool for the characterization of polymers, *Mater. Charact. Opt. Probe Tech. A Crit. Rev.* 10291 (1997) 1029107. <https://doi.org/10.1117/12.279857>.
- [110] A. Opitz, M. Bronner, J. Wagner, M. Götzenbrugger, W. Brütting, Ambipolar organic semiconductor blends for photovoltaic cells, *Photonics Sol. Energy Syst. II*. 7002 (2008) 70020J. <https://doi.org/10.1117/12.780998>.
- [111] S. Goker, G. Hizalan, E. Aktas, S. Kutkan, A. Cirpan, L. Toppare, 2,1,3-Benzooxadiazole, thiophene and benzodithiophene based random copolymers for organic photovoltaics: thiophene versus thieno[3,2-b]thiophene as π -conjugated linkers, *New J. Chem.* 40 (2016) 10455–10464. <https://doi.org/10.1039/c6nj02469f>.
- [112] Z. Li, L. Huo, X. Guo, W. Yong, S. Zhang, H. Fan, Synthesis and photovoltaic properties of D- π -A copolymers based on thieno[3,2-b]thiophene bridge unit, *Polymer* . 54 (2013) 6150–6157. [10.1016/j.polymer.2013.09.021](https://doi.org/10.1016/j.polymer.2013.09.021).

- [113] M.H. Choi, H.Y. Kim, E.J. Lee, D. Kyung Moon, Control of molecular curvature and crystallinity of quinacridone-benzoxadiazole copolymers using different π bridge for polymer solar cells, *Polymer*. 91 (2016) 162–173. <https://doi.org/10.1016/j.polymer.2016.03.062>.
- [114] S. Goker, G. Hizalan, S.O. Hacioglu, L. Toppare, Investigation of Optical and Electrochemical Properties of Benzene Based Solution Processable 2,1,3-Benzoxadiazole Comprising Polymers, *J. Electrochem. Soc.* 167 (2020) 122505. <https://doi.org/10.1149/1945-7111/abab23>.
- [115] L. Fan, R. Cui, X. Guo, D. Qian, B. Qiu, J. Yuan, Y. Li, W. Huang, J. Yang, W. Liu, X. Xu, L. Li, Y. Zou, A new two-dimensional donor/acceptor copolymer based on 4,8-bis(2'-ethylhexylthiophene)thieno[2,3-f]benzofuran for high-performance polymer solar cells, *J. Mater. Chem. C*. 2 (2014) 5651–5659. <https://doi.org/10.1039/c4tc00738g>.
- [116] Y. He, G. Zhao, B. Peng, Y. Li, High-yield synthesis and electrochemical and photovoltaic properties of indene-C70 bisadduct, *Adv. Funct. Mater.* 20 (2010) 3383–3389. <https://doi.org/10.1002/adfm.201001122>.
- [117] G. Yang, Z. Wang, Y. Duan, D. Zhao, J. Yu, High-Performance Organic Photodetectors by Introducing a Non-Fullerene Acceptor to Broaden Long Wavelength Detective Spectrum, *Nanoscale Res. Lett.* 14 (2019). <https://doi.org/10.1186/s11671-019-3033-8>.
- [118] D. Deng, Q. Luo, Synthesis and photovoltaic properties of new medium band gap polymers based on phthalimide units, *J. Mater. Sci. Mater. Electron.* 27 (2016) 1378–1383. <https://doi.org/10.1007/s10854-015-3900-8>.
- [119] P.K. Shin, P. Kumar, A. Kumar, S. Kannappan, S. Ochiai, Effects of organic solvents for composite active layer of PCDTBT/PC 71BM on characteristics of organic solar cell devices, *Int. J. Photoenergy*. 2014 (2014). <https://doi.org/10.1155/2014/786468>.

- [120] Q. Liu, Y. Jiang, K. Jin, J. Qin, J. Xu, W. Li, J. Xiong, J. Liu, Z. Xiao, K. Sun, S. Yang, X. Zhang, L. Ding, 18% Efficiency organic solar cells, *Sci. Bull.* 65 (2020) 272–275. <https://doi.org/10.1016/j.scib.2020.01.001>.
- [121] I.-N.K. Kakaraparthi Kranthiraja, Kumarasamy Gunasekar, Woosum Cho, Young Geun Park, Jin Yong Lee, Yurim Shin, and S.-H.J. Myungkwan Song, Keun Hwa Chae, BongSoo Kim, Influential effect of π -spacers, alkyl side chains, and of the various processing conditions on the photovoltaic properties of alkylselenenyl substituted benzodithiophene based polymers, *J. Mater. Chem. C.* 3 (2015) 10715–10722. <https://doi.org/10.1039/C4TC02092H>.
- [122] F. Zhao, C. Wang, X. Zhan, Morphology Control in Organic Solar Cells, *Adv. Energy Mater.* 8 (2018) 1–34. <https://doi.org/10.1002/aenm.201703147>.
- [123] H. Zhang, Y. Li, X. Zhang, Y. Zhang, H. Zhou, Role of interface properties in organic solar cells: From substrate engineering to bulk-heterojunction interfacial morphology, *Mater. Chem. Front.* 4 (2020) 2863–2880. <https://doi.org/10.1039/d0qm00398k>.
- [124] Y. Choi, B.H. Lee, H. Kim, Bicontinuous network of electron donor-acceptor composites achieved by additive-free sequential deposition for efficient polymer solar cells, *Curr. Appl. Phys.* 20 (2020) 760–764. <https://doi.org/10.1016/j.cap.2020.03.011>.

APPENDICES

A. NMR DATA

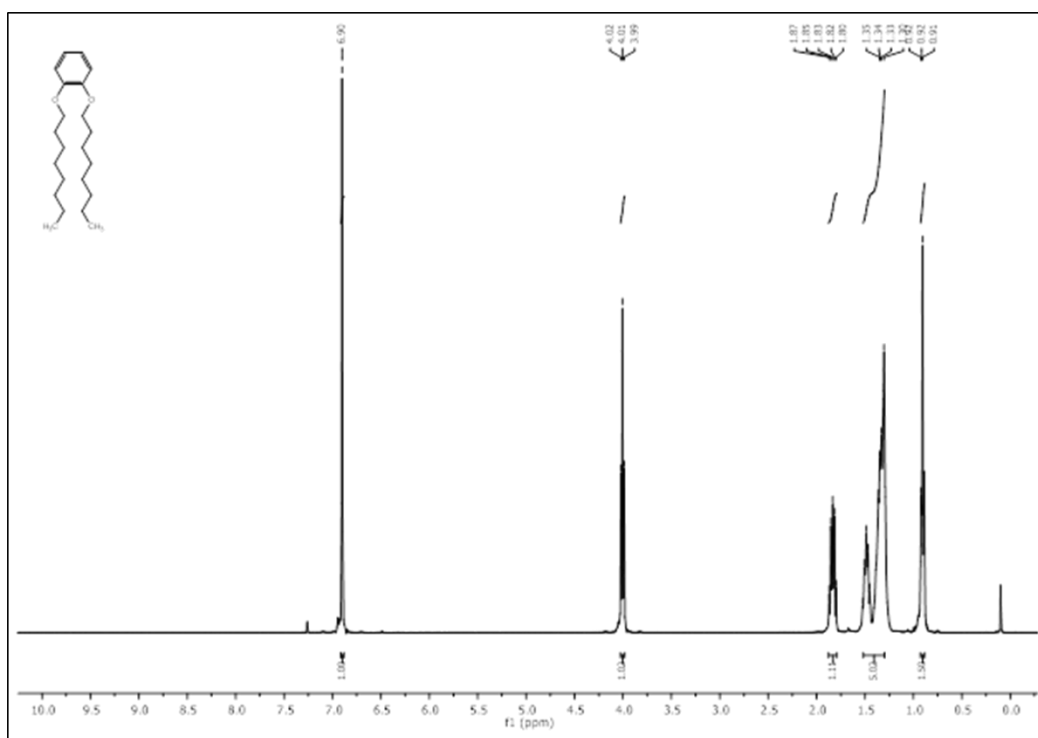


Figure A. ^1H NMR spectrum of compound 1 in CDCl_3

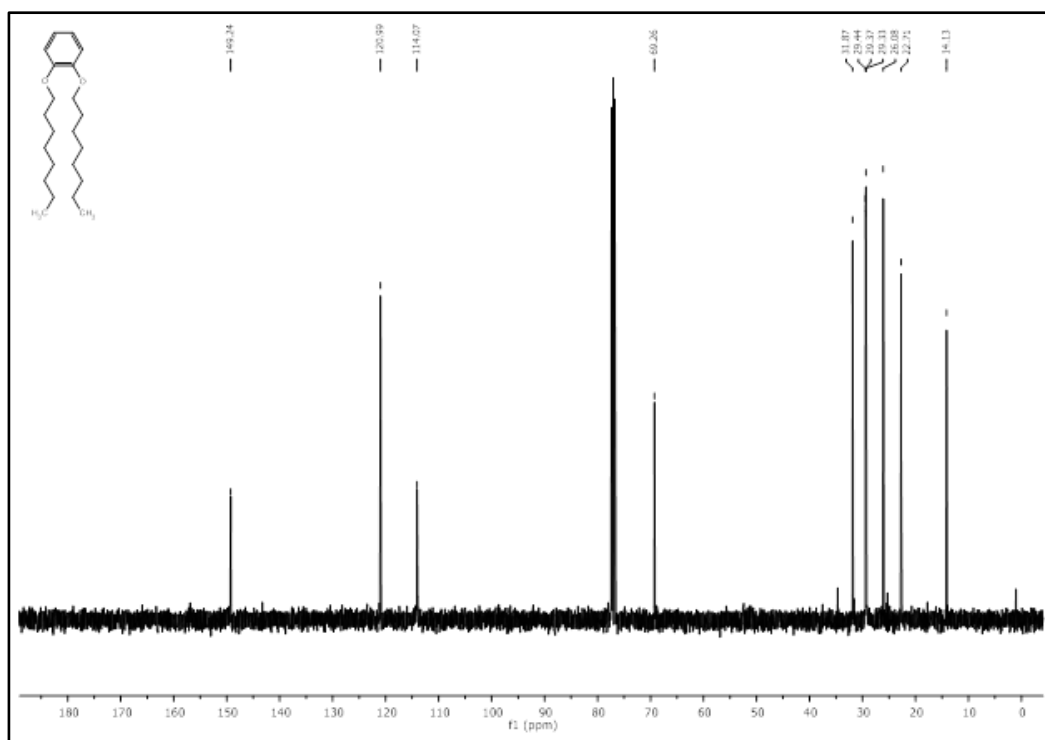


Figure A. 2 ^{13}C NMR spectrum of compound 1 in CDCl_3

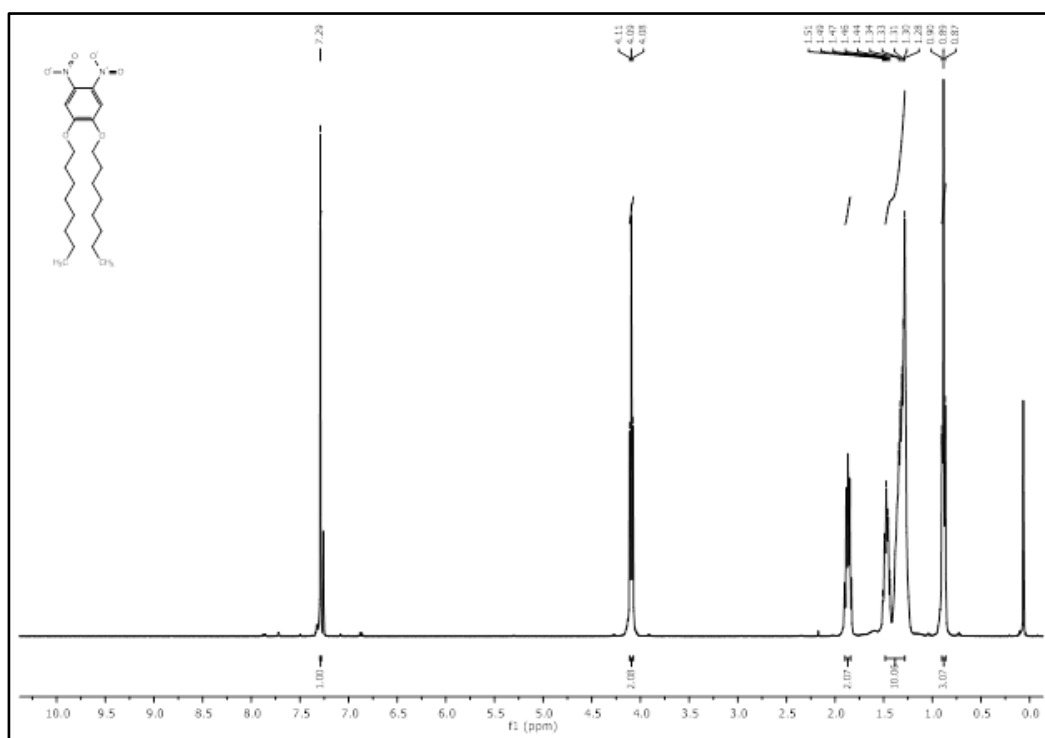


Figure A. 3 ^1H NMR spectrum of compound 2 in CDCl_3

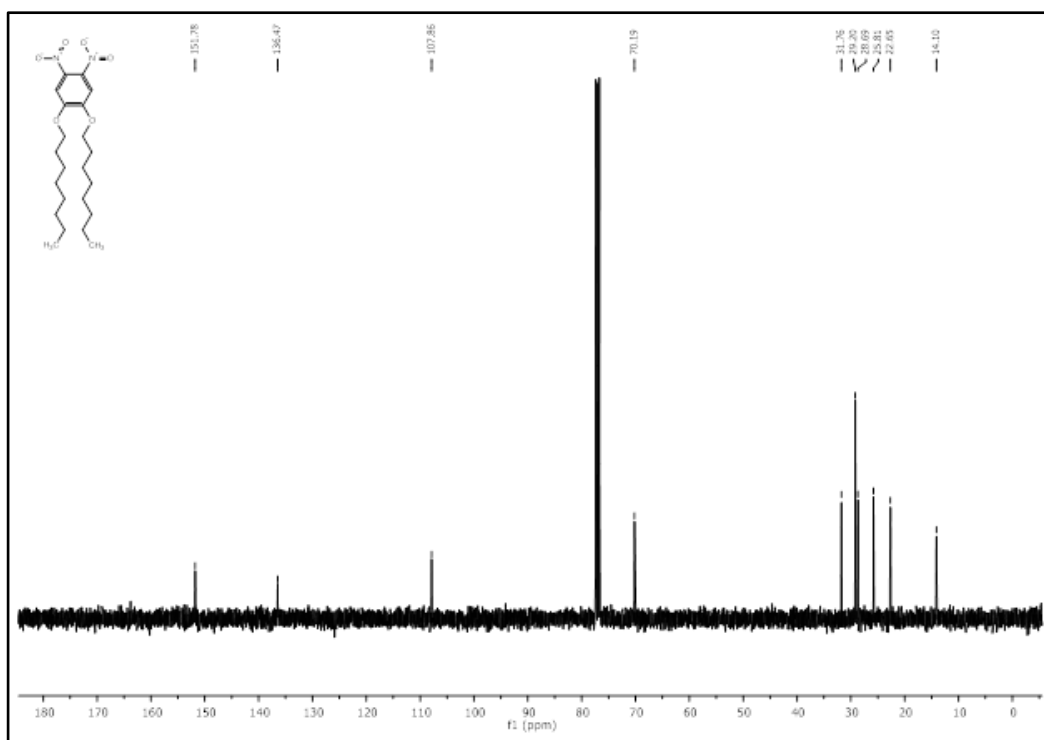


Figure A. 4 ^{13}C NMR spectrum of compound 2 in CDCl_3

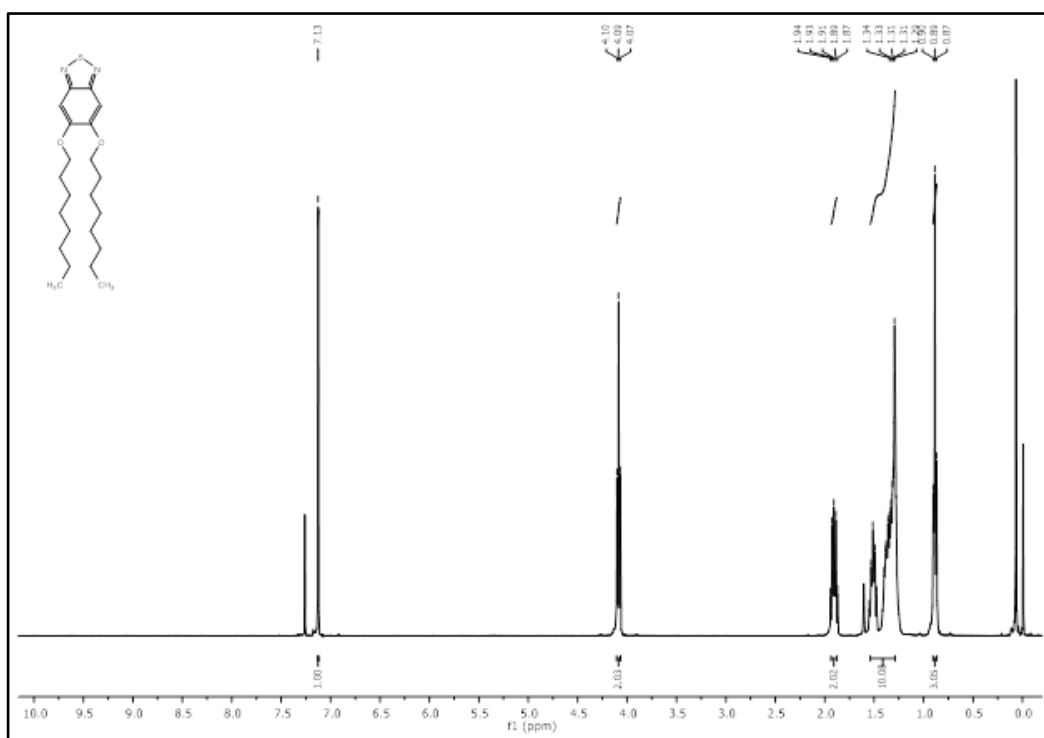


Figure A. 5 ^1H NMR spectrum of compound 3 in CDCl_3

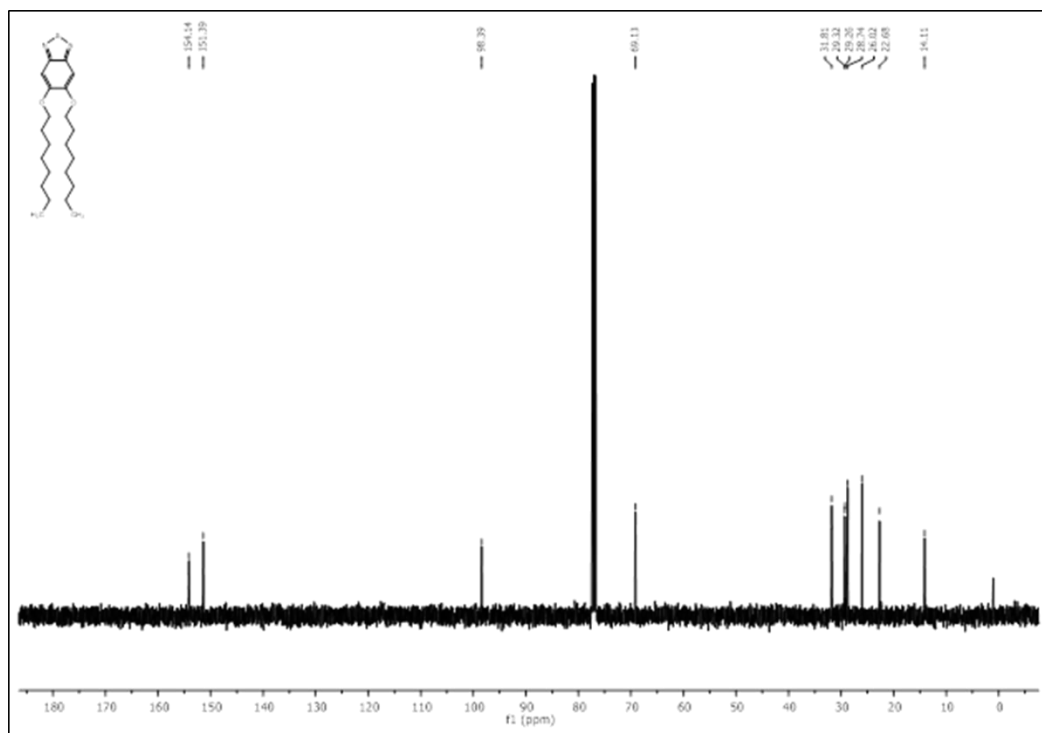


Figure A. 6 ^{13}C NMR spectrum of compound 3 in CDCl_3

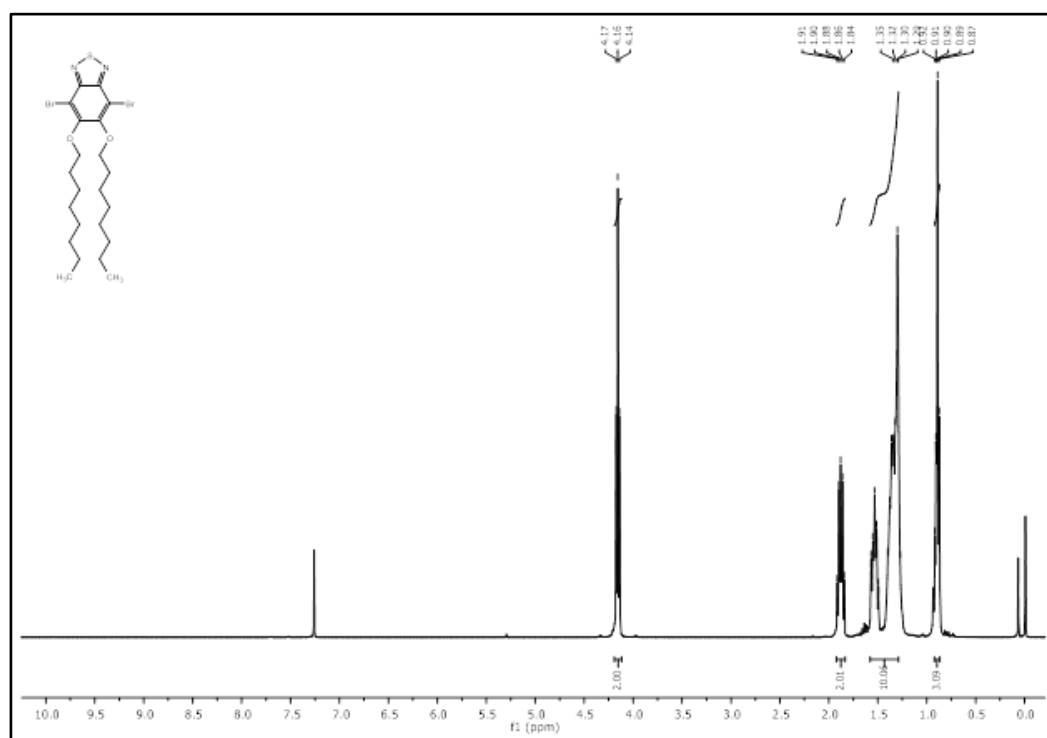


Figure A.7 ^1H NMR of compound 4 in CDCl_3

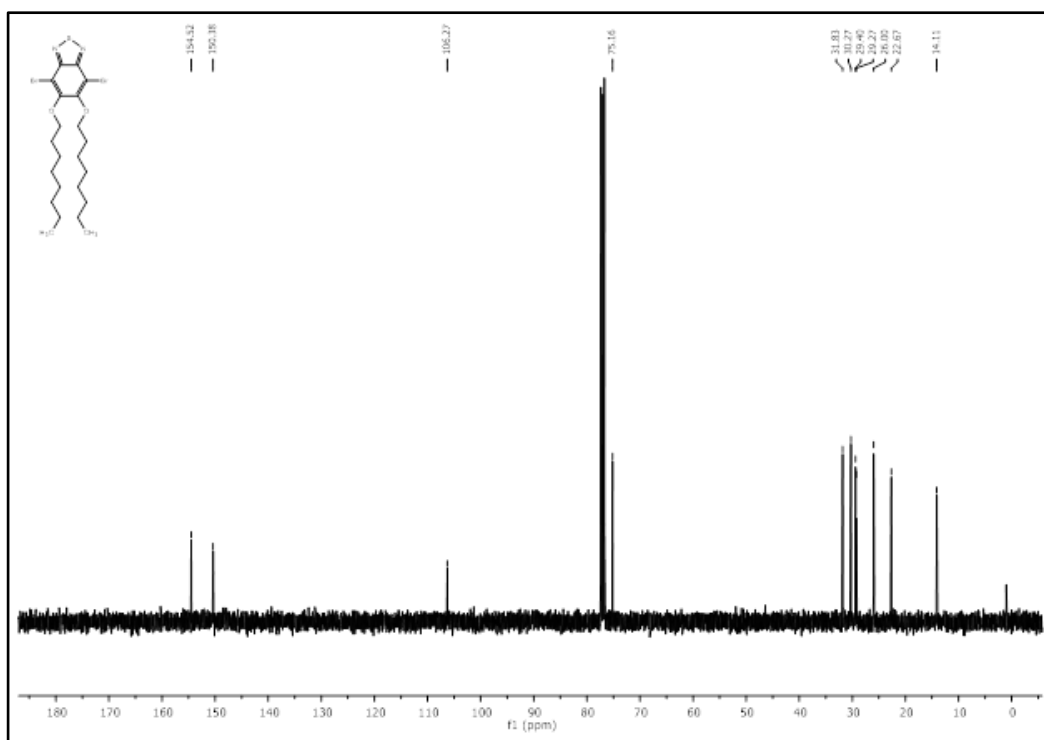


Figure A. 8 ^{13}C NMR of compound 4 in CDCl_3

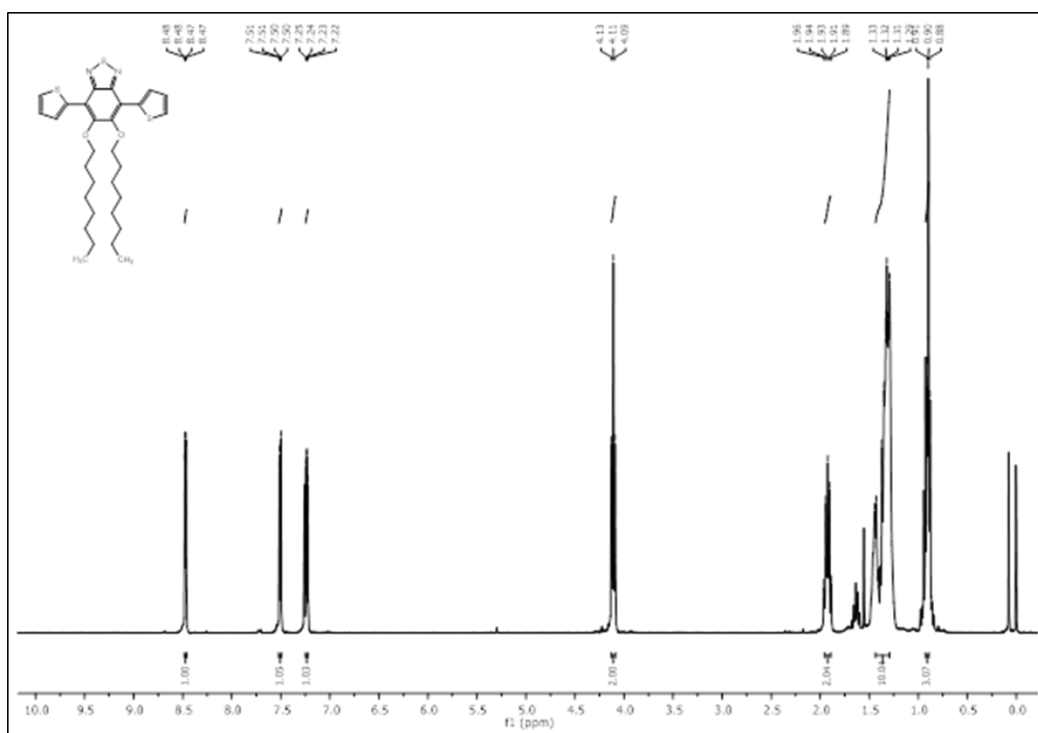


Figure A. 9 ^1H NMR spectrum of TBT in CDCl_3

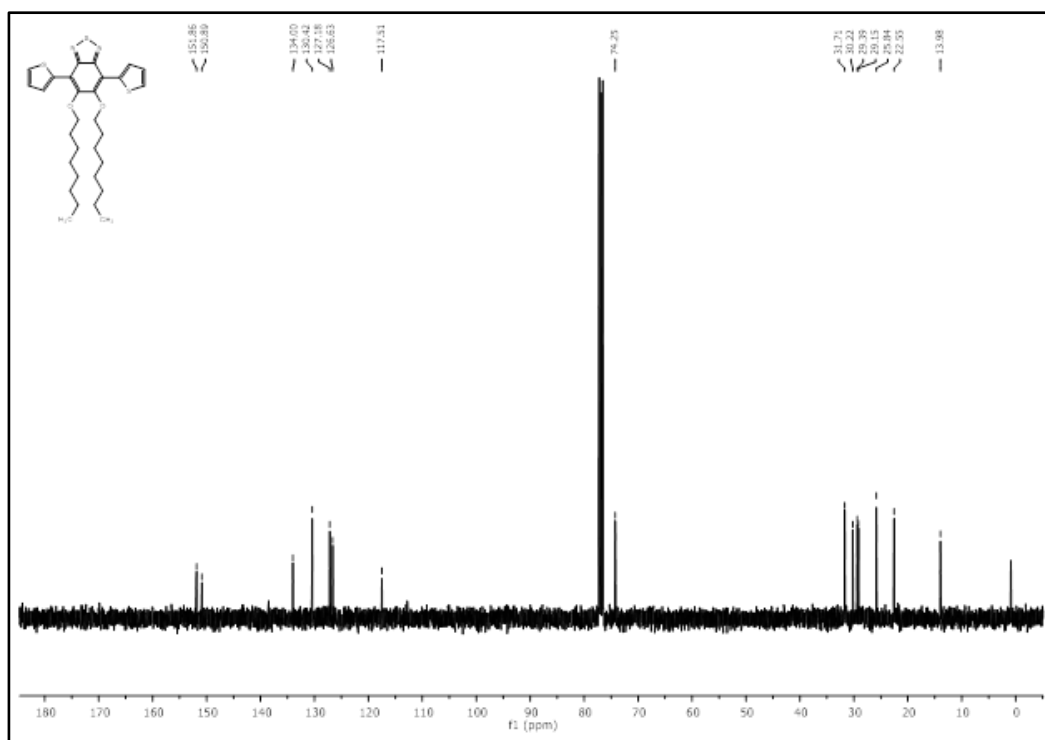


Figure A. 10 ^{13}C NMR spectrum of TBT in CDCl_3

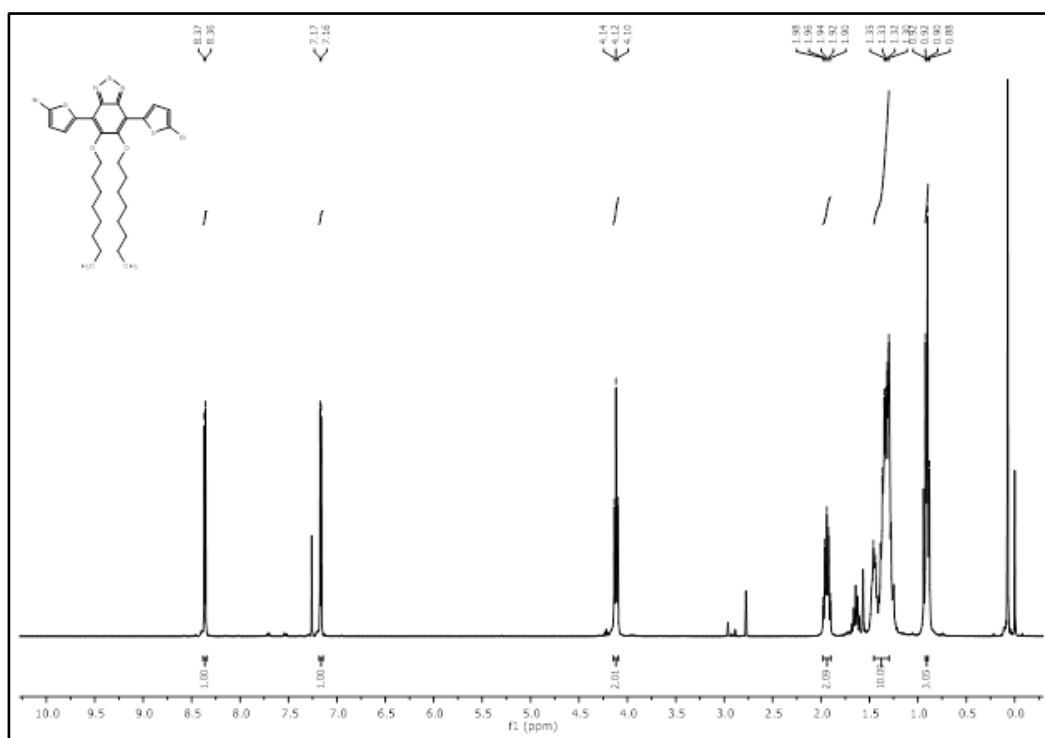


Figure A. 11 ^1H NMR spectrum of TBTBr in CDCl_3

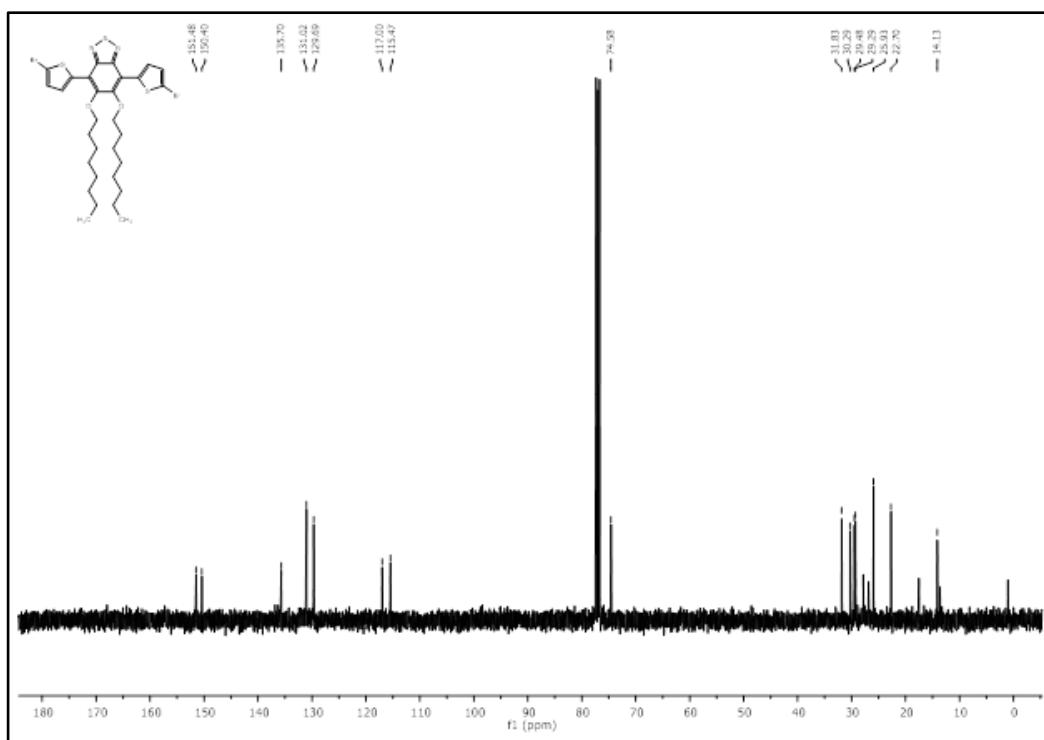


Figure A. 12 ^{13}C NMR spectrum of TBTBr in CDCl_3

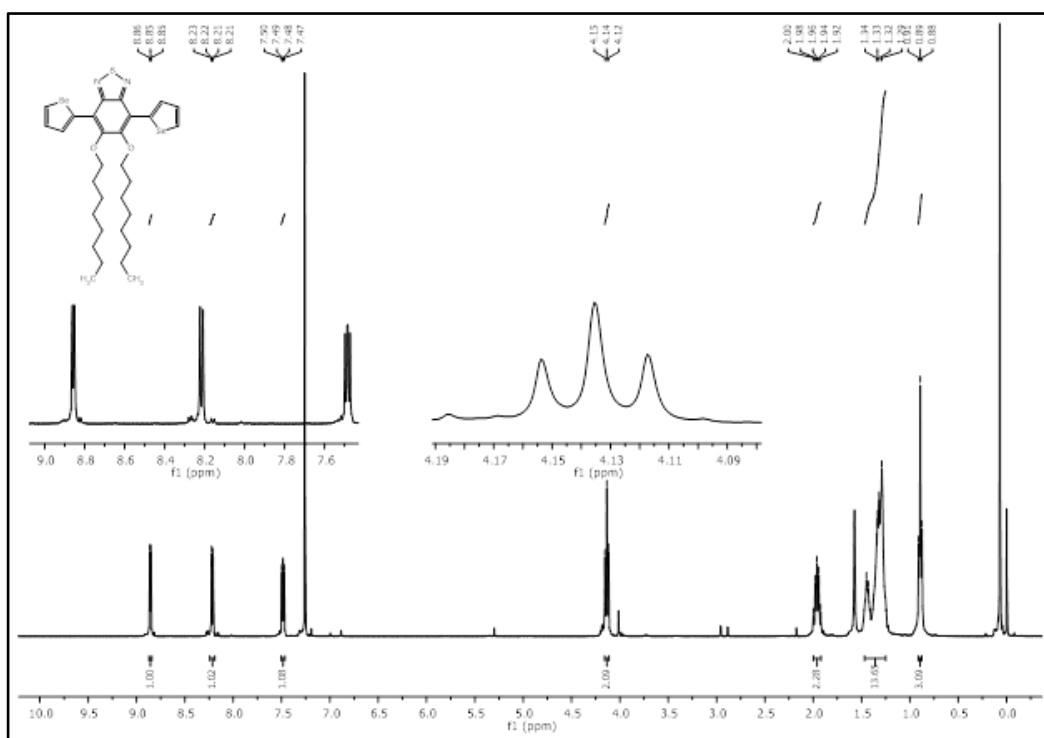


Figure A. 13 ^1H NMR spectrum of SeBT in CDCl_3

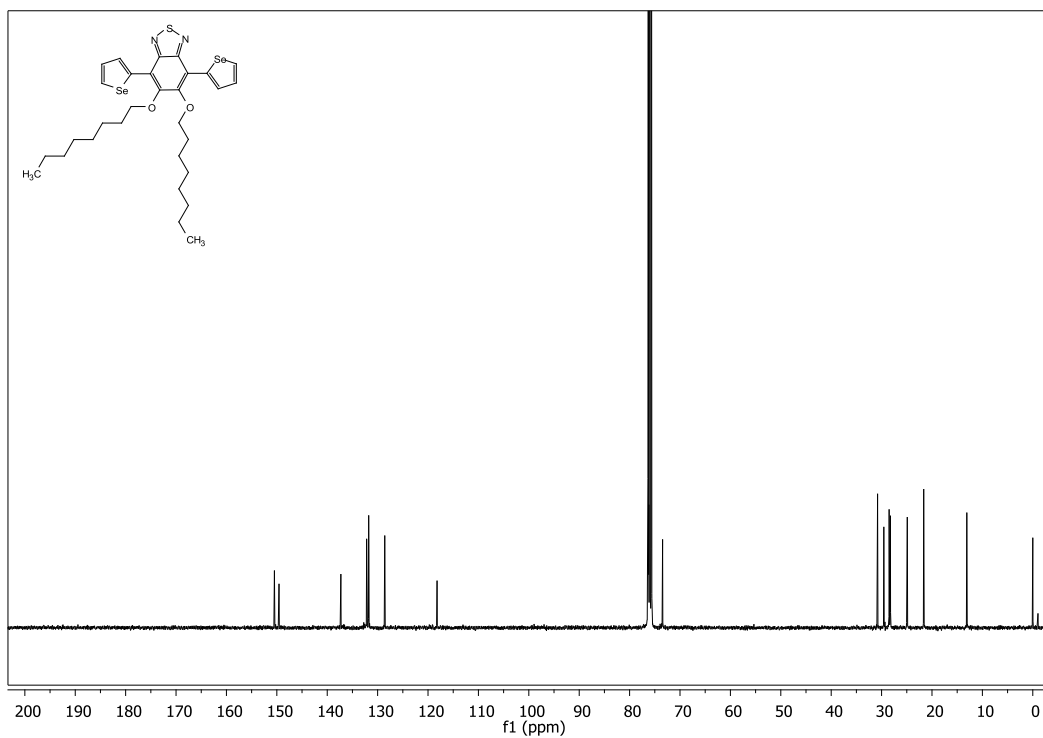


Figure A. 14 ^{13}C NMR spectrum of SeBT in CDCl_3

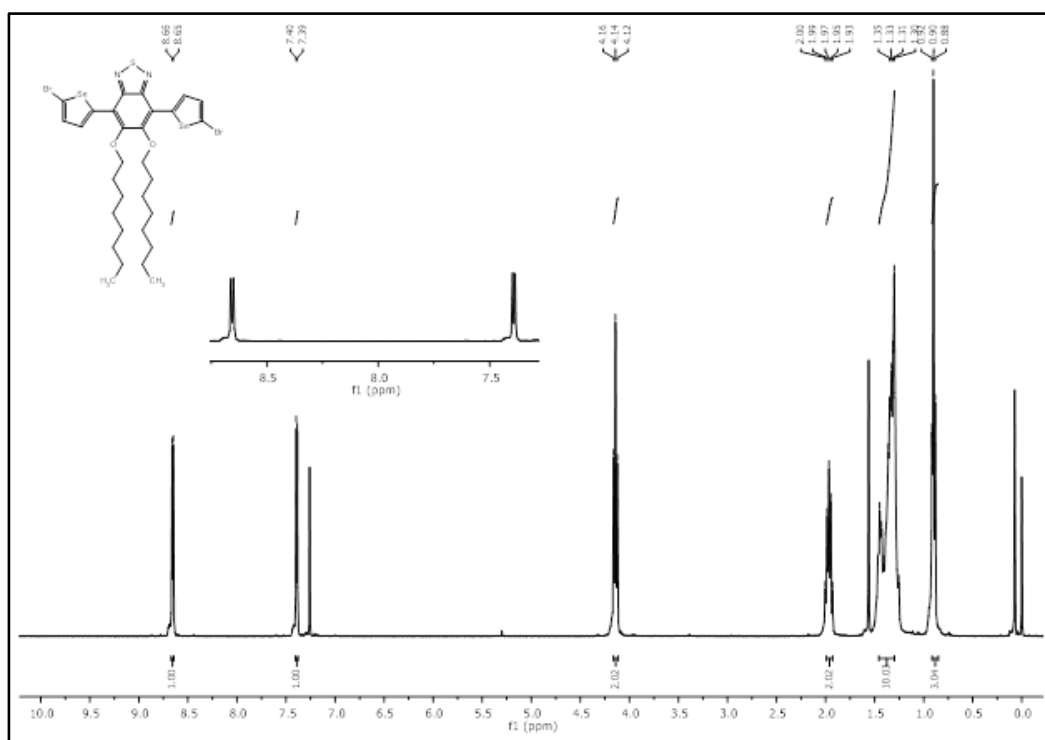


Figure A. 15 ^1H NMR spectrum of SeBTBr in CDCl_3

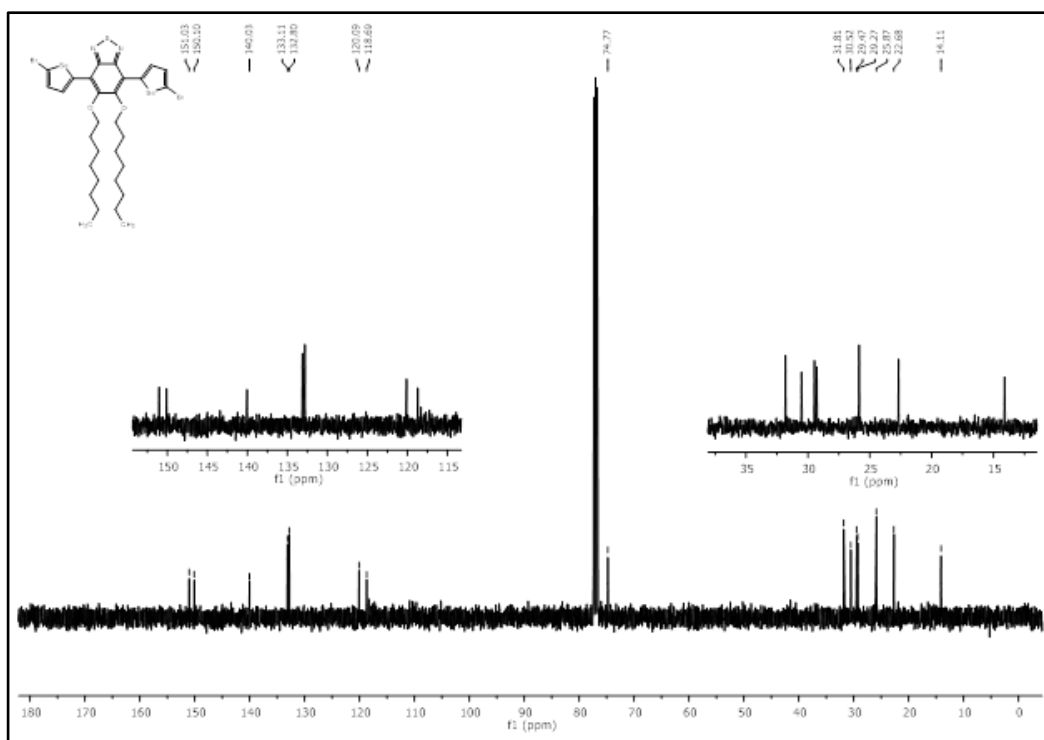


Figure A. 16 ^{13}C NMR spectrum of SeBTBr in CDCl_3

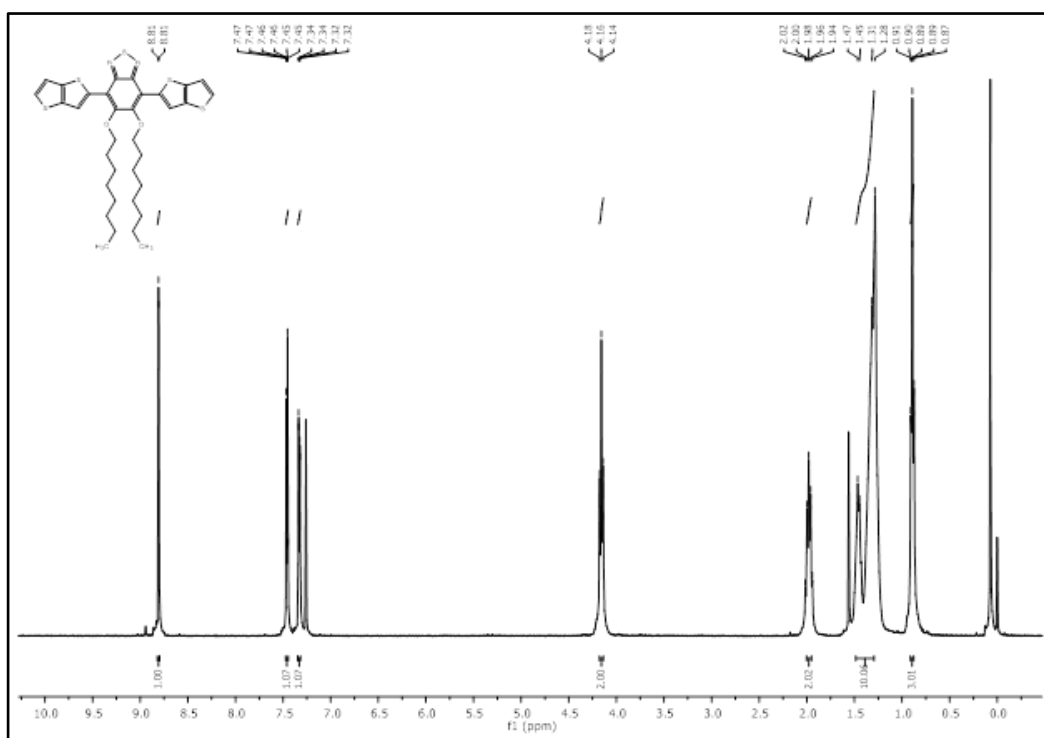


Figure A. 17 ^1H NMR spectrum of TTBT in CDCl_3

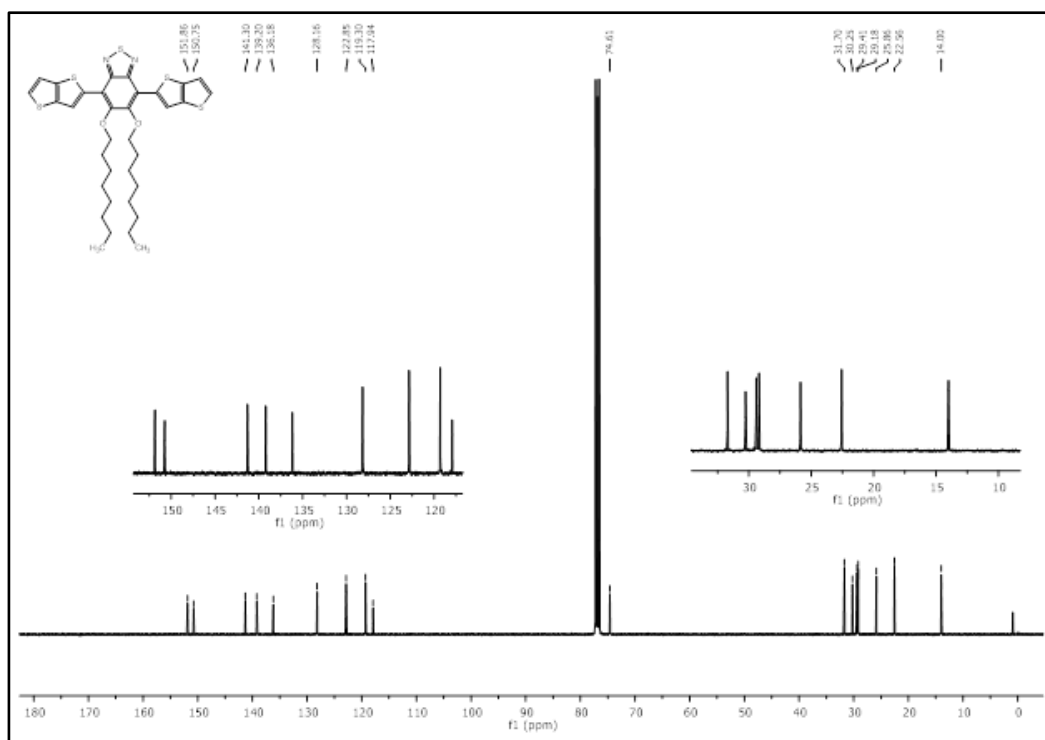


Figure A. 18 ^{13}C NMR spectrum of TTBT in CDCl_3

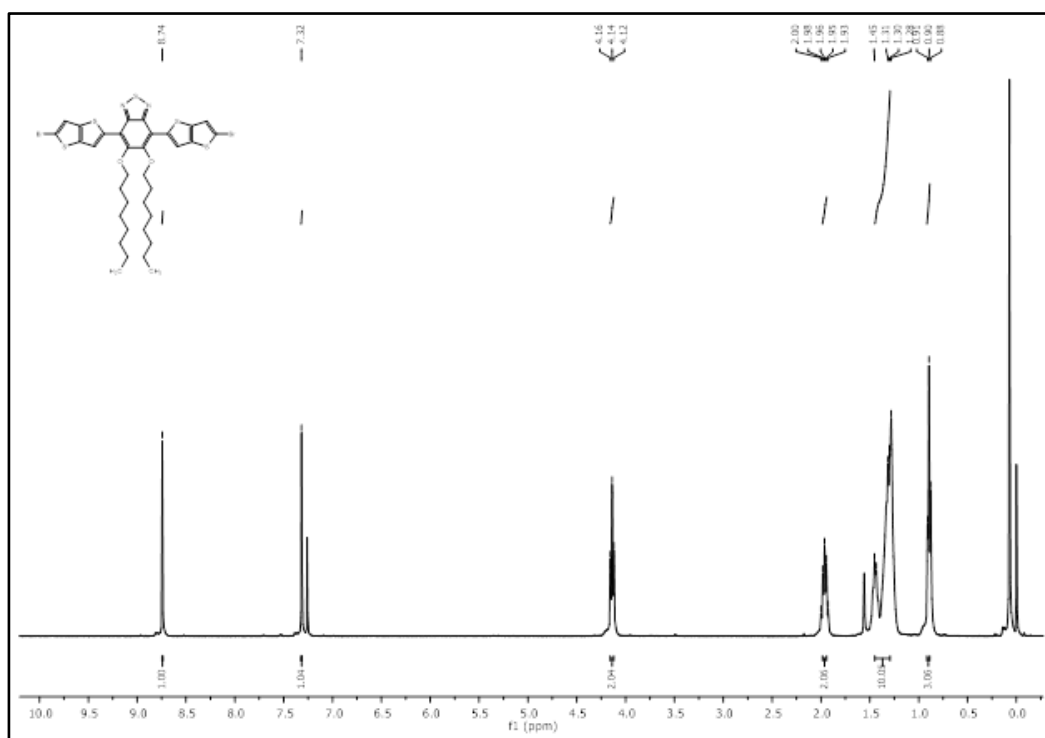


Figure A. 19 ^1H NMR spectrum of TTBTBr in CDCl_3

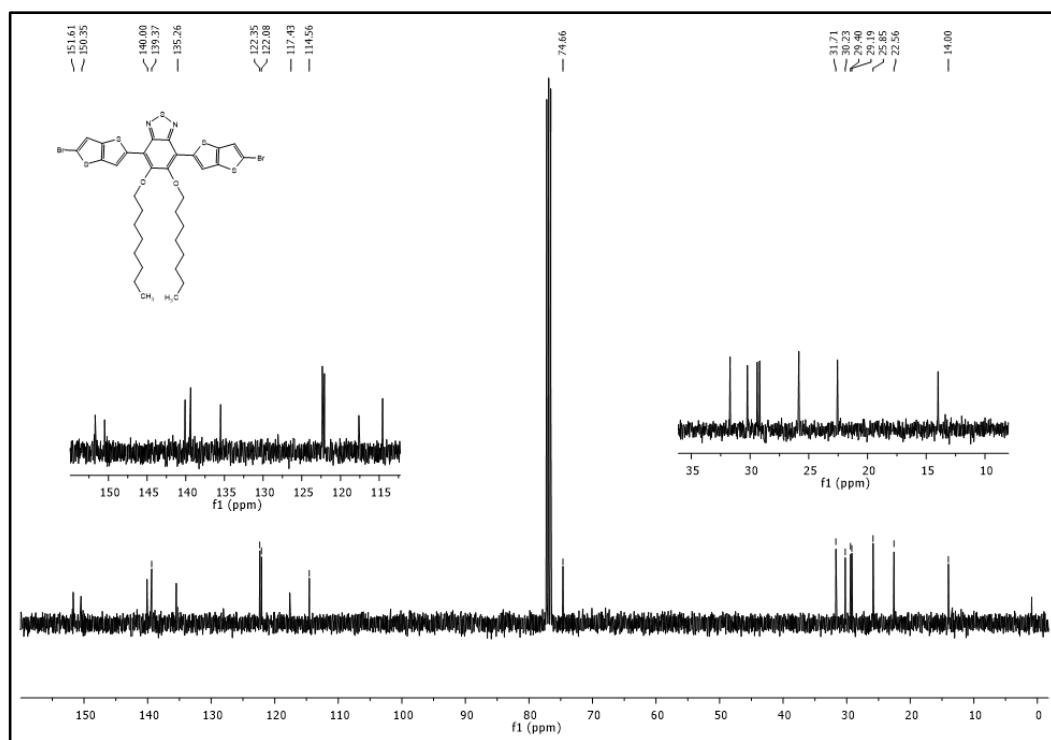


Figure A. 20 ^{13}C NMR spectrum of TTBTBr in CDCl_3

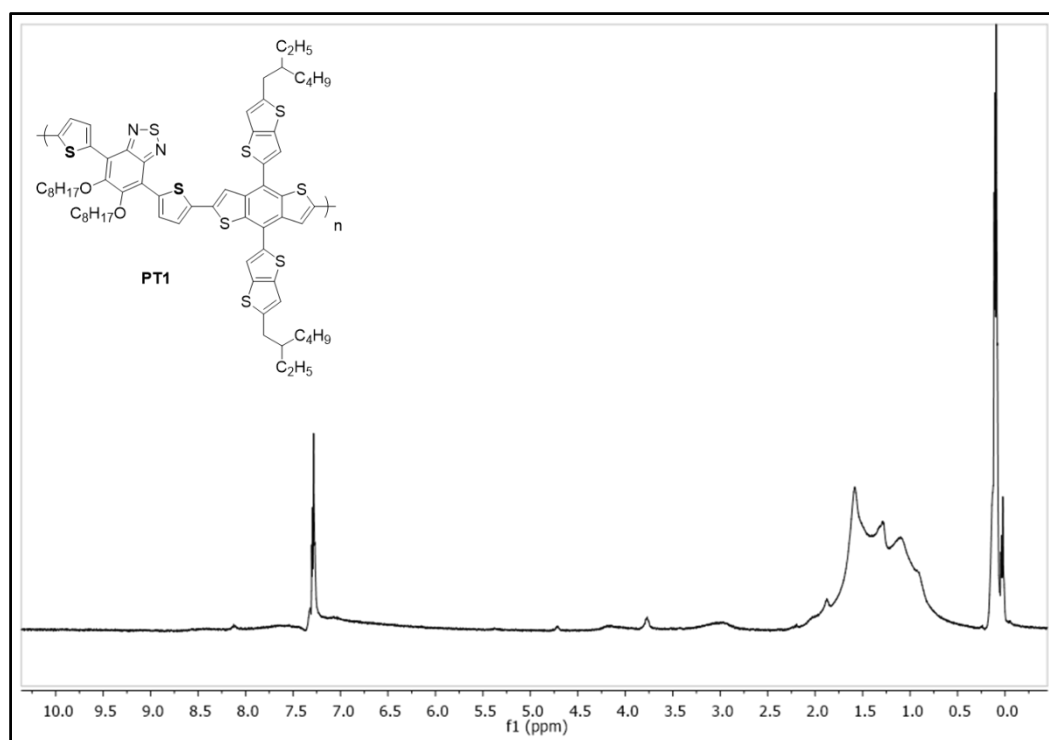


Figure A. 21 ^1H NMR spectrum of PT1 in CDCl_3

B. THERMAL ANALYSIS DATA

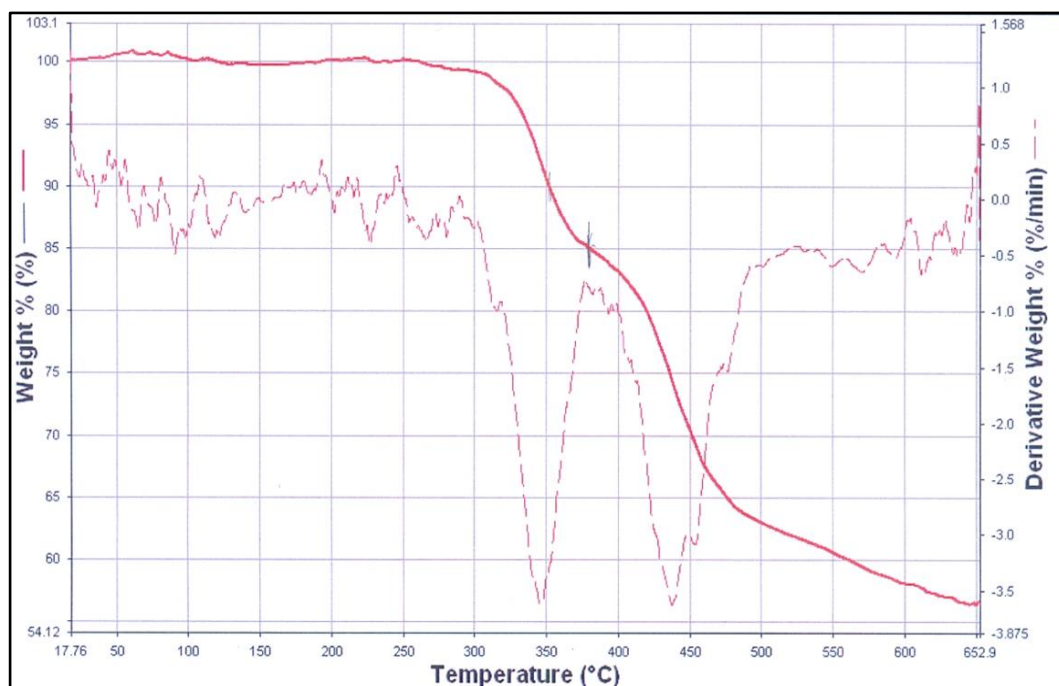


Figure B. 1 TGA study of PT1

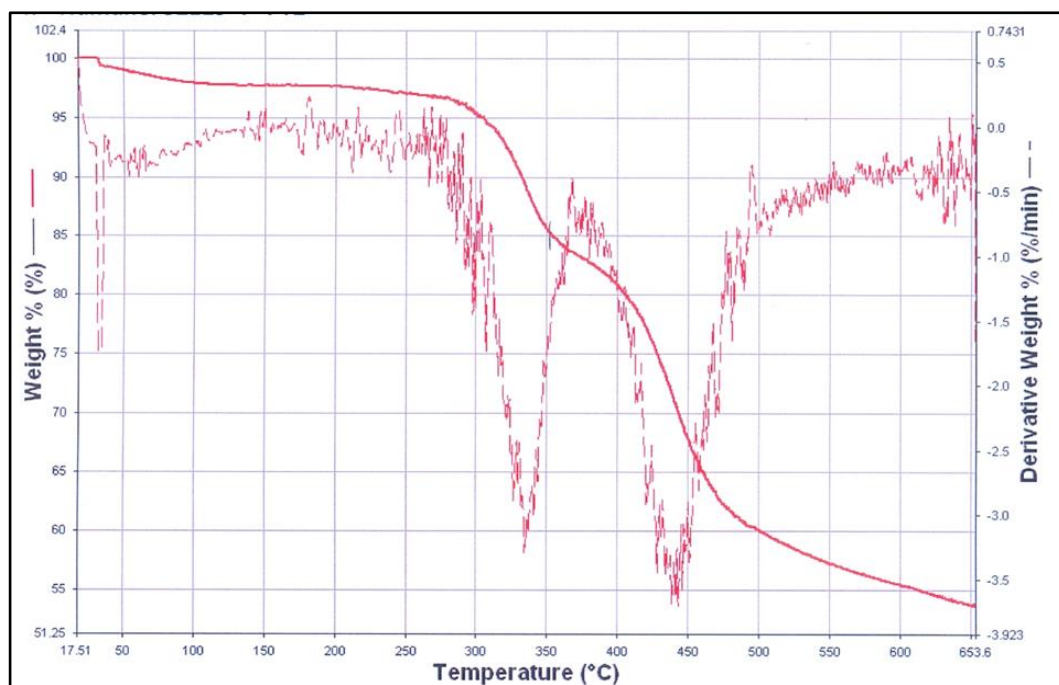


Figure B. 2 TGA study of PT2

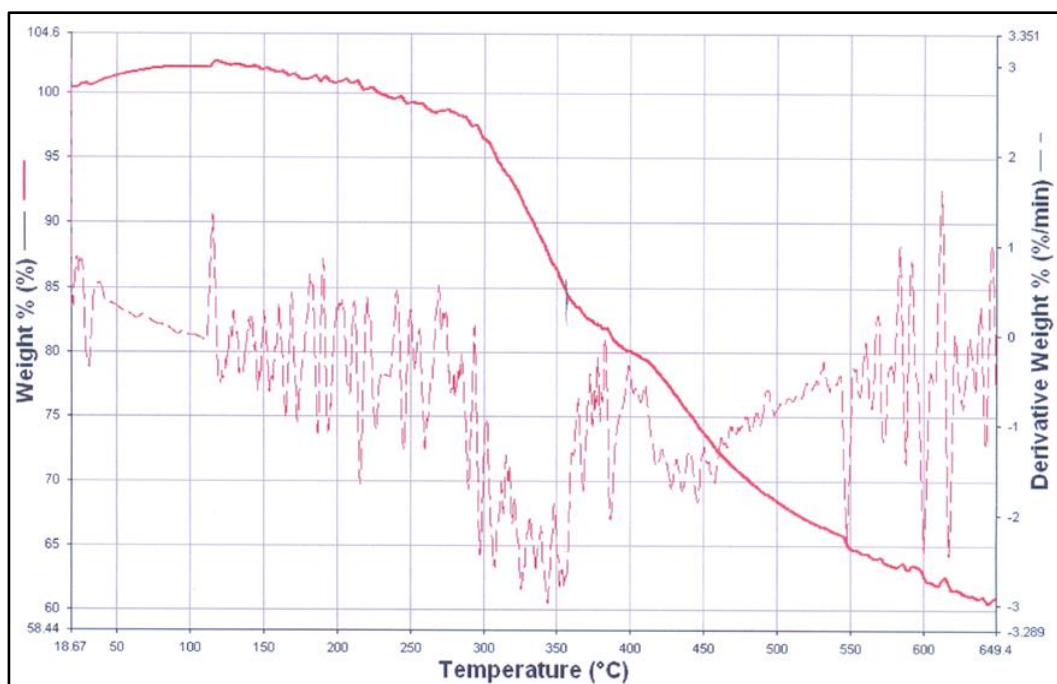


Figure B. 3 TGA study of **PT3**